FRA-OR&D-75-93

CONCRETE TUNNEL LINERS
STRUCTURAL TESTING OF SEGMENTED LINERS

AUGUST 1975

FINAL REPORT

Prepared for

Department of Transportation
FEDERAL RAILROAD ADMINISTRATION
Washington, D.C. 20590

NOTICE

Technical Report Documentation Page

1. Report No.	2. Government Accession No.	3. Recipient's Catalog No.
FRA OR&D 75-93		

4. Title and Subtitle	5. Report Date
CONCRETE TUNNEL LINERS: STRUCTURAL TESTING OF SEGMENTED LINERS	August 1975
	6. Performing Organization Code
7. Author(s)	8. Performing Organization Report No.
S. L. Paul and G. K. Sinnamon	UILU-ENG-75-2013
9. Performing Organization Name and Address	10. Work Unit No. (TRAIS)
Department of Civil Engineering University of Illinois at Urbana-Champaign Urbana, Illinois 61801	11. Contract or Grant No. DOT FR 30022
	13. Type of Report and Period Covered Aug. 1974 - Aug. 1975 Final Report
12. Sponsoring Agency Name and Address	14. Sponsoring Agency Code
Federal Railroad Administration Department of Transportation Washington, D. C. 20590	

15. Supplementary Notes

16. Abstract

Tests of three circular segmented steel-fiber-reinforced concrete tunnel liners are described. They were 10 ft outside diameter and loaded with hydraulic rams in a manner that approximates a ground loading. There were six segments and a key in each ring and the segments were ribbed to allow bolting them together. Two tests were on single rings of segments and the third was on 3 rings bolted together.

A series of beams that were designed to fail in shear and made of steel-fiber-reinforced concrete were tested. The results are used to develop a means for predicting shear strength of liner segments subjected to moment and thrust as well as shear.

Segment joints similar to those used in the liner tests were subjected to eccentrically applied thrust in a testing machine so that thrust and moment were present in varying combinations at the joint. These joints were also cast of steel-fiber-reinforced concrete, and methods are presented to calculate their strength. These methods are then compared with the test results.

17. Key Words	18. Distribution Statement
Tunnel Liners, Steel-Fiber Concrete, Segmented Concrete Liners, Liner Tests	Document is available to the public through the National Technical Information Service, Springfield, Virginia 22151

19. Security Classif. (of this report)	20. Security Classif. (of this page)	21. No. of Pages	22. Price
Unclassified	Unclassified	170	

Form DOT F 1700.7 (8-72) Reproduction of completed page authorized

PREFACE

Research described in this report was performed by the Department of Civil Engineering at the University of Illinois at Urbana-Champaign, Urbana, Illinois from August 1974 to August 1975. The project was sponsored by the Federal Railroad Administration, Department of Transportation, through contract No. DOT FR 30022. Mr. William N. Lucke was the technical representative for the Federal Railroad Administration. He helped to formulate the research goals and made many helpful suggestions during the work. His help is greatly appreciated.

Assistance was provided by Professors R. B. Peck, E. J. Cording and Mr. H. W. Parker. These men provided geotechnical input into the planning of the test programs by defining the major problems and giving advice in techniques for approaching the solution to those problems.

Much of the research was carried out by research assistants in the Department of Civil Engineering. Those who had primary responsibility in the various areas were:

Chapter 2 Shear Strength of Steel-Fiber-Reinforced Concrete Beams
R. N. Prado

Chapter 3 Tests of Bolted Reinforced Concrete Connections
I.-B. Park

Chapter 4 Tests of Large-Scale Bolted Segmented Liners
H. Nikooyeh
R. N. Prado

Student employees D. Coultas and D. Guse helped to prepare the large-scale liner test specimens.

TABLE OF CONTENTS

LIST OF TABLES

LIST OF FIGURES

LIST OF SYMBOLS

CHAPTER 2

A_g	gross area of section
A_s	area of non-prestressed tension reinforcement
a	length of region of constant shear
b_w	width of compression face of rectangular members or web of T-beams
d	distance from extreme compression fiber to centroid of tension reinforcement
f'_c	compressive strength of concrete
f_{ct}	splitting tensile strength of concrete
f_r	modulus of rupture of concrete
h	overall thickness of section
h_f	depth of flange in compression
I	second moment of the uncracked transformed area of the section
M_m	modified bending moment
M_u	applied design load moment at section
N_u	design axial load
p_f	steel fiber content, percent by volume
Q	first moment of area above the neutral axis about the neutral axis
V_{cr}	load at which flexure shear cracks form

V_u	total applied design shear force at section
v_c	nominal allowable shear stress of the concrete
ρ_w	$As/b_w d$

CHAPTER 3

A_t	area of diagonal-tension failure surface on one side of the separated chunk of concrete
b	width of beam
C	compression force
c	distance from extreme compression fiber to neutral axis
e	initial eccentricity
e_b	eccentricity in balanced condition
f'_c	compressive strength of concrete
f_{ct}	average splitting tensile strength of concrete
f_r	modulus of rupture of concrete
f_t	tension stress perpendicular to the failure surface
I	moment of inertia of a section
$k_1 k_3 f'_c$	magnitude of concrete compressive stress in equivalent rectangular stress block
M_b	moment at balanced condition
P	applied force
P_b	applied forces at balanced condition

Q	bolt force
S	deflection
Sv	vertical component of normal force on the diagonal-tension failure surface

CHAPTER 4

ΔD	change in diameter of the liner
b_w	web width
D	diameter of liner
d	distance from the extreme compression fiber to centroid of tension reinforcement
E	modulus of elasticity
f_r	modulus of rupture of concrete
I	moment of inertia of the section
M_u	design moment at a section
P	radial forces on the liner
V	shear forces
V_c	shear capacity of liner section
V_u	design shear force of liner section

CHAPTER 5

f'_c	specified compressive strength of concrete
f_r	modulus of rupture of concrete
p	passive forces

CHAPTER 1

INTRODUCTION

Reinforced concrete segmented tunnel liners have the potential for providing substantial cost savings over steel liners. This is particularly true with the recent increases in steel prices; yet they are seldom used. Thd cost advantage of concrete segmented liner, could be increased further by eliminating some or all of the tie bars and shear reinforcement in each segment. This may be possible with a better understanding of the behavior of a segmented liner under loading conditions that occur in the ground. Also, it may be possible to replace part or all of this secondary reinforcement with randomly oriented steel fibers in the concrete. The steel fibers also provide resistance to chipping and other damage during handling and erection.

Glass fiber reinforced concrete segments have been used to reline a 1.7 m diameter existing sewer in England by bolting together the segments inside the old tunnel and grouting them in place (BRE News, 1974). The segments, cast by Kinnear Moodie Concrete, Ltd., were 10 mm thick and weighed 50 kg each. The success of this project suggests the advantages of fiber reinforcement for segments. Steel fibers appear to present some advantages of strength and toughness, but have the possible disadvantage of corrosion.

Analysis and testing is underway to improve the understanding of overall behavior and failure modes of tunnel liners. Part of this program is described in this report. One objective of the tests reported herein is to improve the techniques for predicting the load capacity of

liners, particularly those constructed of steel-fiber-reinforced concrete. The failure mechanism of a liner section subjected to the combinations of thrust, shear and moment associated with ground loading is not well understood and cannot be inferred easily from conventional tests.

There are two significant problems associated with segmented concrete liners: damage during transportation, erection, and waterproofing. Waterproofing of segmented concrete liners is such a great problem that this type of liner has been used very little in the United States in ground with significant water present. Sound concrete can be waterproofed adequately as shown by its use in sewage treatment tanks and other structures of this nature. The primary problem occurs in waterproofing of joints that will deform during the life of the liner. Through an improved understanding of joint behavior and of the interaction between joints and segments in the liner, it may be possible to design liners with joints such that the overall deformations can occur without significant joint deformations. The waterproofing of joints would then be much easier and will hopefully make possible the design of an inexpensive and easily installed waterproofing system. The segment itself may be more difficult to design as it will be required to deform without excessive cracking. To this end structural tests of complete liners and of joints are described.

A series of beams that were cast with steel-fiber-reinforced concrete and designed to fail in shear was tested, and the results are described in Chapter 2. These tests are used to develop a means for predicting shear strength of beams. The long range purpose of the effort is to obtain information which will be useful in predicting the shear capacity of

segmented liners constructed of steel-fiber-concrete. An equation of the form used in Building Code Requirements for Reinforced Concrete (ACI 318-71) is obtained from the test data in Chapter 2, and is later used to predict the capacity of liners that were also tested.

Chapter 3 describes the structural testing of segment joints similar to those that were used in large scale liner tests. The specimens were subjected to eccentrically applied load, so thrust and moment in various combinations were present at the joint. They were cast with steel-fiber-reinforced concrete, and during the test the joint opening and overall deformation were measured. Tentative methods for predicting the strength of joints of the type tested are presented.

Tests of three circular, segmented, steel-fiber-reinforced-concrete liners are described in Chapter 4. They were 10 ft (3.05 m) outside diameter and loaded with hydraulic rams in a manner that approximates a ground loading and includes a passive loading mechanism to represent the passive forces near the springlines. There were 6 segments and a key in each ring and the segments were ribbed to allow bolting them together. Two tests were on single rings of segments, and the third test was on 3 rings bolted together. These tests, together with the results described in Chapters 2 and 3, may be used to formulate procedures for determining the interaction between joints and segments in a ring and the interaction between rings. This information will allow the prediction of liner deformability for use in predicting its behavior in the ground. In addition, methods can be formulated for predicting liner capacity and modes of failure which will allow liners to be designed for varying ground conditions and improvement of designs.

The research described in this report concerning the behavior of segmented liners is the first phase of a continuing program in this area. Additional tests will be performed, and analytical procedures will be developed to aid in the prediction of interaction of the liner with the ground and the structural response of the liner.

CHAPTER 2

SHEAR STRENGTH OF STEEL-FIBER-REINFORCED CONCRETE BEAMS

2.1 INTRODUCTION

A series of seven singly reinforced beams made of steel-fiber-reinforced concrete that were designed to fail in a mode designated classically as "shear" were tested. There was no shear reinforcement in the beams. The purpose of the study was to determine a procedure for predicting the shear capacity of segmented concrete liners made with steel-fiber-reinforced concrete. Liners of this type were tested and are reported in Chapter 4.

The ACI Code formula for shear capacity prediction for conventional beams was altered to provide satisfactory prediction of steel-fiber-reinforced beam capacity. This formula was then modified to account for axial load and shape of section so that it could be applied to the segmented liners. The modification used for thrust was taken from the Building Code Requirements for Reinforced Concrete (ACI 318-71; 1971), and that for shape of section from the ACI-ASCE Task Committee 426 Report (1973). The modifications for conventional concrete were applied directly to steel-fiber-reinforced concrete because they are related primarily to the compressive strength of the concrete, which changes very little with addition of steel fibers.

Two variables were considered: amount of steel fibers in the concrete, p_f, and shear span, a, the latter being an indication of the moment-shear ratio. Table 2.1 summarizes the material properties of the beam specimens, steel fiber content and the geometric variables. The steel

fibers used were U.S. Steel Fibercon with dimensions 10 mils x 22 mils (0.25 mm x 0.56 mm) cross section by 1 in. (25 mm) length, with a volume content ranging from 0.24 to 1.51 percent. These fibers are sheared from sheet steel with a thickness of 10 mils (0.25 mm). The surface of the fiber resulting from the shearing operation may influence the concrete-steel bond characteristics.

Behavior of beams that suffer distress due to shear forces will be reviewed briefly. As loading of a member subjected to flexure and shear progresses, vertical flexure cracks normally appear first, and result from tension stresses in the direction of the longitudinal axis of the beam. This stress is maximum at the bottom of the member. In the region of the member subjected to shear force, there are shear stresses on a vertical section through the member which are maximum at or above the midheight of the member and zero at the top and bottom faces. The horizontal shear stress is equal to that on a vertical section so these two shear stresses result in a tension stress on a 45-degree plane. This tension stress also increases toward the midheight of the member from zero at the top and bottom faces. The flexure crack due to tension progresses vertically as load is increased; tension above this crack on an inclined plane due to the shear stress increases also causing the principal tension stress from the flexure and shear combined to be inclined, and, thus, the tension crack to become inclined. When this occurs, the first inclined cracking is said to occur. The first inclined cracking load is significant because it is an indication that the shear stresses are large enough to cause the combined tension stress to exceed the tensile strength of the concrete. The load

at which this occurs is not just a function of the shear, but depends on the relative amounts of flexure and shear. For example, if there is less flexure, the flexure cracks will not progress as high in the beam, so a greater shear force must be applied to reach the critical shear stress that will cause inclined cracking.

Inclined cracking may or may not cause collapse of the member. There are two mechanisms (at least) to resist the shear forces, and the tension stress across a potential inclined crack is one of them. Once the inclined crack develops, the shear force may be resisted by a shear force in the compression region of concrete above the neutral axis. If the shear capacity of the latter mechanism is larger than that which developed the inclined crack, the mechanism of resistance will be changed and more load can be added until the concrete in the compression region fails due to the combined forces, and a "shear-compression" failure is said to occur. If the shear capacity of the latter mechanism is smaller, collapse will occur immediately, and a diagonal tension failure is said to occur. This brief discussion is illustrated more completely in Fig. 2.1.

The type of failure that occurs is closely associated with the relative amounts of moment and shear in beams and for simple beams this can be related to the length of the shear span divided by the effective depth of the member (a/d). The important point is that this ratio is also a measure of the relative amounts of flexure and shear stresses in the member.

Figure 2.2 shows the range of a/d ratios associated with various types of failure as described by the Joint ASCE-ACI Task Committee 426 on Shear and Diagonal Tension (1973) for conventional concrete beams; the

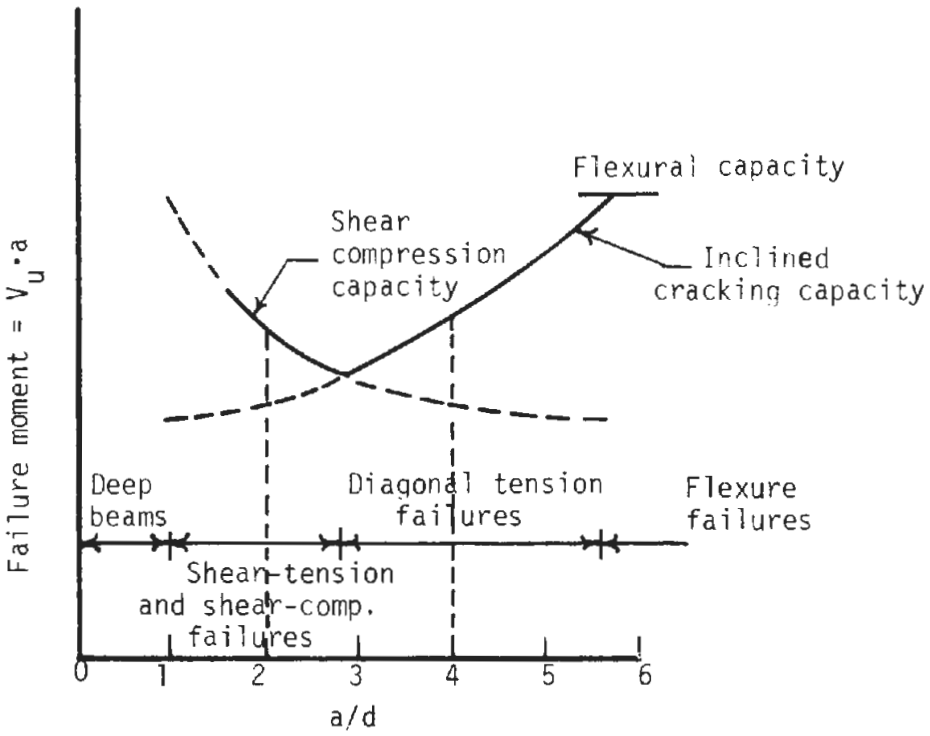

FIGURE 2.1 MODES OF FAILURE FOR NONFIBER BEAMS
(Bresler and McGregor, 1967)

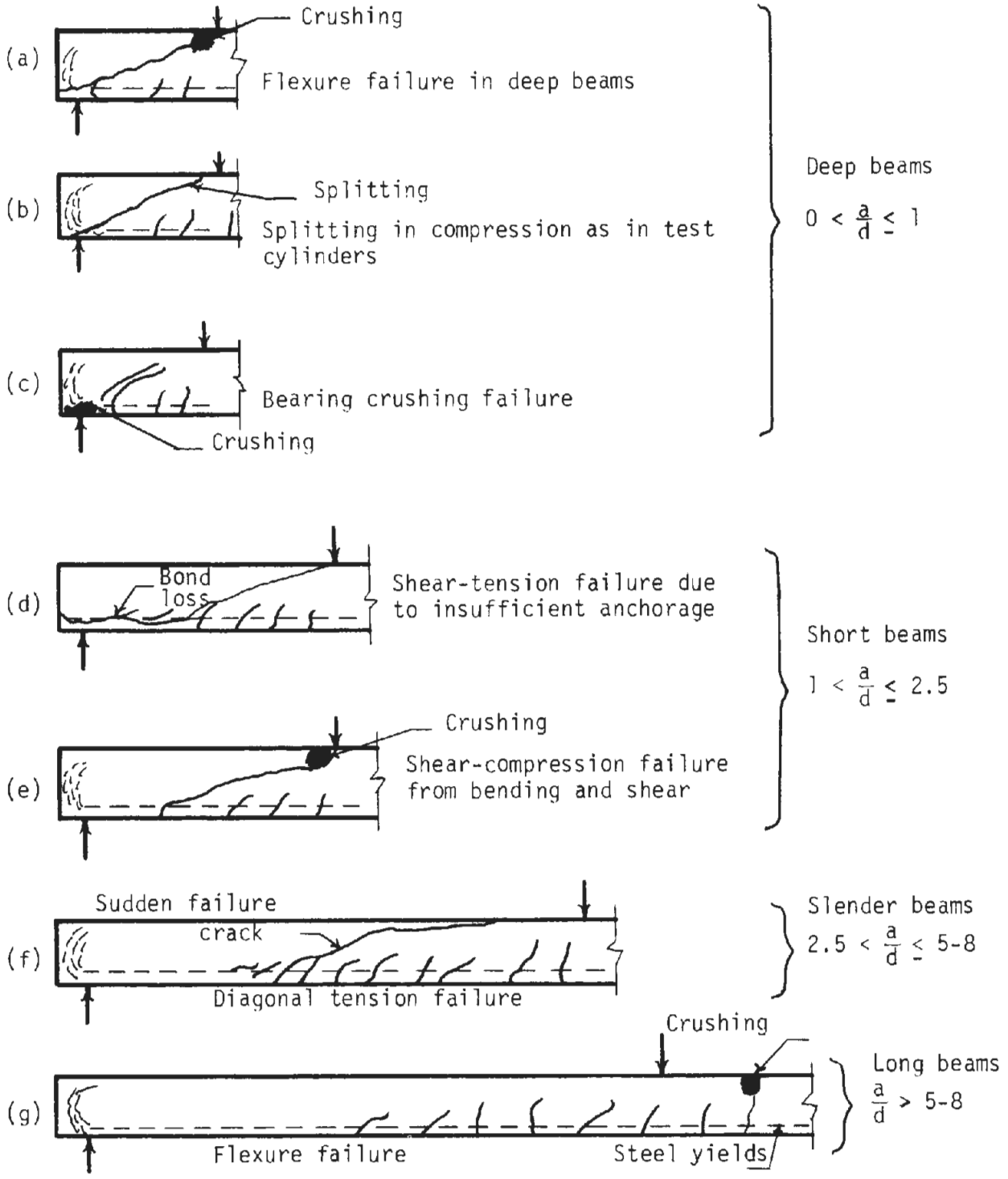

FIGURE 2.2 TYPICAL MODES OF FAILURE FOR CONVENTIONAL CONCRETE BEAMS WITHOUT SHEAR REINFORCEMENT

approximate range of a/d for flexural failures was taken from a series of tests reported by Kani (1964). The range $0 < a/d \leq 1$ applies to deep beams in which a significant amount of the load is resisted by an arch that forms in the shear span between the load point and reaction.

In the range $1 < a/d \leq 2.5$ failures shown in Fig. 2.2d and 2.2e may occur, and are called shear-tension and shear-compression failures. The former type results from insufficient anchorage of the tension reinforcement and can be avoided with proper detailing. One beam in the present study failed in this way, but is not included in the data used to develop the formulas for predicting shear strength. Shear-compression failures are the type described earlier that result when the resisting mechanism changes after a diagonal crack has formed, and finally the compression region fails from compression and shear after the application of additional load. Though the final collapse is sudden, the diagonal crack formed at a smaller load so distress is indicated before failure occurs.

In the range $2.5 < a/d \leq (5\text{-}8)$ diagonal tension failures occur in which the member collapses upon formation of the critical diagonal crack because the shear-compression mechanism has less capacity than that of the diagonal tension in the member. This failure is very sudden, and has no prior indication. The diagonal crack must have a particular location to cause failure. Some inclined cracks may appear at the end of flexure cracks and not propagate through the beam and result in failure, either because they are too near the end of the specimen where the flexure is low, or they are too close to the load so the crack would propagate into the zone under the loading block where large localized compressive stresses exist.

Long beams fail in flexure and are not significantly influenced by the shear forces though some inclined cracking may occur due to shear stresses (Fig. 2.2g).

The behavior of beams fabricated using steel-fiber-reinforced concrete will differ in some details from that described for conventional concrete beams, but the overall modes of failure will be very similar. Therefore, the available information on conventional beams provided a valuable guide in the investigation.

2.2 DESCRIPTION OF TEST

The specimens were singly-reinforced, steel-fiber concrete beams measuring 6 x 12 in. (150 mm x 300 mm) in cross section with lengths of 51 to 120 in. (1.3 m to 3 m). They were tested as simply-supported beams by applying two concentrated loads at the top of the member; the beam span and spacing of the loads are described in Table 2.1 and the nomenclature is defined in Fig. 2.3.

The load was applied by a hydraulic ram operated by an electric pump. Three load cells were used: one at the ram and one between a distributing beam and the test specimen at each of the two load points, as shown in Figs. 2.3 and 2.4. A steel ball was used under the top load cell and steel rollers at the two load points on the beam.

In order to produce failure on one side of the beam so that only one side need be instrumented, an external clamp was used on one shear span (region of constant shear). The clamp consisted of a steel plate 9 in. x 5 in. x 3/4 in. (229 mm x 127 mm x 19 mm) on the top and bottom of the beam

TABLE 2.1

DESCRIPTION OF TEST SPECIMENS

Specimen	p_f, percent by vol.	f'_c psi (MPa)	f_r psi (MPa)	f_{ct} psi (MPa)	a, in. (mm)	L, in. (mm)	d, in. (mm)	a/d,	$\rho_w = \frac{A_s}{b_w d}$
1	0.90	4410 (30.40)	555 (3.85)	525 (3.60)	22 (560)	66 (1675)	9.6 (245)	2.3	0.0208
2	0.24	5140 (35.45)	670 (4.60)	425 (2.95)	22 (560)	66 (1675)	9.6 (245)	2.3	0.0208
3	0.91	5170 (35.65)	710 (4.90)	610 (4.20)	17 (430)	51 (1295)	10.1 (255)	1.7	0.0198
4	0.93	5810 (40.05	780 (5.40)	630 (4.35)	44 (1120)	120 (3050)	10.1 (255)	4.4	0.0198
5	0.25	6560 (45.25)	650 (4.50)	560 (3.85)	44 (1120)	120 (3050)	10.1 (255)	4.4	0.0198
T1	1.51	7950 (54.80)	1320 (9.10)	not taken	44 (1120)	120 (3050)	10.1 (255)	4.4	0.0198
T2	1.51	7960 (54.90)	1370 (9.45)	not taken	22 (560)	66 (1675)	10.1 (255)	2.2	0.0198

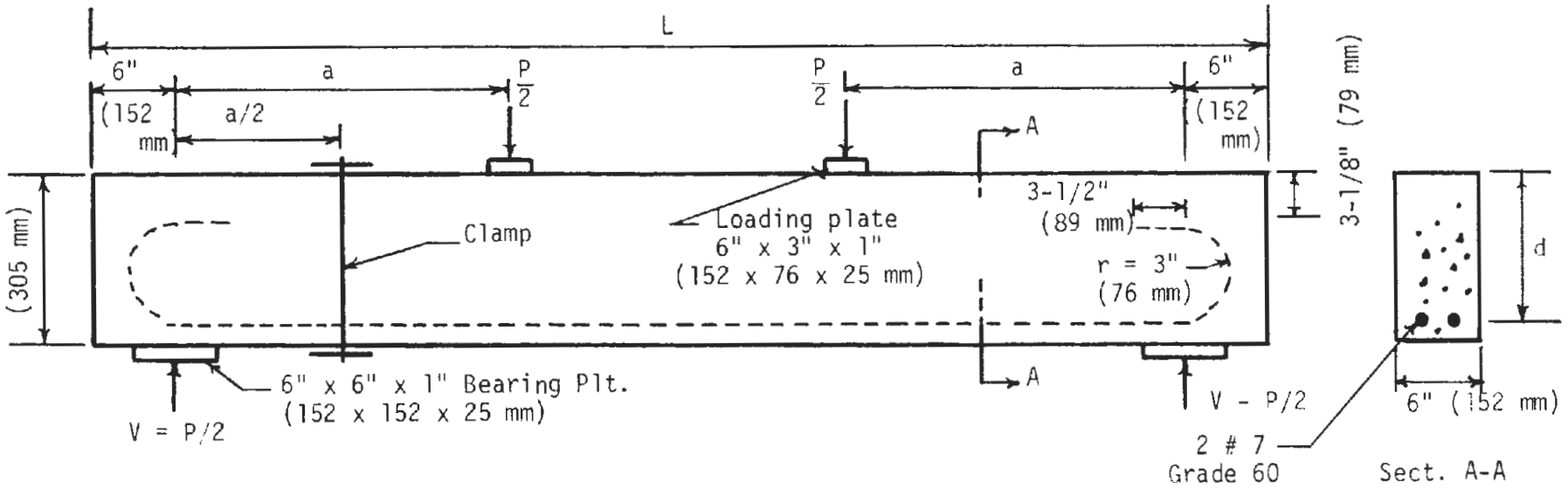

FIGURE 2.3 LOAD ARRANGEMENT FOR THE BEAM TESTS

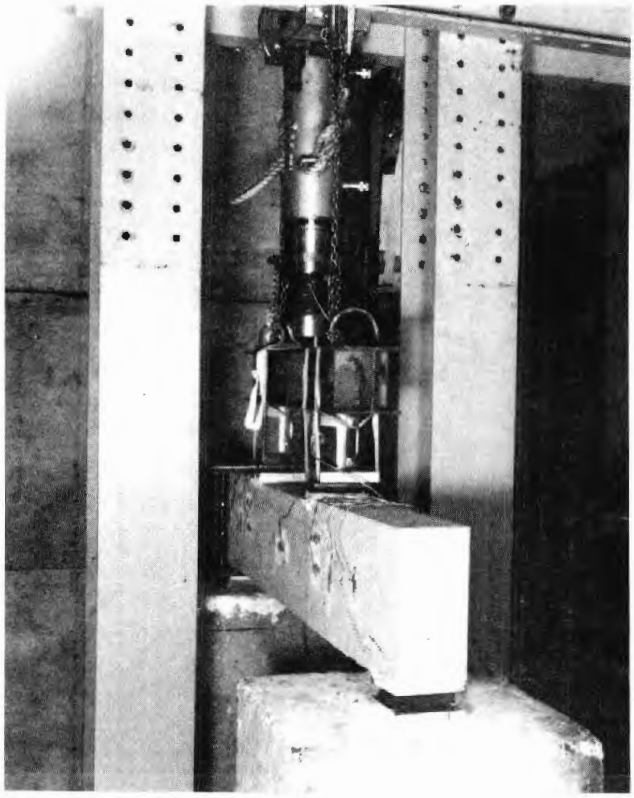

FIGURE 2.4 PHOTOGRAPH OF THE BEAM TEST ARRANGEMENT

pulled together by two steel rods 7/8 in. (22 mm) diameter. This clamp is shown in Figs. 2.3 and 2.5. Load was applied at a rate of approximately 1000 lb/min (4.5 kN/min) at each of the two load points.

The test data consisted of the following: ram load, two concentrated loads on the beam specimen, deflections at both midspan and the load points, and axial strains in the longitudinal reinforcement at a cross section in the shear span located 1.5 in. (38 mm) from the edge of the loading plate, and at midspan. Strains were measured with 1 in. (25 mm) electrical-resistance wire strain gages. However, for the last two specimens, T1 and T2, the data consisted only of the three loads and deflections. Photographs of the test arrangement and instrumentation are shown in Figs. 2.4 and 2.5. All strains and loads were read with a portable strain indicator.

The constituents used in the mixes for each test specimen are listed in Table 2.2, converted to a saturated surface-dry moisture state of the aggregates, i.e., SSD.

For the first five specimens, 1 through 5, mixing was done in the laboratory, using a cylindrical six-vane mixer, but one of these vanes was removed to reduce balling of fibers. The procedure in mixing consisted of adding to the mixer the required quantities of cement and aggregates, distributing the fibers to this dry mixture while the mixer was in operation, adding the water containing an air entrainer in solution, and mixing for three minutes thereafter.

The last two specimens, T1 and T2, were prepared in a drum-type mix truck. Mixing was done at a commercial batching plant, and the sequence in mixing consisted of the following: the mix truck was first loaded with

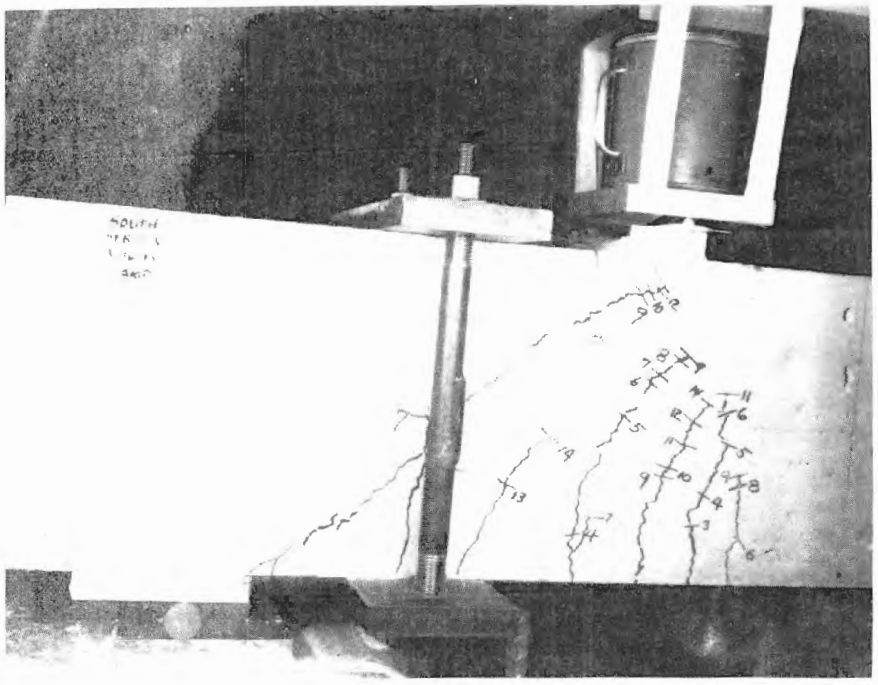

FIGURE 2.5 CLAMP USED ON ONE END OF THE BEAM TO PREVENT SHEAR FAILURE

TABLE 2.2

CONCRETE MIX QUANTITIES

Specimen	Cement[1], lb/cu yd (kg/m^3)	Sand, lb/cu yd (kg/m^3)	Gravel, lb/cu yd (kg/m^3)	Fibers, lb/cu yd (kg/m^3)	Water, lb/cu yd (kg/m^3)	Air entr. fl.oz/cu yd (cm^3/m^3)	Cement factor, sacks/cu yd (sacks/m^3)	Water/Cement by weight	Fiber content, percent by vol.
1	544 (322.5)	1629 (966.5)	1095 (649.5)	120 (71.0)	307 (182.0)	13.4 (520)	5.8 (7.6)	0.56	0.90
2	587 (348.5)	1384 (821.0)	1390 (824.5)	32 (19.0)	276 (163.5)	14.6 (565)	6.2 (8.2)	0.47	0.24
3	547 (324.5)	1638 (972.0)	1102 (654.0)	121 (72.0)	314 (186.5)	10.1 (390)	5.8 (7.6)	0.57	0.91
4	556 (330.0)	1662 (986.0)	1120 (664.5)	123 (73.0)	316 (187.5)	6.9 (265)	5.9 (7.7)	0.57	0.93
5	594 (352.5)	1400 (830.5)	1402 (832.0)	33 (20.0)	275 (163.0)	7.8 (300)	6.3 (8.3)	0.46	0.25
T1	800 (474.5)	1476 (875.5)	1065 (632.0)	200 (118.5)	469 (278.0)	none	8.5 (11.1)	0.59	1.51
T2	800 (474.5)	1476 (875.5)	1065 (632.0)	200 (118.5)	469 (278.0)	none	8.5 (11.1)	0.59	1.51

[1]Cement type I for 1 through 5; cement type III for T1 and T2.

the gravel, then portions of sand and fibers were added intermittently followed by 2/3 of the total water and the total amount of cement required; finally, the rest of the water was added in three steps to reach the desired slump. The truck arrived at the laboratory, just prior to casting, with a count of 110 drum revolutions.

The material was consolidated in the forms by external vibration, with care exercised to minimize segregation of aggregates and fibers. Occasional balls of fibers were encountered in the concrete coming from the mix truck and were removed. Table 2.3 contains the results of tests made on the fresh concrete, together with concrete ages and days of moist curing. The method of curing consisted of covering the specimens first with wet burlap, and finally with a layer of polyethelyne plastic to prevent loss of moisture; the burlap was rewet daily for seven days. At the end of this period, the specimens were exposed to the laboratory air environment of approximately 70 F (21 C) and 58 percent relative humidity until and during the beam tests.

Tests on the No. 7 grade 60 reinforcing bars used for tension steel gave a yield stress of 69.1 ksi (476.4 MPa).

2.3 TEST RESULTS

Results of the tests are summarized in Table 2.4, where the load at which the flexure-shear crack, V_{cr}, formed, the ultimate load V_u, and the failure modes are given. Flexure-shear crack formation was defined as the appearance of the first inclined crack at the advancing top of a flexure crack. First inclined-cracking load is defined as the condition at which

TABLE 2.3

CURING AND PROPERTIES OF FRESH CONCRETE

Specimen	Slump, in. (mm)	Unit weight lb/cu ft (kg/m^3)	Total air content, percent by volume	Age at time of test, days	Moist curing time, days
1	4 (100)	not taken	not taken	28	7
2	3 1/2(90)	136(2180)	8.9	29	7
3	3 1/2(90)	138(2210)	8.0	29	7
4	2 1/2(65)	140(2240)	5.8	34	7
5	2 1/2(65)	137(2200)	8.2	31	7
T1	4 1/2(115)	148(2370)	1.3	31	7
T2	4 1/2(115)	148(2370)	1.3	34	7

a (nearly vertical) flexure crack bends to an angle of about 60 degrees (1.05 rad) from the axis of the beam. The ultimate load occurred at final collapse of the beam, which was also the maximum load.

The two basic types of shear failure, shear compression and diagonal tension, were obtained in this test series. Photographs of each specimen after testing are shown in Figs. 2.6 and 2.7. Additionally, one specimen, designated 0, is shown in Fig. 2.6 which failed by shear tension. In this case, failure occurred by loss of bond to the longitudinal tension steel which was caused by insufficient anchorage as these bars did not have an end hook as in the other specimens. For this reason, the test results for this specimen were not used in the computations. In Table 2.4, the basic mode of failure for each beam is noted and additional features accompanying the failures are described.

Load-deflection curves are shown in Fig. 2.8 for all specimens except specimen 1. Deflections at the midspan and under one of the loads are shown and indicate low ductility for all specimens except T1 which had an a/d ratio of 4.4 and the highest fiber content used, 1.51 percent. The large deformation of specimen T1 relative to the others indicates more bending deformation resulting from yield of the tension steel, though failure was precipitated by an inclined crack.

Specimens 4, 5 and T1 had a/d ratios of 4.4, lengths of 12.0 in. (3050 mm) and fiber contents which ranged from 0.25 to 1.51 percent. The load-deflections at midspan are almost identical up to the collapse of 4 and 5, while the deflection of T1 continued to about 3 times that of the others, as shown below.

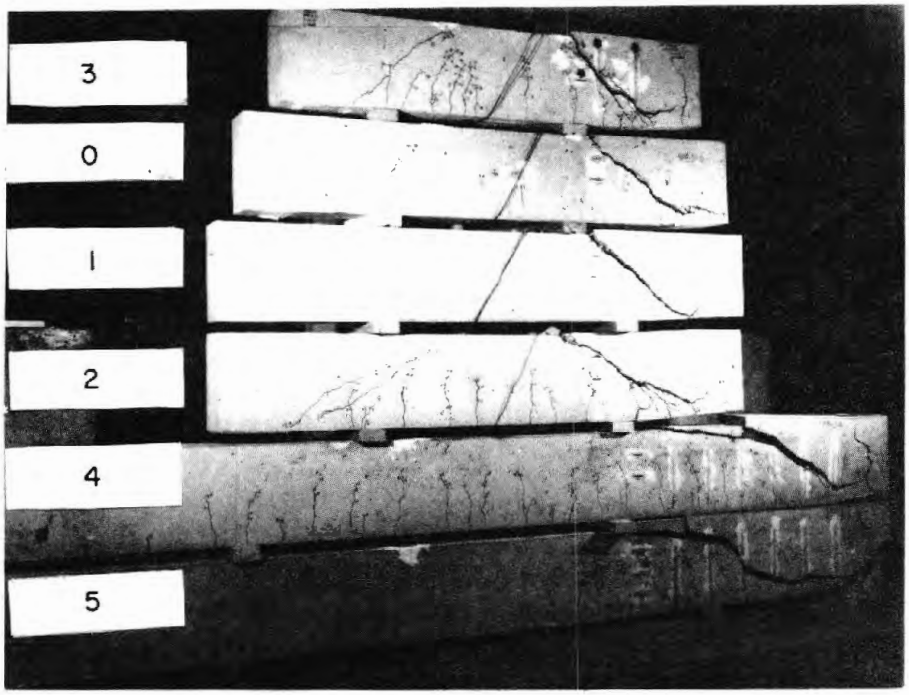

FIGURE 2.6 SPECIMENS 1 TO 5 AFTER TEST

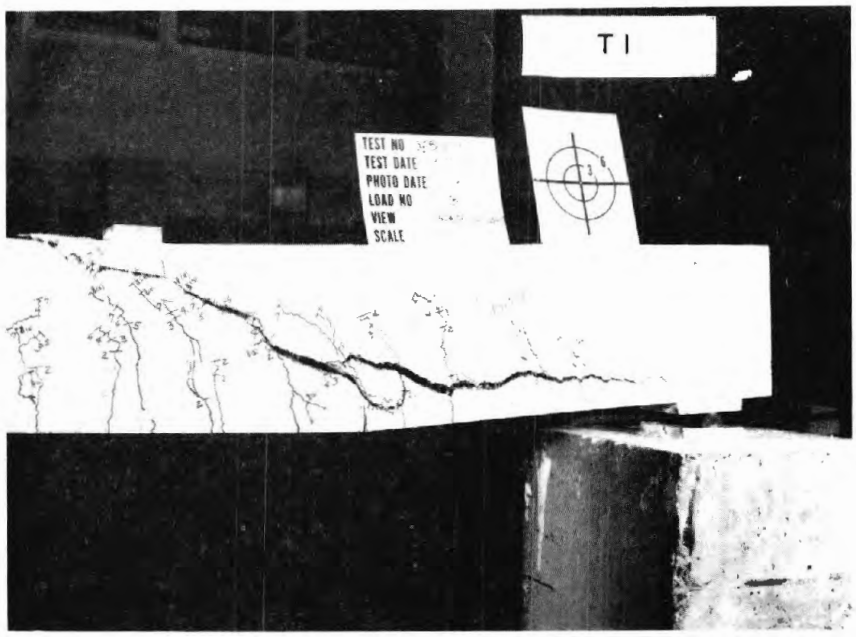

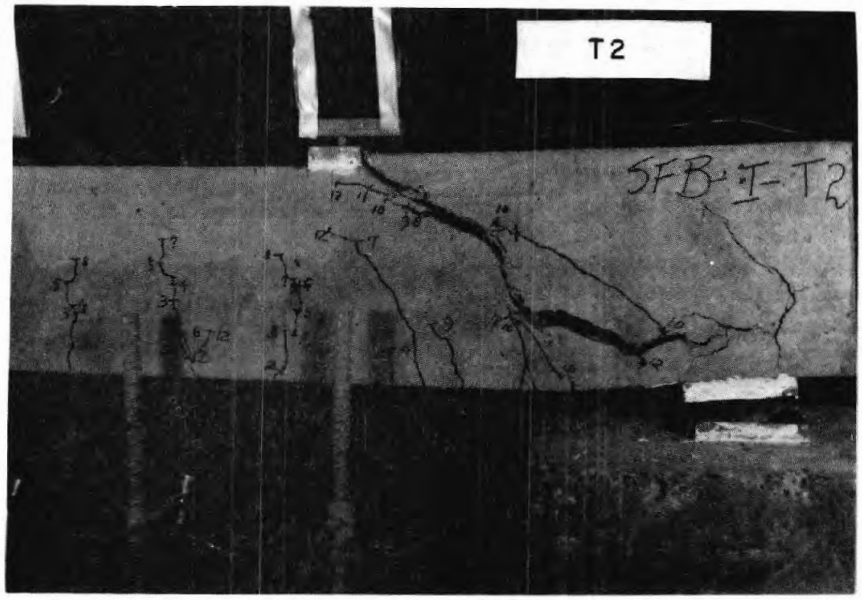

FIGURE 2.7 SPECIMENS T1 AND T2 AFTER TEST

TABLE 2.4

SUMMARY OF TEST RESULTS

Specimen	p_f, percent	$\frac{a}{d}$	V_{cr},[1] kip (kN)	V_u,[1] kip (kN)	Failure crack angle, θ, degrees (rad)	Mode of failure[2]
1	0.90	2.3	15.3 (68.0)	23.8 (106.0)	36(0.63)	SC-anchorage
2	0.24	2.3	12.2 (54.5)	26.2 (116.5)	32(0.56)	SC-anchorage crack under load
3	0.91	1.7	15.0 (66.5)	36.6 (163.0)	51(0.89)	SC-splitting and anchorage
4	0.93	4.4	11.9 (53.0)	15.4 (68.5)	29.5(0.52)	DT-splitting and anchorage. Wedge
5	0.25	4.4	10.6 (47.0)	13.8 (61.5)	27.5(0.48)	DT-splitting and anchorage. Wedge
T1	1.51	4.4	16.8 (74.5)	19.7 (87.5)	31(0.54)	DT-splitting Crack under load. Partial Wedge
T2	1.51	2.2	17.7 (78.5)	35.8 (159.0)	38(0.66)	SC-splitting and anchorage

[1]One-half the total load, including dead weight of distributing beam and test specimen.

[2]Failure Types
SC = shear compression failure
DT = diagonal tension failure
Additional Features
anchorage = splitting cracks around hook of longitudinal rebars
splitting = opening of cracks along straight portion of longitudinal rebars
wedge = appearance of triangular wedge produced by failure mechanism near load
crack under load = failure surface extended under load into flexure span

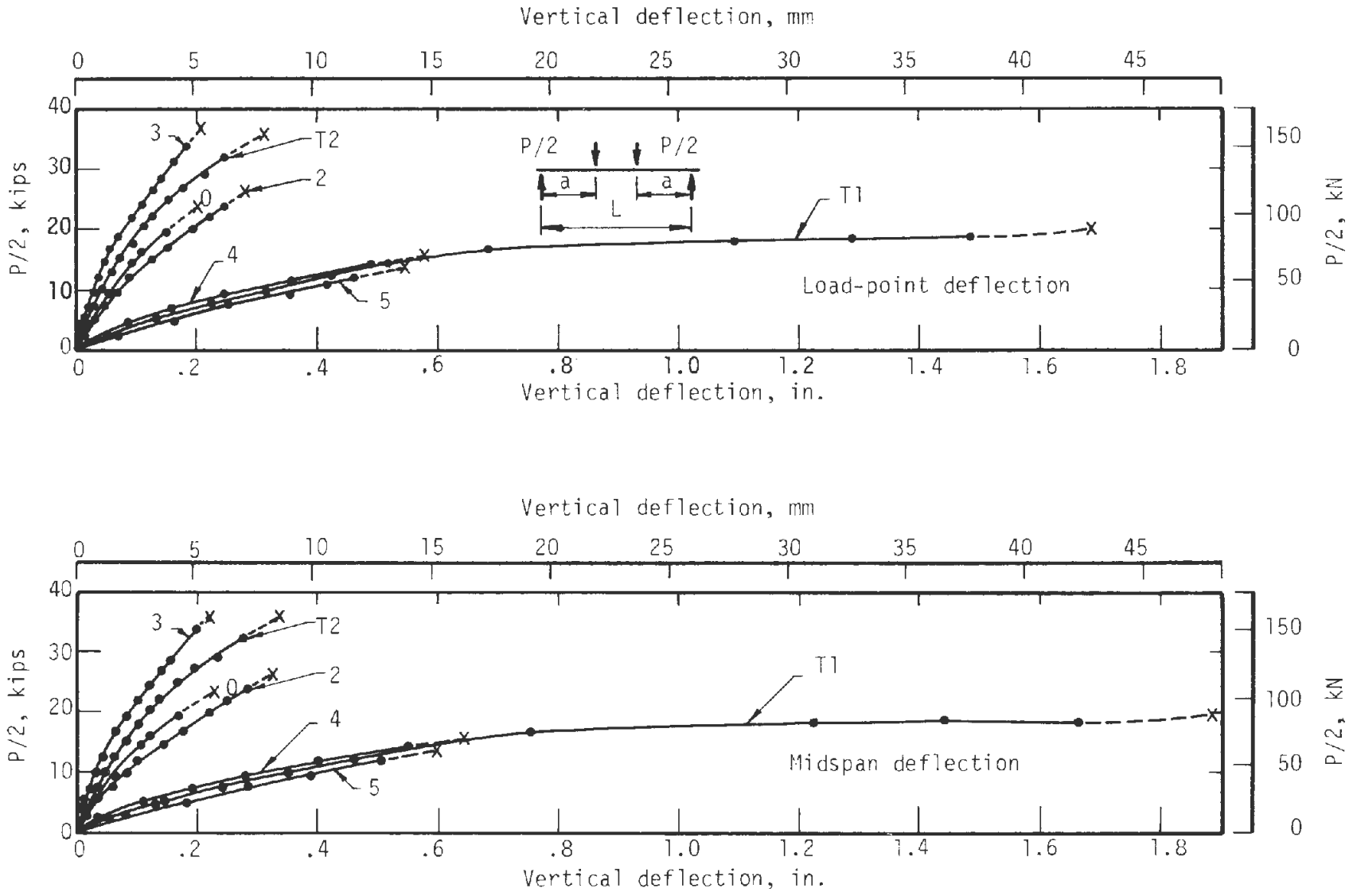

FIGURE 2.8 LOAD-DEFLECTION DIAGRAMS

Specimen	f'_c, psi (MPa)	a/d	p_f, percent	maximum midspan deflection, in. (mm)
4	5810 (40.05)	4.4	0.93	0.64 (16.3)
5	6560 (45.25)	4.4	0.25	0.60 (15.2)
T1	7950 (54.80)	4.4	1.51	1.88 (47.8)

Thus, it appears that the increase in fiber content accounts for this additional ductility by delaying the shear failure, though the higher compressive strength of T1 may also have influenced this effect.

Specimens 2 and T2 show (see table below) that for the range of a/d from 2.2 to 2.3 and length of 66 in. (1675 mm), an increase in fiber content from 0.24 to 1.51 percent does not modify the behavior of the beam to give a ductile load-deflection curve as it did for an a/d of 4.4.

Specimen	f'_c, psi (MPa)	a/d	p_f, percent	maximum midspan deflection, in. (mm)
2	5140 (35.45)	2.3	0.24	0.33 (8.5)
T2	7960 (54.90)	2.2	1.51	0.34 (8.6)

The lower group of load-deflection curves for specimens 4, 5 and T1 ended with failures that have been classified as diagonal tension while the remaining group was classified as having shear-compression failures, except for specimen 0. The load-deflection curves are grouped in the same way as the failure mode, as a consequence of the different a/d ratios. In these tests, specimens with a/d of 4.4 failed in diagonal tension while those with a/d of 2.2 and 1.7 failed in shear-compression. The appearance of the two types of failure mode may be observed in the photographs of Figs. 2.6 and 2.7.

Failure of specimens 4, 5 and T1 may be distinguished from the others in two respects, the cracking sequence and the failure crack angle. First, the crack growth from the advancing tip of the flexure cracks had become only slightly inclined near the upper one-third of the effective depth when the failure crack flattened out toward the load point forming a wedge in the shear span. Failure was sudden at this point. Second, the angle of inclination, θ, from the longitudinal axis of the member of the failure crack varied from 27.5 to 31 degrees (0.48 to 0.54 rad), increasing slightly with fiber content (Table 2.4). In reference to the second group (specimens 1, 2, 3, T2), inclined crack growth was more gradual and continuous up to a load at which the crack essentially stopped advancing for a few load increments before failure. At failure, the crack terminated in crushing near the loading block for beams 1, 2, and 3; for T2 crushing was not so obvious, but the inclined crack advanced through the compression region. In all cases, the course of failure was more progressive and predictable than for the diagonal tension failures, though it was still explosive at the final stage. For specimens 1, 2, and T2, inclination of the failure surface from the beam axis varied from 32 to 38 degrees (0.56 to 0.66 rad) with the angle increasing with fiber content. For the final specimen in this group, specimen 3, an angle of 51 degrees (0.89 rad) was obtained, which falls in the range of inclination for deep beams as summarized by the ASCE-ACI Task Committee 426 (1973) for nonfiber concrete. This is indicative of a third mode of failure typically associated with shear behavior of deep beams.

Strains in the tension steel at midspan and in the shear span

1.5 in. (38 mm) from the edge of the loading block are shown in Fig. 2.9 for specimens 0, 1, 2, 3, 4 and 5. The strains at failure of the beams are compared with the yield strain of 2350 psi and show that only the steel in specimen 4 in this group passed the yield point of the steel, and only by about 300 μ. It may be concluded that the tension steel in specimen T1 was well into the yield range at failure since the deflection was larger than that for specimen 4.

2.4 DISCUSSION

Results of the beam tests are summarized in Fig. 2.10 where the shear loads at first inclined cracking and ultimate are divided by $b_w d \sqrt{f'_c}$ and plotted against the a/d ratio. This graph shows a strong influence of the parameter a/d on the results; the effect of different compressive strengths is taken into account by modifying the nominal shear stress $V_c/b_w d$ by the square root factor. With so few tests, conclusions drawn must be tentative, but certain trends can be noted. At the large a/d ratio of 4.4, steel fiber content influenced the ultimate shear capacity as expected, with an increase in capacity with fiber content; however, the effect is not shown as conclusively for a/d ratios of 2.2 to 2.3.

First inclined cracking is difficult to detect in the tests, because cracking is progressive. The shear stress influences the flexure cracking from the start causing it to be somewhat inclined, but at first this influence is negligible. When the crack should be considered inclined depends on the judgment of the observers. In these tests, first inclined cracking load was considered to occur when the crack became inclined about

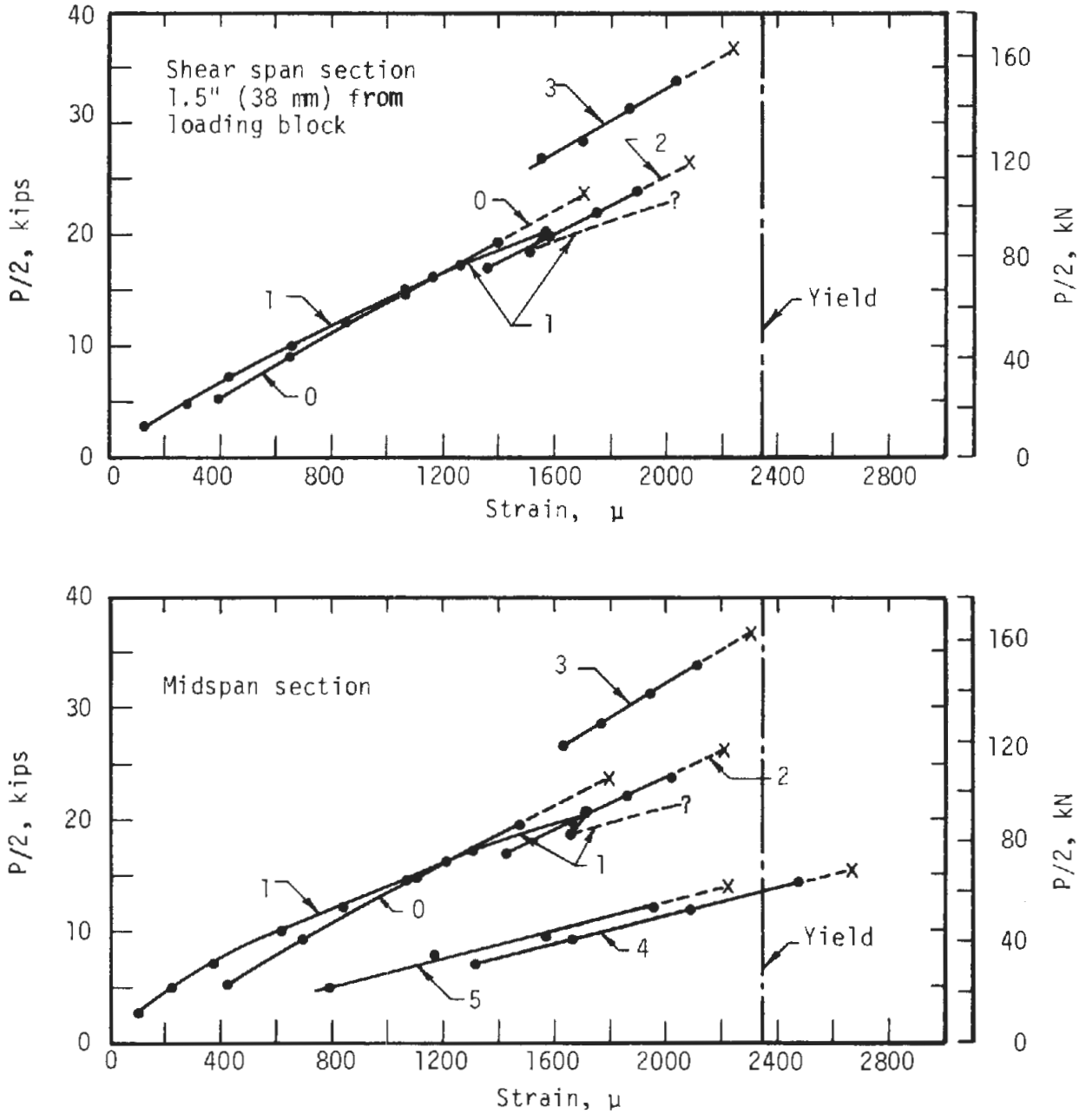

FIGURE 2.9 VARIATION OF STRAIN IN THE TENSION STEEL WITH SHEAR FORCE

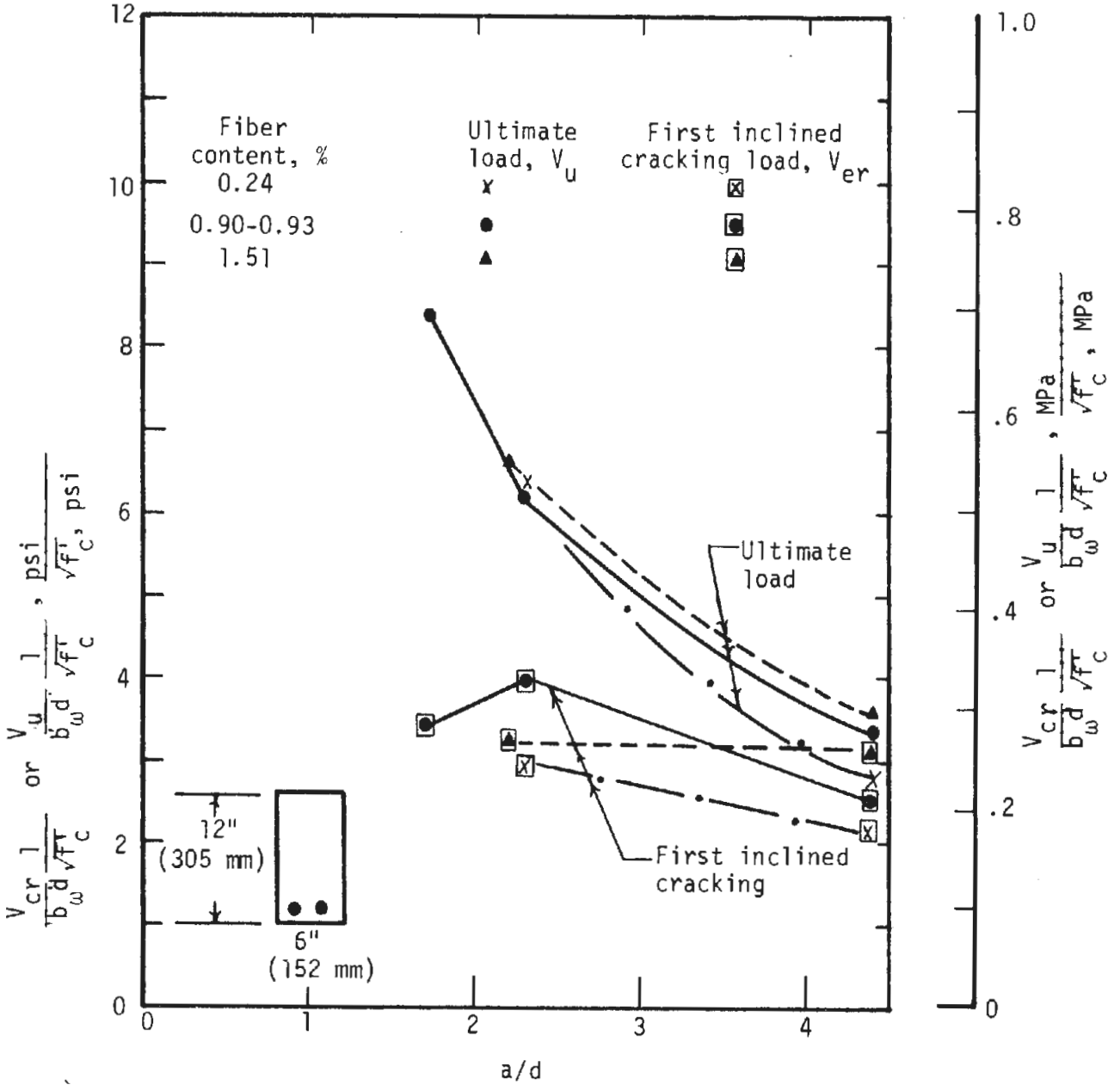

FIGURE 2.10 INFLUENCE OF a/d RATIO ON THE TEST LOADS

60 degrees (1.05 rad) to the axis of the beam. The first inclined cracking loads appear more erratic than the ultimate loads in Fig. 2.10. This reflects the observer's judgment and the scatter in the concrete tensile strength. These loads show a tendency to increase with decreasing a/d ratio as expected, since this ratio is a measure of the relative amounts of moment and shear, but the variation of first cracking load is not nearly as marked as it is for ultimate load. However, at an a/d ratio of 4.4 the first inclined crack load increases with steel fiber content, because the concrete-fiber composite tensile strength increases with fiber content.

A series of beam tests is reported by Batson, Jenkins and Spatney (1972), in which some of the beams failed in shear. Comparison of the present tests with one group of results reported by those authors is of interest because of the similarity of the results, in spite of the many differences in the test specimens. The tests were on beams containing 0.22 to 1.76 percent by volume of rectangular-section crimped fibers. The cross sections of the fibers were 0.016 x 0.010 in. (0.41 x 0.25 mm) and 0.015 x 0.025 in. (0.38 x 0.64 mm), and the lengths were 0.75 and 1.0 in. (19 and 25 mm), respectively. Concrete compressive strengths varied from 4817 psi (33.20 MPa) to 5830 psi (40.20 MPa). Figure 2.11 shows the shear stress as a function of a/d for the present tests and the range of data for the group of tests cited. The same trend is observed in the data and the scatter appears well within the range expected for shear failures of beams. The shear stress used in this comparison is calculated in the same manner

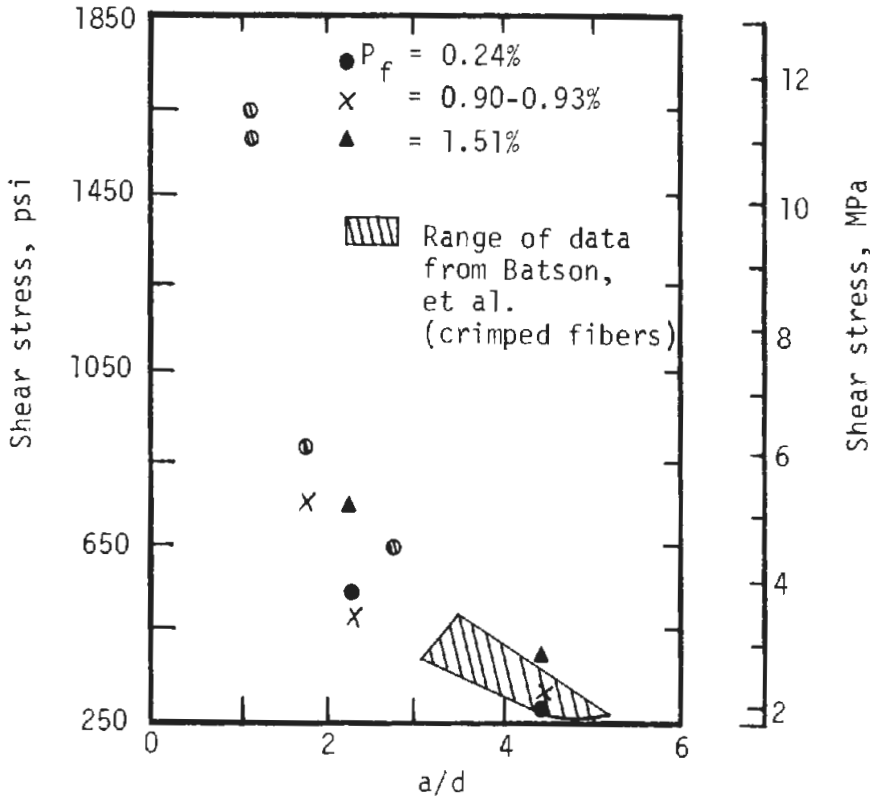

FIGURE 2.11 COMPARISON WITH OTHER TESTS OF SHEAR STRESS AT MAXIMUM LOAD

suggested by Batson, et al. and was determined by the formula VQ/It at the neutral axis of the beam in the shear span, where

V = shear force

Q = first moment of area above the neutral axis about the neutral axis

I = second moment of the uncracked, transformed area of the section

t = width of the beam

Building Code Requirements for Reinforced Concrete (ACI-318-71) (1971) contains a formula for defining the allowable shear capacity of conventionally reinforced concrete beams without special shear reinforcement in terms of stress.

$$v_c = 1.9\sqrt{f'_c} + 2{,}500\,\rho_w \frac{V_u d}{M_u} \leq 3.5\sqrt{f'_c}\ , \text{ psi} \qquad (2.1)$$

$$v_c = 0.1578\sqrt{f'_c} + 17.24\,\rho_w \frac{V_u d}{M_u} \leq 0.2906\sqrt{f'_c}\ , \text{ MPa} \qquad (2.1\text{-SI})$$

The allowable load corresponding to this stress is given by $V_c = v_c b_w d$, where

V_c = total allowable shear force resisted by the concrete at the section

v_c = allowable shear stress resisted by the concrete at the section

d = effective depth of the beam

b_w = web width or width of a rectangular beam

$\rho_w = A_s/(b_w d)$

A_s = area of tension steel reinforcement

V_u = total applied design shear force at section

M_u = applied design load moment at a section

f'_c = specified compressive strength, psi in English system and MPa in SI system of units

$\sqrt{f'_c}$ = square root of f'_c, but the units remain psi in English system and MPa in SI system of units.

Formula 2.1 may be divided by $\sqrt{f'_c}$ to give

$$\frac{v_c}{\sqrt{f'_c}} = \frac{V_c}{b_w d\sqrt{f'_c}} = 1.9 + \frac{2500\,\rho_w}{\sqrt{f'_c}}\,\frac{V_u d}{M_u} \leq 3.5 \qquad (2.2)$$

$$\frac{v_c}{\sqrt{f'_c}} = \frac{V_c}{b_w d\sqrt{f'_c}} = 0.1578 + \frac{17.25\,\rho_w}{\sqrt{f'_c}}\,\frac{V_u d}{M_u} \leq 0.2906 \qquad (2.2\text{-SI})$$

It is desirable to evaluate the shear strength of steel fiber reinforced concrete beams in these same terms in order to compare the strength with conventional beams, and to determine whether the same procedure, and perhaps the same formula with slight modifications, can be used for design purposes. One problem with the comparison is that the tensile capacity of fiber concrete varies with fiber content and is not reflected well by the compressive strength. Thus, if tensile strength affects the shear capacity, a different formula is needed for each fiber

content. To avoid this, the formula can be changed to depend on the modulus of rupture, f_r, which will then reflect the effect of fiber content. The formula for conventional beams will not be changed if a constant relation is assumed between f'_c and f_r. A reasonable relation for conventional concrete is $f_r = 7.5\sqrt{f'_c}$, psi ($0.6228\sqrt{f'_c}$, MPa). With this substitution into Eq. 2.2, the formula is unchanged for conventional beams and becomes applicable to fiber reinforced beams.

$$\frac{v_c}{\sqrt{f'_c}} = \frac{V_c}{b_w d}\,\frac{7.5}{f_r} = 1.9 + \frac{2500(7.5)}{f_r}\,\frac{\rho_w V_u d}{M_u} \leq 3.5$$

$$\frac{V_c}{b_w d}\,\frac{7.5}{f_r} = 1.9 + \frac{18750}{f_r}\,\frac{\rho_w V_u d}{M_u} \leq 3.5 \qquad (2.3)$$

At the capacity of the beam, the resisting shear on the left side of the equation (V_c) is taken equal to the design shear on the right (V_u). In Fig. 2.12, the dimensionless variable on the left of the equation which is a function of shear capacity is shown as the ordinate and the dimensionless variable on the right is shown as abscissa for nonfiber concrete beams. The equation applies over a part of the range of abscissa, after which the limit becomes active. The formula is based on a fit of data consisting of 194 beam tests (Journal of the ACI, 1962) of constant cross section and subjected to one or two concentrated loads in any one span (diagonal tension cracking occurs in a region of constant shear). The outline of points representing the data is shown in Fig. 2.12 also, where it can be compared with the formula. There is considerable scatter in the data and no distinction is made in the type of failure that occurred. The formula is near the

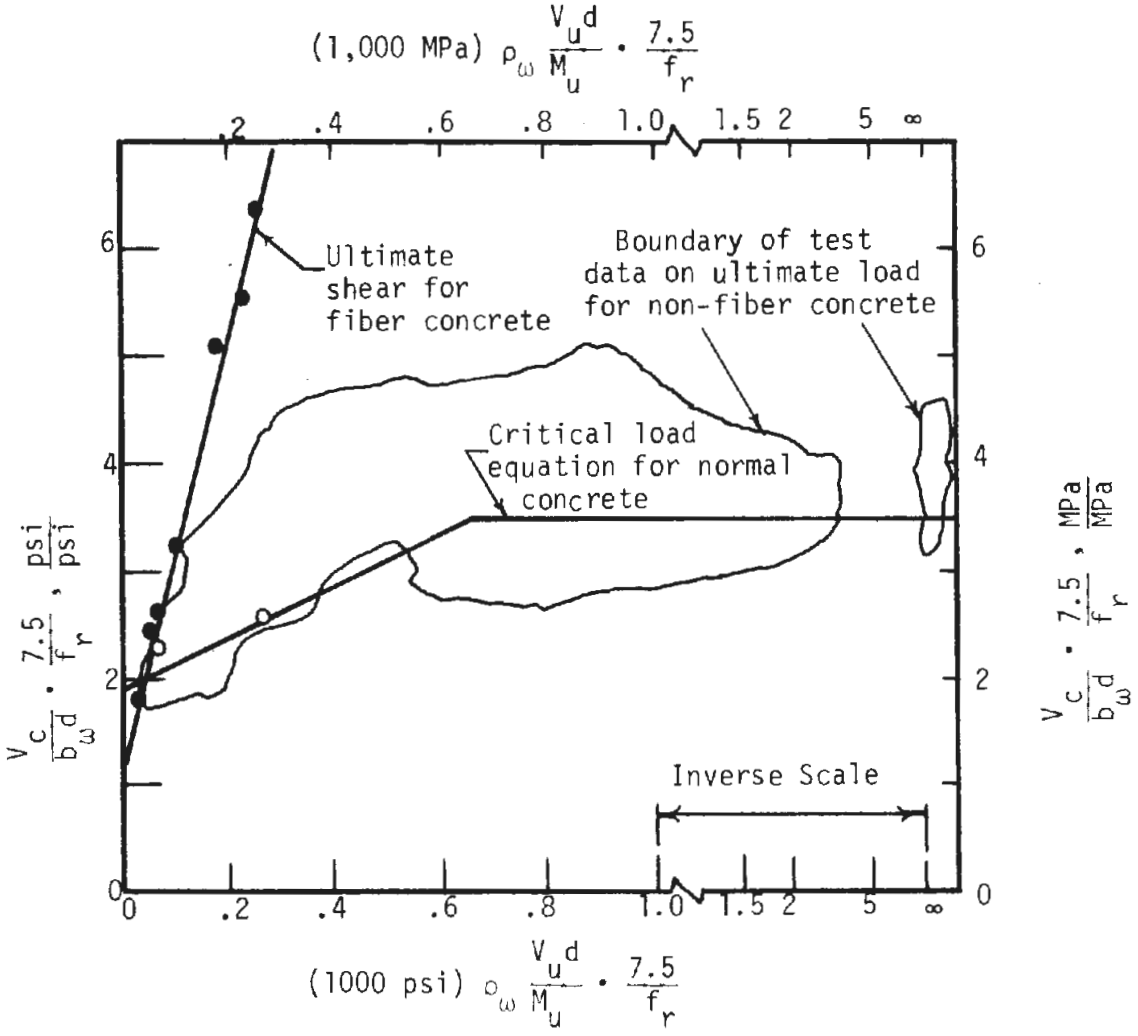

FIGURE 2.12 COMPARISON OF TEST DATA FOR FIBER CONCRETE WITH DATA FROM ACI-ASCE COMMITTEE 326 (1962)

lower limit of the data at the left side of the graph which corresponds to large values of a/d in the range in which diagonal tension failures are more likely to occur. As discussed in the last section, these types of failure are more sudden and give less warning so greater conservatism is desirable. Values of the abscissa from 0.6 and larger apply to deep beams. It is also important to note that a particular procedure was used to define the moment-shear ratio (M_u/V_u) used for plotting the data, in an effort to define the section at which failure actually occurred in a consistent manner. This definition may be expressed symbolically as shown below, which basically considers the moment at the distance d from the load point:

$$\frac{M_u}{V_u} = \left(\frac{M_{max}}{V_u} - d\right) \geq \left(\frac{M_{max}}{V_u} - \frac{a}{2}\right)$$

where

M_{max} = maximum moment in the shear span considered

a = length of shear span defined as the distance between a concentrated load and the nearest reaction, that is, length or a region of constant shear

The same definition of critical section was used in comparing the tests in this program with the ACI formula.

The ultimate loads obtained in the 7 tests are shown on the graph of Fig. 2.12, and indicate a significant increase in shear capacity over those made of conventional concrete except for very low values of the

abscissa at the left edge of the graph. In this range, the beams are long, shallow and tend to fail in flexure as well as shear. The lowest test point, the one that falls below the ACI formula curve, corresponds to specimen T1; this beam had yielded in flexure with a deflection of 1.88 in. (47.8 mm) before it failed in shear. It is questionable to consider this a shear failure as the shear capacity would have been higher if the failure section had not already yielded and deformed a great deal in flexure.

A straight line fit to the test points can represent a reasonable prediction tool for ultimate shear capacity of the fiber-reinforced test beams.

$$\frac{V_c}{b_w d}\ \frac{7.5}{f_r} = 1.07 + 20{,}700\ \rho_w \frac{V_u d}{M_u}\ \frac{7.5}{f_r}$$

$$\frac{V_c}{b_w d}\ \frac{7.5}{f_r} = 1.07 + 155{,}000\ \frac{\rho_w V_u d}{f_r M_u} \qquad (2.4)$$

The straight line represented by this formula is shown in Fig. 2.12, and represents the test data quite well. There should be an upper limit placed on the capacity, as in the case of conventionally reinforced beams, but it is not possible from the data to establish such a limit.

Axial compression in a member, combined with bending and shear, tends to increase the shear capacity. A simple method for taking thrust into account is given in Building Code Requirements for Reinforced Concrete (1971) that would calculate v_c from the formula

$$v_c = 2(1 - .0005 \frac{N_u}{A_g}) \sqrt{f'_c} \leq 3.5 \sqrt{f'_c} \sqrt{1 + .002 \frac{N_u}{A_g}} \quad (2.5)$$

where

N_u = design axial load normal to the cross section occurring simultaneously with V_u, to be taken as positive for compression, and to include the effects of tension due to shrinkage and creep, lbs

A_g = gross area of section, $in.^2$

The amplification factor used in Eq. 2.5 allows the increase of unit shear stress, up to a limit, by the factor

$$(1 + 0.0005\ N_u/A_g) \quad (2.6)$$

$$(1 + 0.072519\ N_u/A_g), \quad (2.6\text{-SI})$$

and will always result in an increase in shear capacity due to thrust. In the absence of data on the effect of axial force on shear capacity for steel-fiber-reinforced members it is suggested that this approximate relation for conventional concrete members may be applied, though it is not possible at this time to determine what the limit should be.

A waffle-type segmented liner can reasonably be considered a T-beam if the flanges on either side of the segment are considered to form the stem of the T. Building Code Requirements for Reinforced Concrete (1971) treats T-beams by taking the stem width to be the width of the beam for shear calculation purposes. This is a conservative approach, and the ACI-ASCE Task Committee 426 (1973) discusses data that indicates addition

of the flange to a beam while keeping the same beam (web) width, may increase the ultimate shear capacity as much as 25 percent. A proposed means of taking into account the added shear strength of the flange is presented by the committee; this modification takes the form

$$V_c = v_c (b_w d + 2 h_f^2) \qquad (2.7)$$

where h_f is the depth of the compression flange. This approach adds to the basic shear area of the rectangular beam an area of the flange on each side of the web; this area is a square with dimensions equal to the depth of the flange. This is a reasonable approach for segmented liners that will give a more realistic value when compared with the actual shear loads at failure. This correction should only be applied when the moment causes the flange of the T section to be in compression. If the moment is in the other direction, the basic rectangular beam area should be used.

A single equation can be obtained by combining Eqs. 2.4, 2.6 and 2.7 to predict the shear capacity of steel-fiber-reinforced members with thrust, moment and shear.

$$V_c = (b_w d + 2h_f^2) \frac{f_r}{7.5} \left[1.07 + 155000 \frac{\rho_w}{f_r} \frac{V_u d}{M_u}\right] \cdot \left(1 + 0.0005 \frac{N_u}{A_g}\right) \qquad (2.8)$$

$$V_c = (b_w d + 2h_f^2) \frac{f_r}{7.5} \left[1.07 + 155000 \frac{\rho_w}{f_r} \frac{V_u d}{M_u}\right] \cdot \left(1 + 0.072519 \frac{N_u}{A_g}\right) \qquad (2.8\text{-SI})$$

where h_f is taken as zero if bending is in the direction that would cause the flange to be in tension (tension on the outside of segmented tunnel liners); f_r and $\frac{N_u}{A_g}$ have the units of psi in the English system of units, and MPa in the SI system. Use of this equation will be discussed further in Chapter 4.

CHAPTER 3

TESTS OF BOLTED REINFORCED CONCRETE CONNECTIONS

3.1 INTRODUCTION

A series of 5 tests that simulated the type of joint used in the longitudinal direction of bolted reinforced concrete segmented tunnel liners are described in this chapter. The joints were subjected to moment and thrust with essentially constant eccentricity. The purpose of these tests was to investigate the structural behavior of the joint in terms of the moment-rotation relationship, load-carrying capacity, failure mode, and magnitude of the load carried by the bolts. In addition, the feasibility of replacing part of the conventional reinforcement and ties with randomly oriented steel fibers was investigated. The objective of the testing program was to provide information which would enable one to assess the effects of the joint on the overall behavior of the tunnel liner. The joints tested were of similar configuration to those used in the large-scale segmented tunnel liner tests described in Chapter 4. Thus, the behavior of isolated joints can be compared with the behavior of similar joints in a full ring.

The part of the joint specimen representing the segment was straight rather than curved as would occur in a tunnel liner, and a block of concrete was cast on each end of the specimen as shown in Fig. 3.1. This arrangement made it possible to apply loads parallel to the centroidal plane but eccentric in either direction in a standard testing machine. The

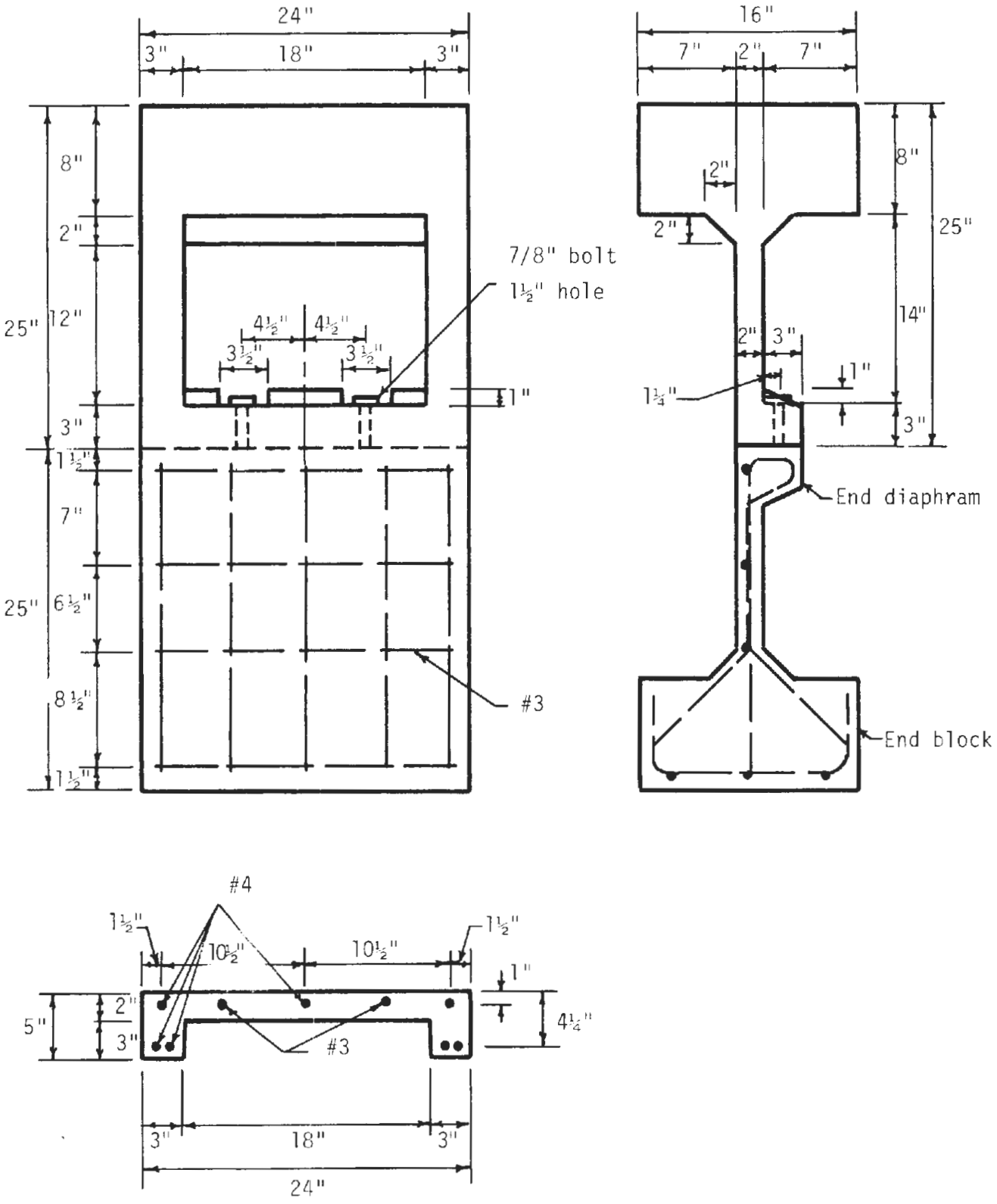

FIGURE 3.1 JOINT TEST SPECIMEN

concrete from which each specimen was cast contained 1.0 percent by volume of steel fibers and had a compressive strength of 6000 to 8800 psi (41.35 to 60.65 MPa).

In designing the test specimen it was decided that the joint proper would have only the main reinforcement extended into it and all conventional additional shear reinforcement and ties would be omitted. Consequently, the strength of the fiber concrete would limit the strength of the joint. With the strength of this basic design determined by test, additional reinforcement could be provided in future designs to increase the capacity of the joint to a value greater than that of the segment. Addition of reinforcement in the joint proper may increase the stiffness of the joint as well as the strength, so care should be exercised in the application of moment-rotation data obtained from these tests to future designs.

From the tests it was found that the joint behavior was fairly ductile. The mode of failure was different depending on the direction of eccentricity of the applied load and the ultimate load could be predicted with reasonable accuracy.

One major problem associated with segmented tunnel liners is water-tightness of the joints. Water-tightness is influenced by the opening of the joint during deformation. In these tests, joint openings were measured to obtain information which can be used in future waterproofing studies.

3.2 DESCRIPTION OF TESTS AND TEST SPECIMEN

The overall dimensions and steel bar reinforcement layout of the

joint specimens is shown in Fig. 3.1. The joint is similar to that reported by Gamble (1967) except that the overall dimensions have been scaled by a factor of 0.525 and the shear and tie bar reinforcement were omitted. This reinforcement was replaced with one volume percent steel fiber. The fiber used is the same U.S. Steel fiber (Fibercon), described in Chapter 2. In some cases the dimensions could not be scaled precisely by the scale factor because minimum cover requirements for the reinforcement would be insufficient. In these cases, the minimum cover was maintained. The resulting segment is five inches thick (127 mm) and has a shell or flange which is two inches (51 mm) thick. The end-diaphragm of the segment, which is connected with bolts to the adjacent segment, is three inches thick (76 mm).

Concrete blocks cast on the ends of the specimen for applying eccentric load were heavily reinforced to prevent failure or deformation. The segments were bolted together with 7/8-in. diameter (22 mm) A325 bolts that were eight inches (203 mm) long. Hardened washers which were flat and regular with inside diameter of 15/16 in. (24 mm) and outside diameter of 2-1/4 in. (57 mm) were used under the bolt head and nut. For three tests the bolts were tightened to a torque of 100 ft-lbs (136 N•m) and in the remaining two tests 150 ft-lbs (203 N•m) was used. Standard deformed reinforcing bars with a nominal yield stress of 50 ksi (344.5 MPa minimum yield stress) were used in the segments. Typical stress-strain curves from tensile tests of representative bars are shown in Fig. 3.2. The concrete mix used was:

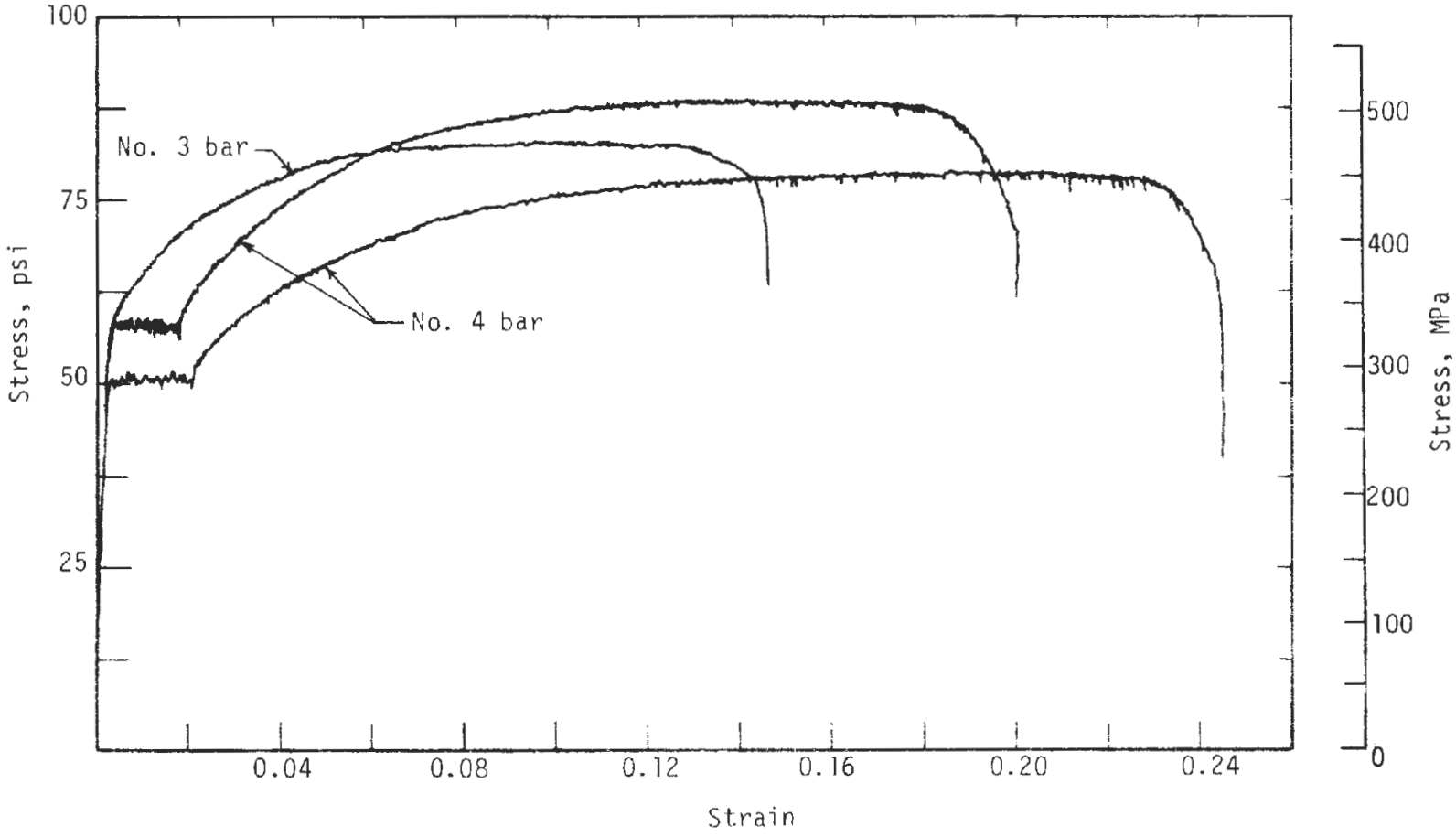

FIGURE 3.2 STRESS-STRAIN CURVES FOR REINFORCING BARS

CONCRETE MIX

Specimen number	lb/cu yd (kg/m^3)				
	Cement	Sand	Gravel	Water	Fiber
J-1,2	631 (274.5)	1760 (1044.0)	1182 (701.5)	381 (226.0)	132 (78.5)
J-4,5,6	599 (3.55.5)	1758 (1043.0)	1176 (697.5)	420 (249.0)	132 (78.5)

Standard control specimens were tested from each batch of concrete and the results are shown in Table 3.1. The two halves of each specimen were cast at the same time from the same batch of concrete mixed in a 1/4-cu yd (0.20 m^3) rotary mixer.

TABLE 3.1

CONCRETE STRENGTHS AND TEST HISTORY

Specimen number	Test age, days	Compressive strength, psi	Splitting tensile strength, psi	Modulus of rupture, psi
J-1	48	8,480	795	960
J-2	44	8,830	820	910
J-4	49	6,000	680	810
J-5	49	6,480	690	920
J-6	50	6,380	715	782

Eccentric load was applied in a MTS hydraulic testing machine through a series of steel plates with a roller on each end of the specimen. A drawing of the loading system and a photograph is shown in Fig. 3.3. The series of plates at each end of the specimen were designed to apply a load to the specimen as uniformly as possible. Load eccentricities measured from the plastic centroid of the segment section were 0.00, +2.66, +4.66, -3.31, and -5.31 in. (0.0, +67.6, +118.4, -84.1, and -134.9 mm). Positive eccentricity is taken as that which causes compression on the shell of the segment (Fig. 3.3).

Loads in the bolts were measured by installing two strain gages on the shank of each bolt. They were placed opposite one another to obtain the average stress without bending. Lead wires for the strain gages were placed in a slot in an extra washer placed on the nut end of the bolt. The bolts were tightened with a torque wrench and the corresponding strain measured. Strain in the bolts was monitored with a portable strain indicator and the relation between torque and bolt load was obtained.

Rotation of the joint was measured by the device shown in Fig. 3.4. This device consisted of two steel frames which were clamped to the sides of the specimen twelve inches (305 mm) apart, or six inches (152 mm) on either side of the joint. Linear variable differential transformers (LVDT) were used to measure the relative movement at each end of the frames. During a test the sum of the LVDT movements was automatically plotted against load measured by the testing machine on an XY-recorder. The measured rotation is that of the joint plus some part of the segment on each side of the joint. The opening of the joint was measured with a two-inch

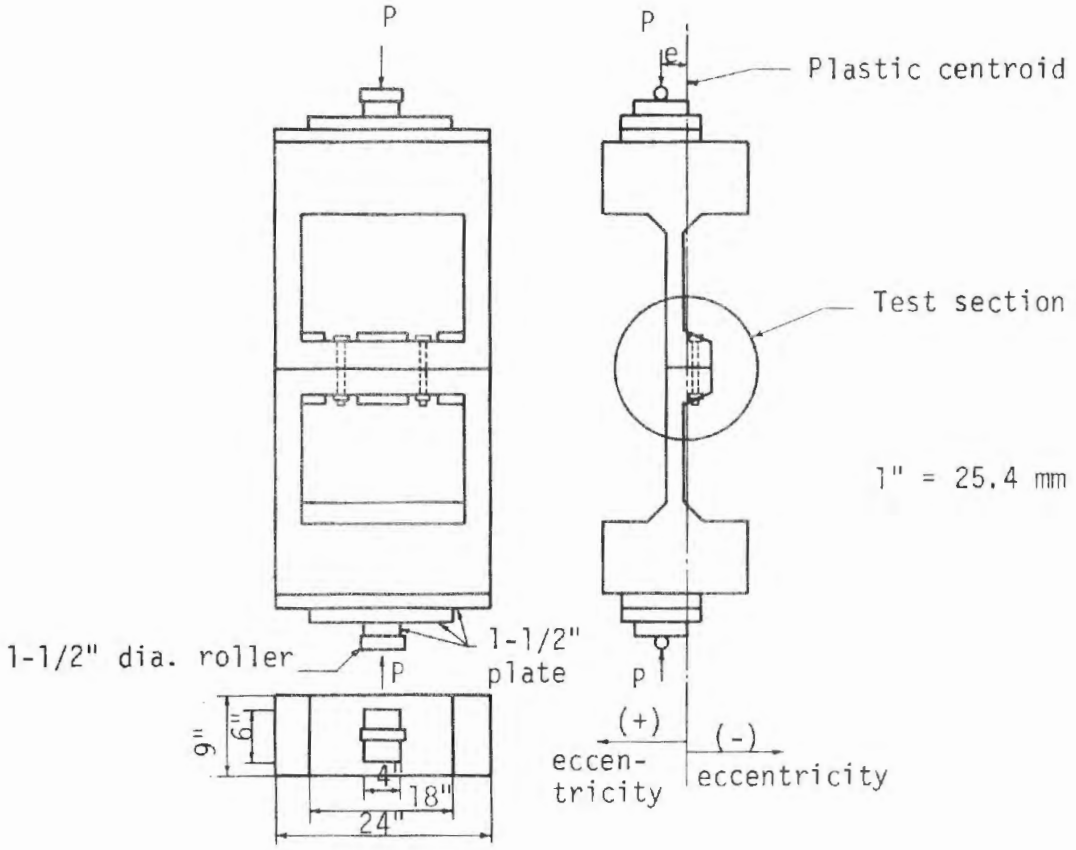

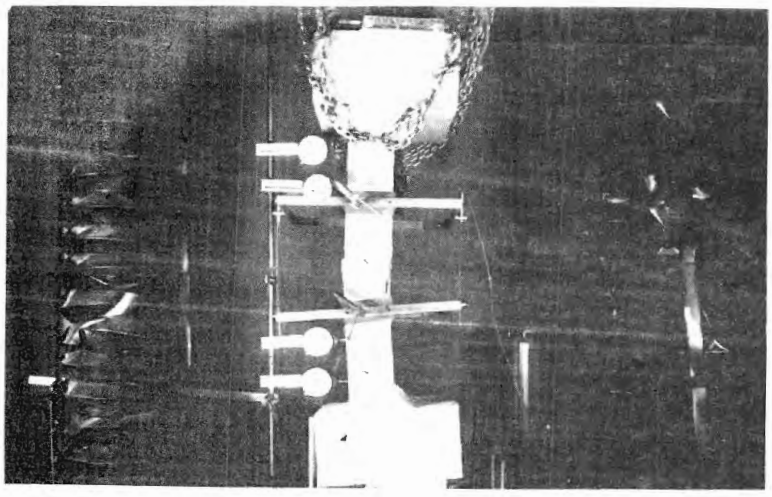

FIGURE 3.3 TEST ARRANGEMENT FOR CONCRETE SEGMENT JOINT TESTS

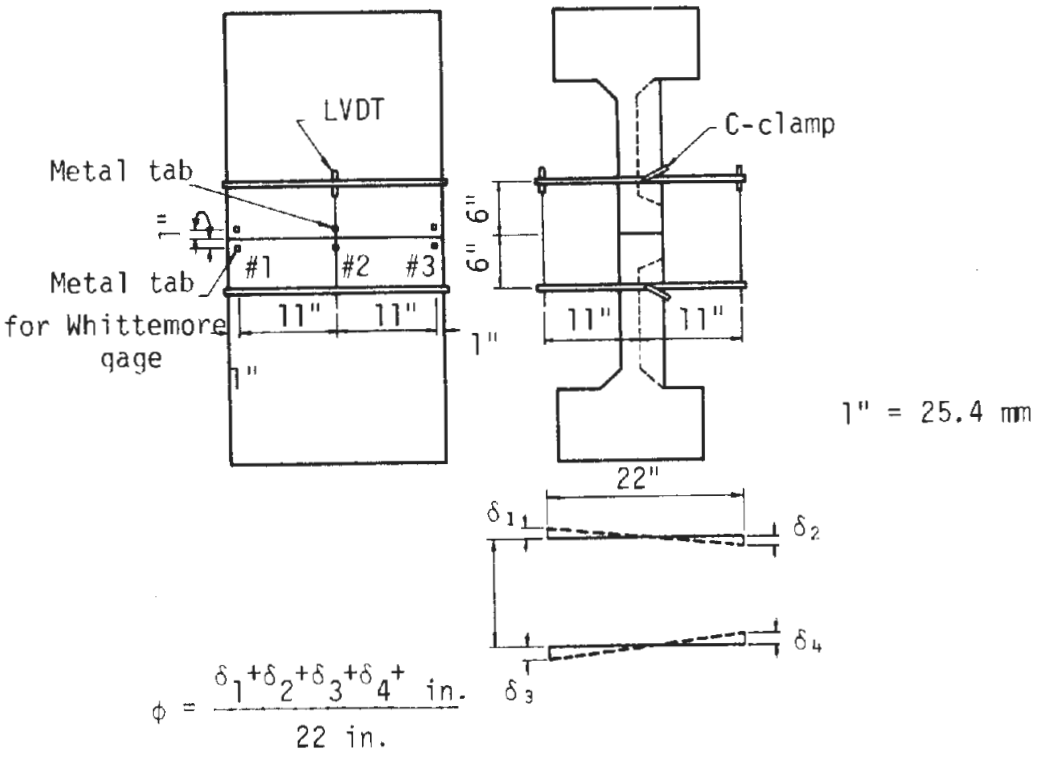

FIGURE 3.4 DEVICE FOR MEASURING THE JOINT ROTATION

(50.8 mm) gage length Whittemore gage by determining the change in the spacing of gage points on metal tabs which were glued to the concrete on each side of the mating surface of the joint. The measurements of joint openings were taken near each end and at the center of the joint as shown in Fig. 3.4.

The overall bending deformation of the specimen was measured with five mechanical dial gages which had a four-inch (102 mm) range and 0.001 in. (0.03 mm) dial divisions. The dial gages were located at the joint surface, and 9 in. (229 mm) and 14 in. (346 mm) on either side of

it. Four of the gages may be seen in the photograph of Fig. 3.3. The primary purpose of these measurements was to provide deformations of the specimen so that the moment at the joint could be corrected for secondary effects.

In general, load was applied in 5-kip (22-kN) increments and all measurements were taken after each increment.

The form used for these specimens was made of wood and is shown in the photograph of Fig. 3.5. The "as cast" mating surfaces of the joints were not true. When the specimens were put together, a gap resulted over part of the mating surface. In some cases it was felt that the gap was too large to represent what would actually be allowed in service. On the other hand, it would not be desirable to grout the joint, completely filling the

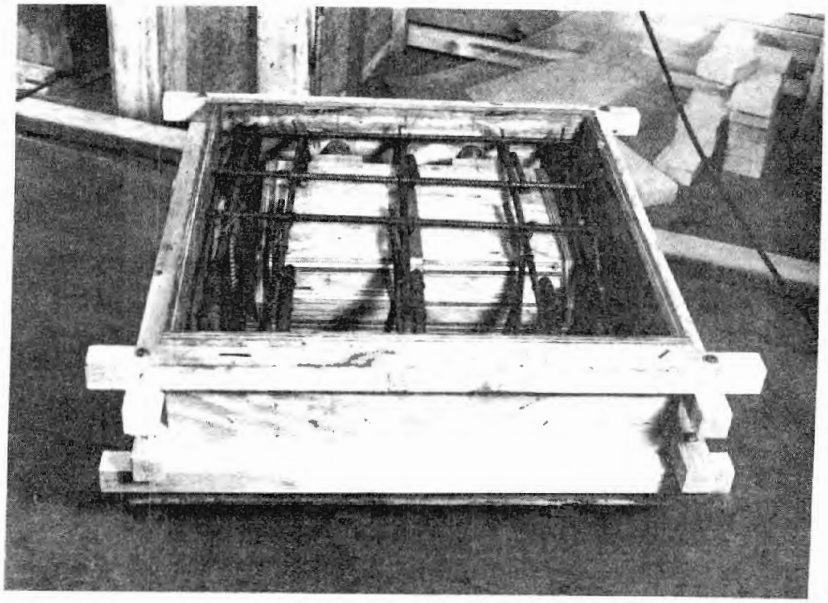

FIGURE 3.5 FORM USED FOR THE JOINT SPECIMENS

gap because the fit might be too good to represent that occurring in actual service. Therefore, the mating surface of each half of a specimen was covered with a very thin coating of grout, and a piece of steel plate was placed on the surface until the grout set. The joint was then bolted together. It was found that the fit was good, but not perfect and contact over the mating surface could be obtained by tightening the bolts. The gap which resulted before the bolts were tightened was on the order of one to two thousandths of an inch, measured with a feeler gage.

3.3 TEST RESULTS

3.3.1 POSITIVE ECCENTRICITY

Specimens J-1 and J-2 had initial positive eccentricities (shell in compression) of 2.66 in. and 4.66 in. (67.7 mm and 118.4 mm) respectively, measured from the calculated plastic centroid of the segment section with its longitudinal reinforcement as shown in Fig. 3.1(b). As the loading progressed and bending of the specimen occurred, the eccentricity changed slightly. This effect was considered by measuring the deformation and correcting the eccentricity when the moments were computed. Opening of the joint across the mating surface of the two specimens is shown in Fig. 3.6. Measurements made near the ends of the joints and at the center give a good indication of the behavior. The measurements show very little opening at the center (curve 2), while near the ends (curves 1 and 3) the joint continued to open throughout the loading history. The bolts held the end diaphragms of the segment together near the center, while the webs at

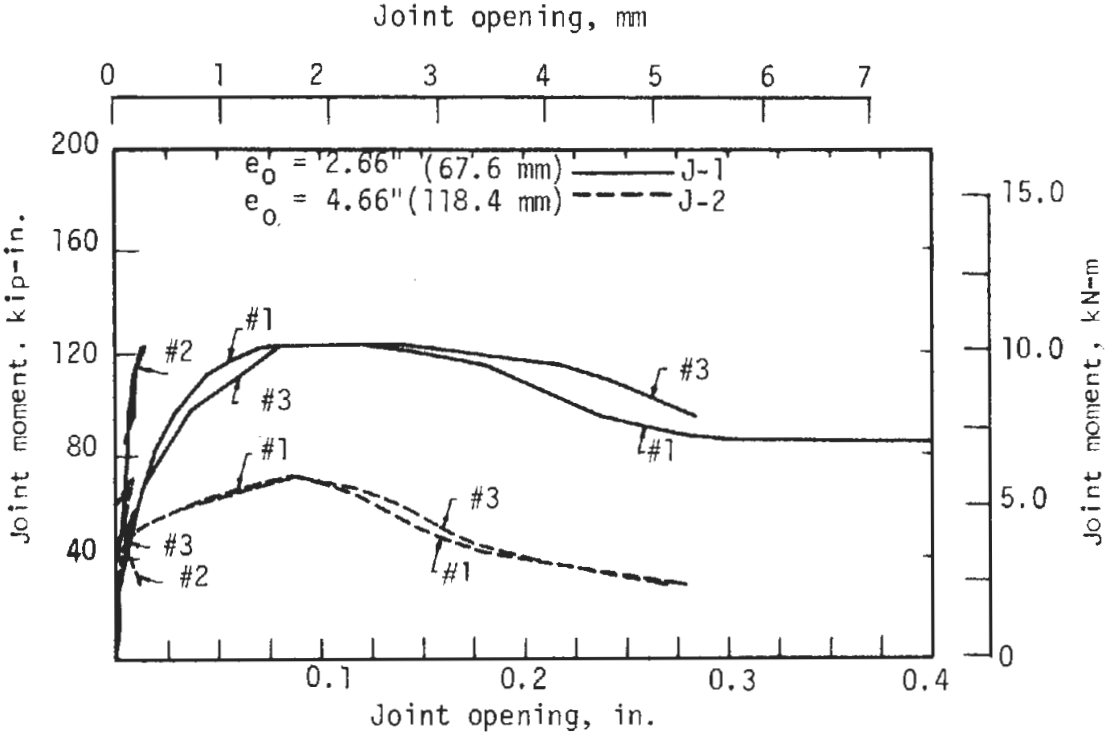

FIGURE 3.6 JOINT OPENING-MOMENT FOR TESTS J-1 AND J-2

the sides were torn away from the center portion of the end diaphragms. The failures were in diagonal tension on a 45 degree (0.80 rad) surface in the end diaphragms, as shown in Fig. 3.7.

On the inside face, the diagonal tension cracks can be seen to extend from the end of the hole which was in contact with the hardened washer toward the mating surface, at 45 degrees (0.80 rad) toward the outer edge of the specimen. Once the crack left the inside face, it traveled

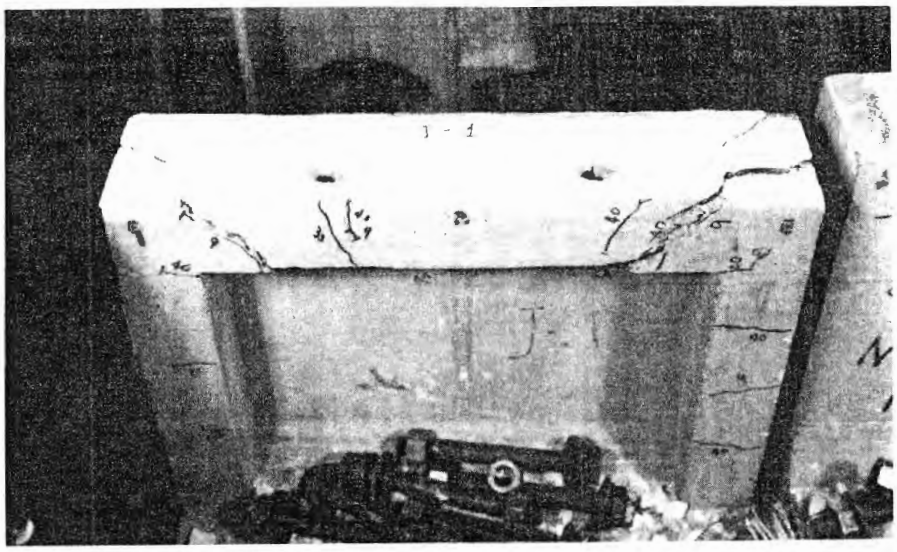

(a) Specimen J-1

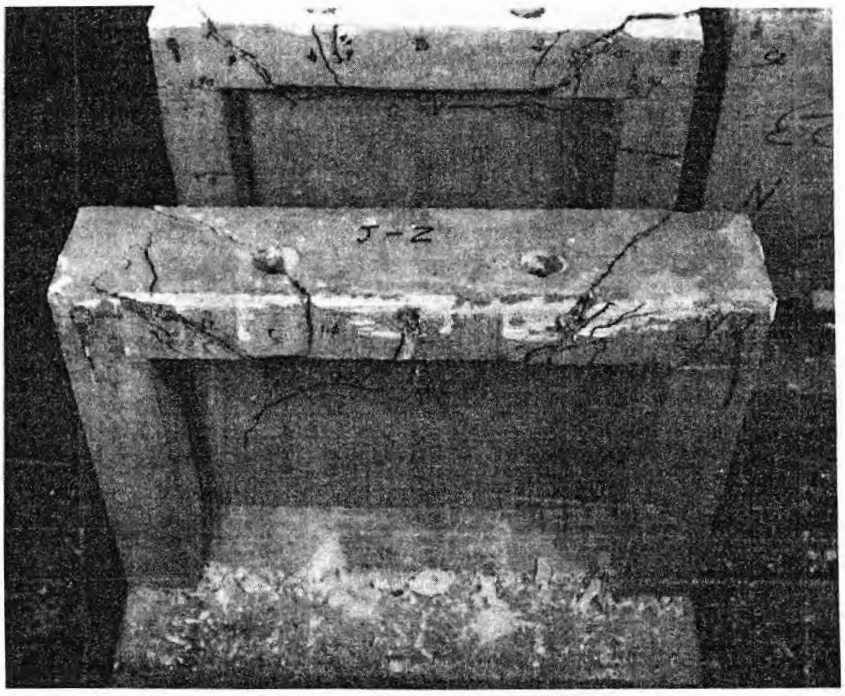

(b) Specimen J-2

FIGURE 3.7 SPECIMENS J-1 AND J-2 AFTER TEST

toward the side of the joint at approximately 45 degrees (0.80 rad), isolating the center portion of the diaphragm. The failure mode appears to be diagonal tension on these surfaces. The isolated portion of the end diaphragm remains attached to the shell acting as a short cantilever. The crack patterns are shown in Figs. 3.8 and 3.9. The maximum load may occur

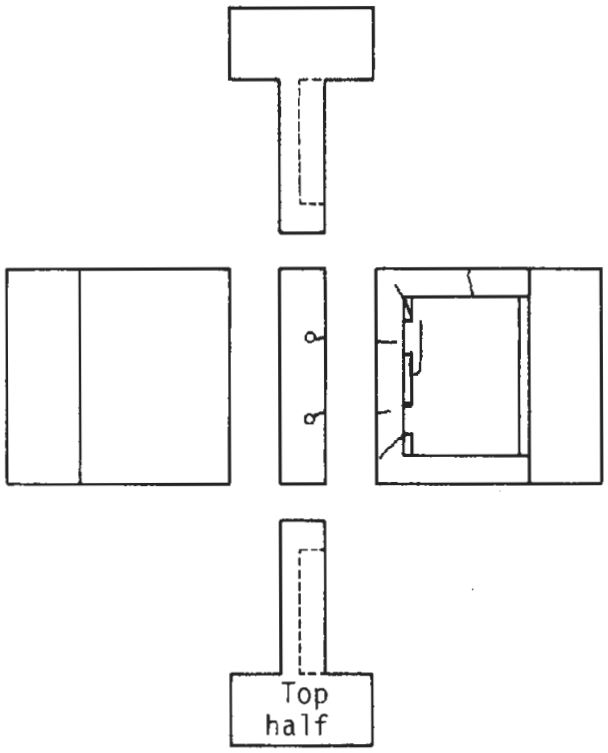

FIGURE 3.8 CRACKING OF SPECIMEN J-1 AFTER TEST

either when failure occurs on the diagonal tension surface described above or when failure occurs in the small cantilever beam which must resist all the moment once diagonal cracking occurs. From observation of the tests, the maximum load appears to occur when the diagonal tension cracks formed.

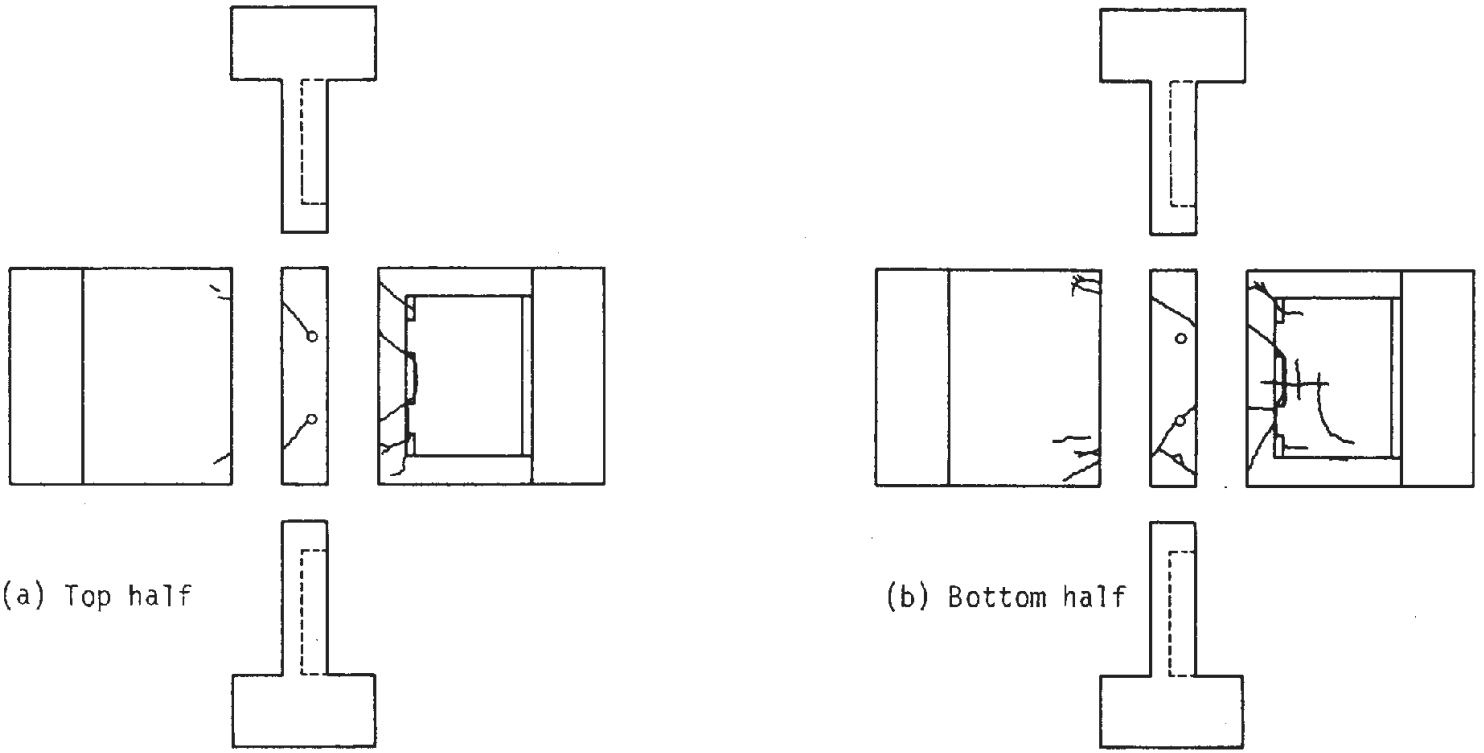

FIGURE 3.9 CRACKING OF SPECIMEN J-2 AFTER TEST

The bolts in both specimens were tightened to a torque on the nut of 100 lb-ft (136 N•m). During tightening of the nut, the bolt forces were measured. The relationship between torque and bolt load is shown in Fig. 3.10. Initial maximum bolt force in specimen J-1 was 8.1 kips (36.0 N) and in J-2 it was 7.8 kips (34.5 N). There was some delay in testing the specimens after initial bolt tensioning because of the time required to place a specimen in the testing machine and install other instrumentation. Creep and shrinkage of the concrete under load allowed the bolt loads to decrease. In specimen J-1 drift in the electronic equipment made the measurement of this change in load unreliable though in J-2 it appeared to be reasonable. The change in bolt force during the test was also measured. The entire loading history of the bolts is shown in Fig. 3.11 from initial tensioning through the test, though the loss of load due to creep after initial torque was applied is assumed zero for specimen J-1.

Initially, the bolt forces became slightly smaller during loading; then they increased with additional moment. When the maximum load was reached, and as the diagonal tension crack formed, the bolt load began to decline. Up to the maximum load the bolt is applying load to the end diaphragm which is being resisted both by diagonal tension and cantilever action. When the diagonal tension crack formed the bolt load fell off to approximately its initial value. The moment resistance of the joint remains relatively high, however.

Rotation of the joint is shown as a function of moment at the mating surface in Fig. 3.12. The rotation was measured over a distance of 6 in. (152 mm) on either side of the mating surface and, therefore,

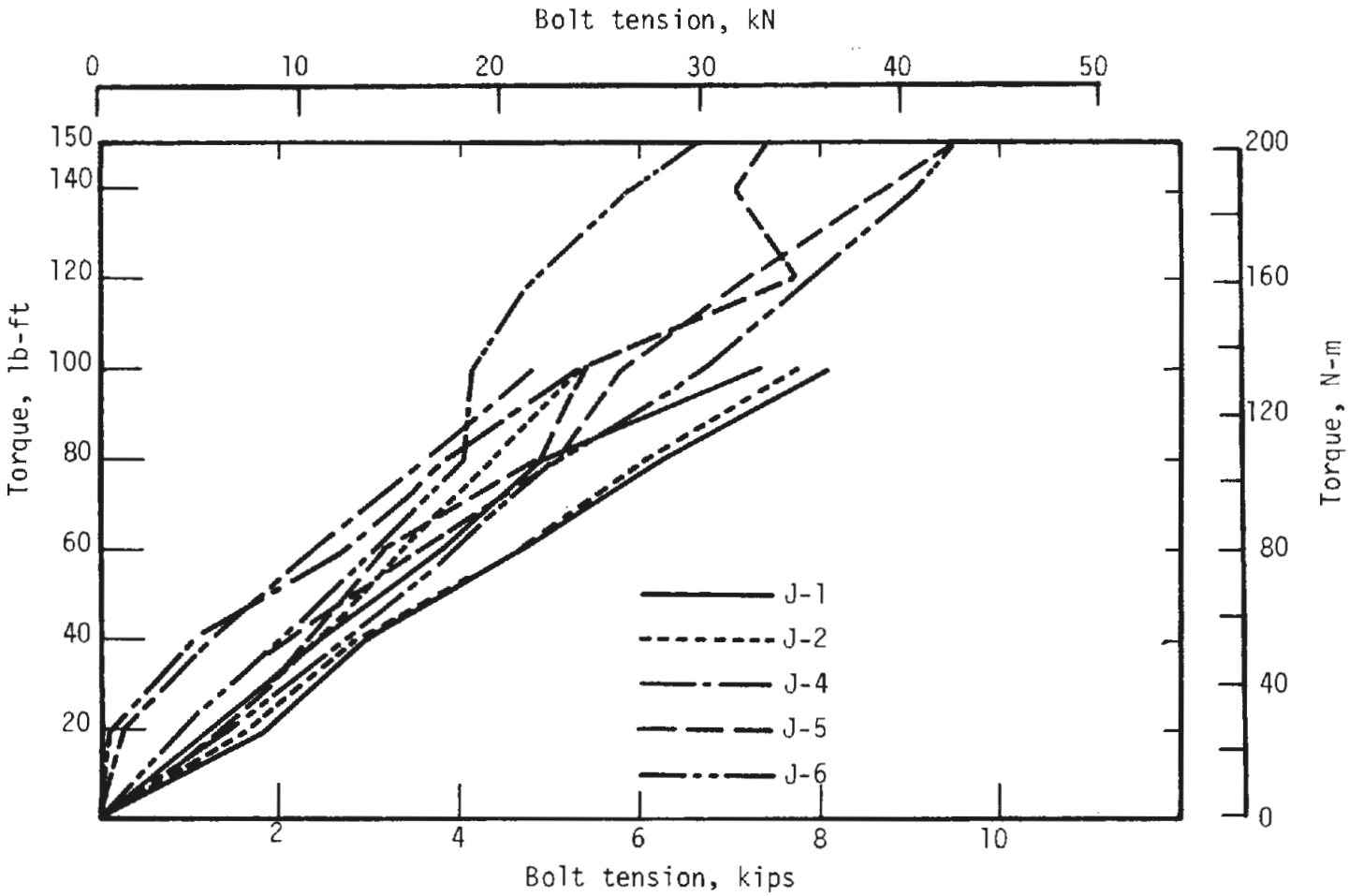

FIGURE 3.10 RELATION BETWEEN TORQUE AND TENSION FOR A BOLT IN THE JOINT

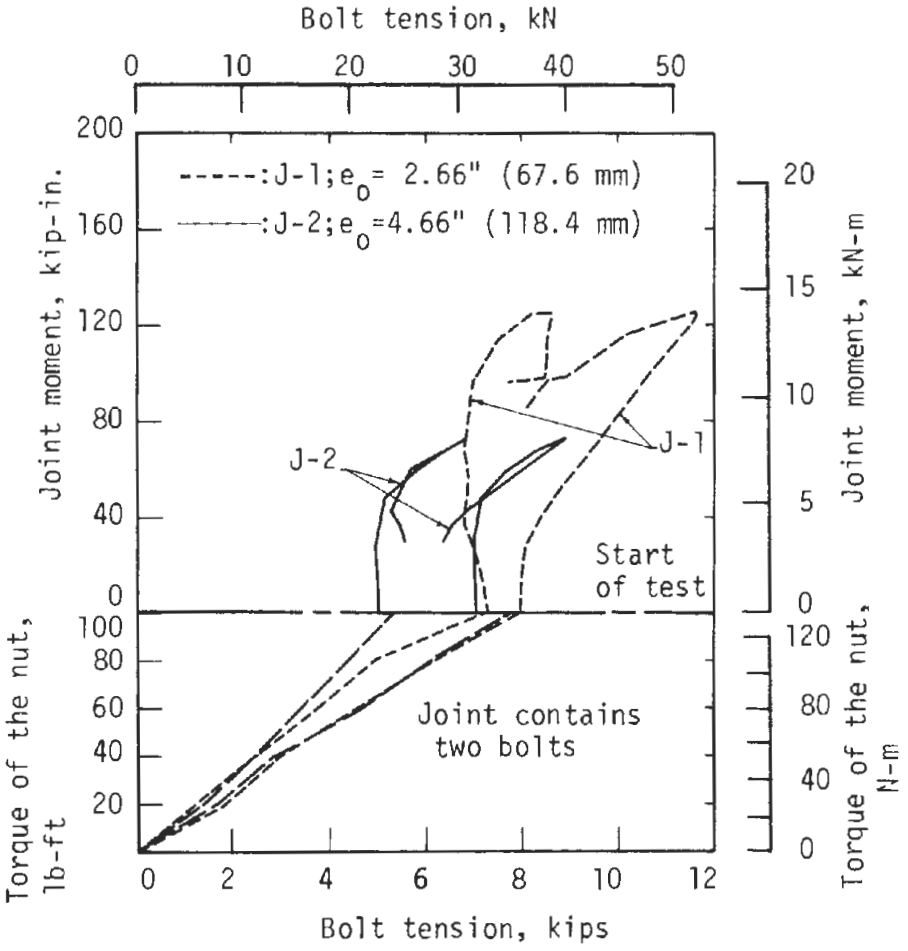

FIGURE 3.11 BOLT TENSION DURING INITIAL TORQUING AND DURING THE TEST

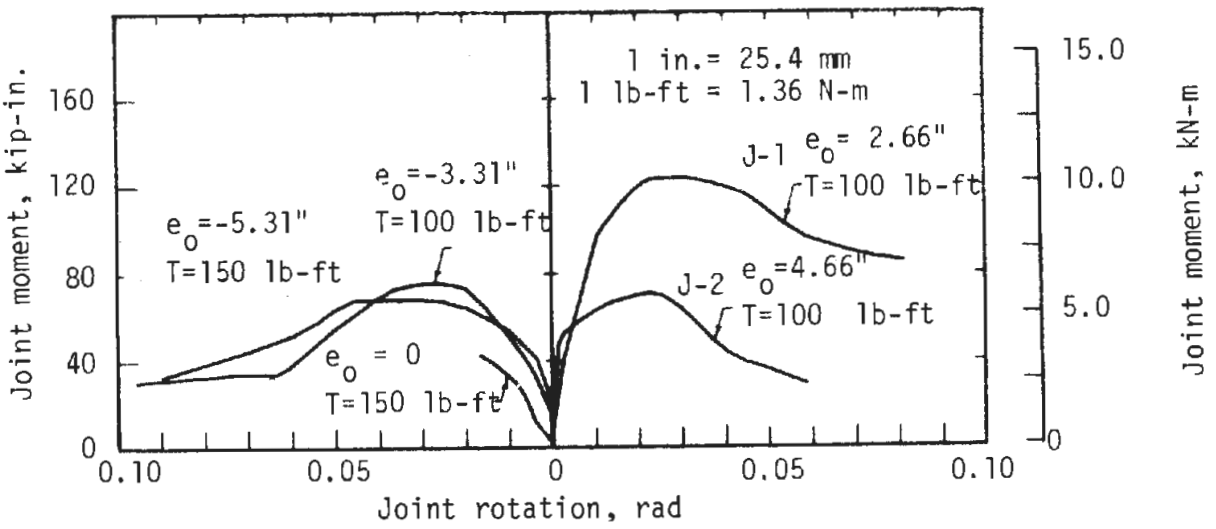

FIGURE 3.12 MOMENT-ROTATION RELATIONSHIP FOR THE JOINT TESTS

includes some bending of the segment, but most of the rotation occurred at the joint. The initial slope of the moment-rotation curve is greater for the larger eccentricity. The most significant observations from Fig. 3.12 are that the behavior, in terms of moment-rotation of the joint, was rather ductile and the specimen with smaller eccentricity had a considerably larger moment capacity. This behavior is typical of ordinary concrete members subjected to eccentric compressive forces such that the failure conditions are on the lower or tension failure region of an interaction diagram where additional axial load increases the moment capacity. The essential test specimen parameters and test results are summarized in Table 3.2.

3.3.2 NEGATIVE ECCENTRICITY

Specimens J-4 and J-5 were tested with negative initial

TABLE 3.2

SUMMARY OF SEGMENT JOINT TEST RESULTS

Specimen number	Initial eccentricity, in. (mm)	Initial bolt torque, lb-ft (kN-m)	Maximum load, kips (kN)	Moment at max. load, kip-in. (kN-m)	Bolt tension at max. load, kips (kN)		Deflection at max. load, in. (mm)	Joint opening at max. load, in. (mm)		
					bolt 1	bolt 2		edge	center	edge
J-1	+2.66 (67.6)	100 (136)	42.53 (189.18)	+127.04 (+14.354)	8.6 (38.3)	11.6 (51.6)	0.327 (8.31)	0.0714 (1.814)	0.0125 (0.318)	0.080 (2.03)
J-2	+4.66 (118.4)	100 (136)	14.77 (65.70)	+ 74.82 (+8.454)	6.8 (30.2)	8.9 (39.6)	0.406 (10.31)	0.0855 (2.172)	0.0084 (0.213)	0.0907 (2.304)
J-4	-3.31 (-84.1)	100 (136)	21.40 (95.19)	-77.28 (-8.732)	9.3 (41.4)	10.3 (45.8)	0.301 (7.65)	0.0886 (2.250)	0.084 (2.134)	0.0771 (1.958)
J-5	-5.31 (-134.9)	150 (203)	12.30 (54.71)	-71.24) (-8.049)	8.7 (38.7)	11.0 (48.9)	0.482 (12.24)	0.0860 (2.184)	0.0860 (2.184)	0.0865 (2.197)
J-6	.0	150 (203)	210.20 (935.02)	-42.04 (-4.750)	5.7 (25.4)	9.6 (42.7)	0.200 (5.08)	0	0	0

eccentricities which placed the flange of the segment in tension. The eccentricities were 3.31 and 5.31 in. (84.1 and 134.9 mm), respectively, measured from the calculated plastic centroid of the segment. The bolts were tightened to an initial torque of 100 lb-ft (136 N•m) for J-4 and 150 lb-ft (203 N•m) for J-5. The torque was increased for J-5 because the joint opening in J-4 appeared to be excessive since the bolts could be seen through the opening of the mating surface at maximum load. The joint opening on the outside of the segment is shown in Fig. 3.13 as a function of moment at the joint. The greater initial bolt tension for J-5 does not appear to have affected the opening of the joint up to a moment of about 55 kip-in. (6.2 kN•m).

Photographs of the specimens J-4 and J-5 after testing are shown in Fig. 3.14 and drawings of the major cracks and failure zones are shown in Figs. 3.15 and 3.16. These figures show a mode of failure that is different from specimens J-1 and J-2. In J-4 there was definite crushing of the webs inside the segment as shown in Fig. 3.14(a). Between the webs, a crack occurred in a plane parallel to the bolt holes and nearly tangent to the outside of the holes. This crack can be seen on the mating surface in Fig. 3.14(a).

Specimen J-5 did not have crushing of the webs as in J-4 though there was some spalling of the inside edge of the end diaphragm, as shown in Fig. 3.16(b) which was more pronounced near the webs. In addition, there was crushing of the concrete around the heads of the bolts, indicating that the bolt force had become greater than the bearing strength of the concrete under their heads. Also, under one bolt a large chunk of concrete spalled off the inside edge of the end diaphragm. The bolts were very

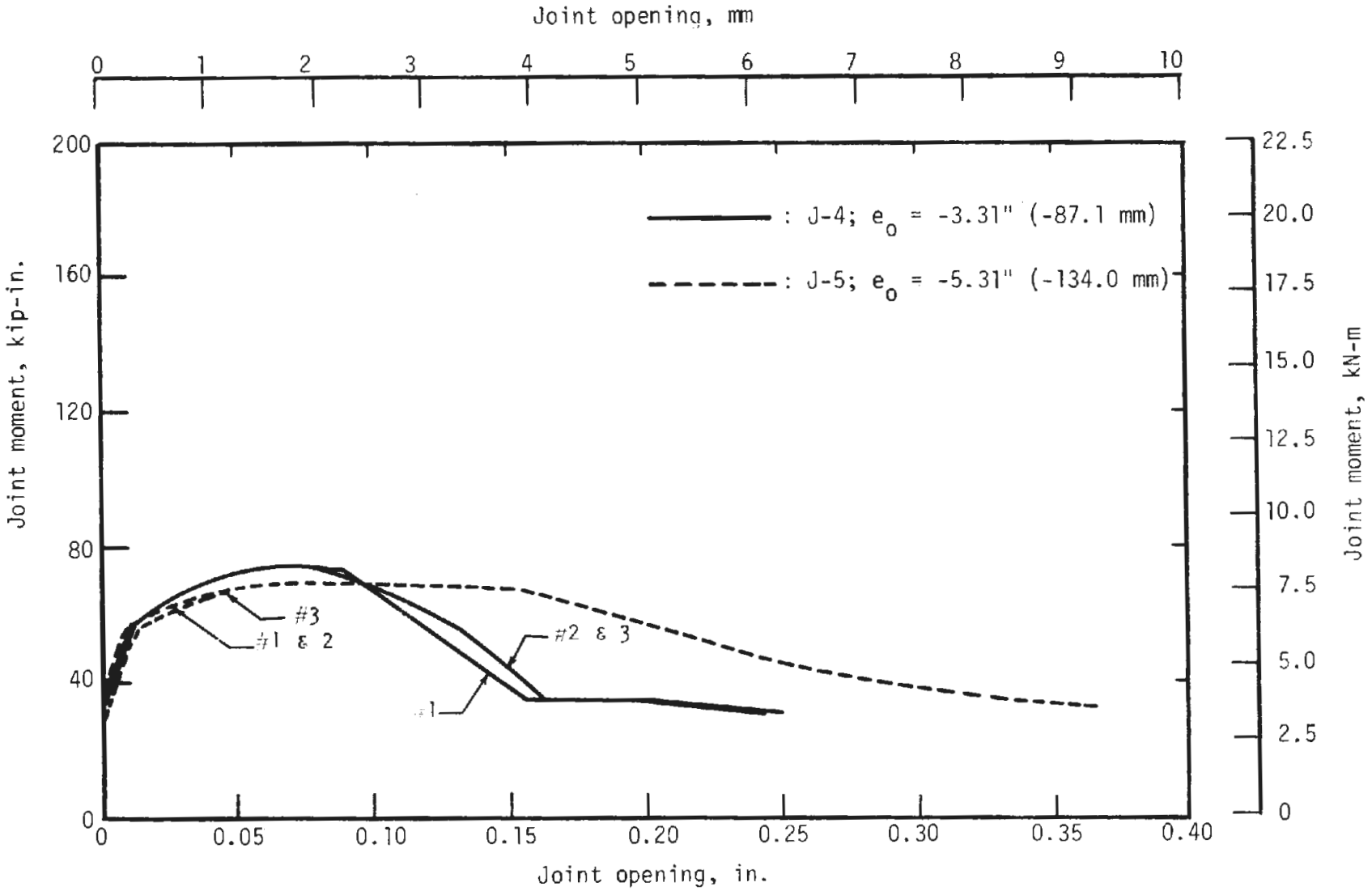

FIGURE 3.13 JOINT OPENING-MOMENT FOR TESTS J-4 AND J-5

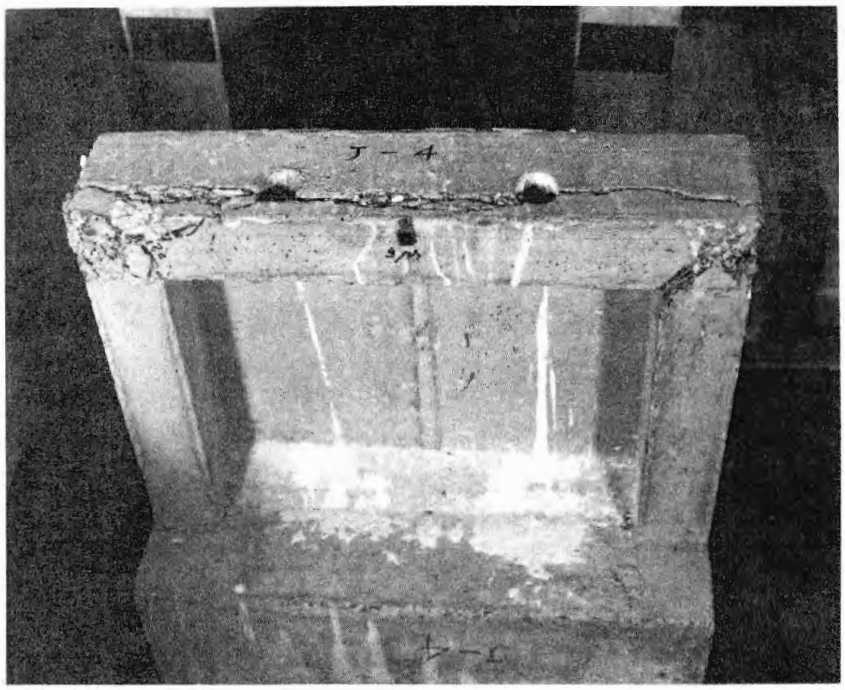

(a) Specimen J-4

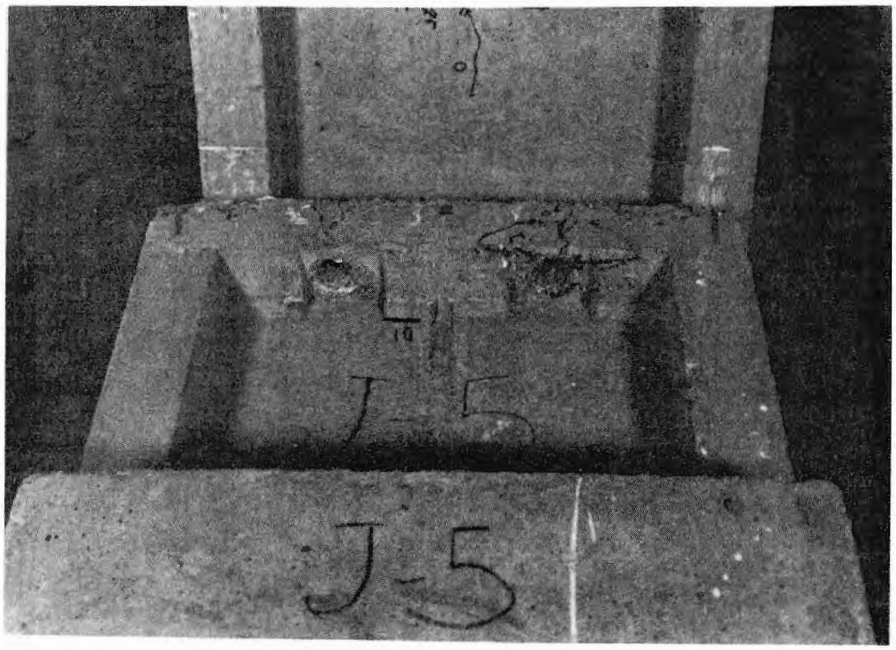

(b) Specimen J-5

FIGURE 3.14 SPECIMENS J-4 and J-5 AFTER TEST

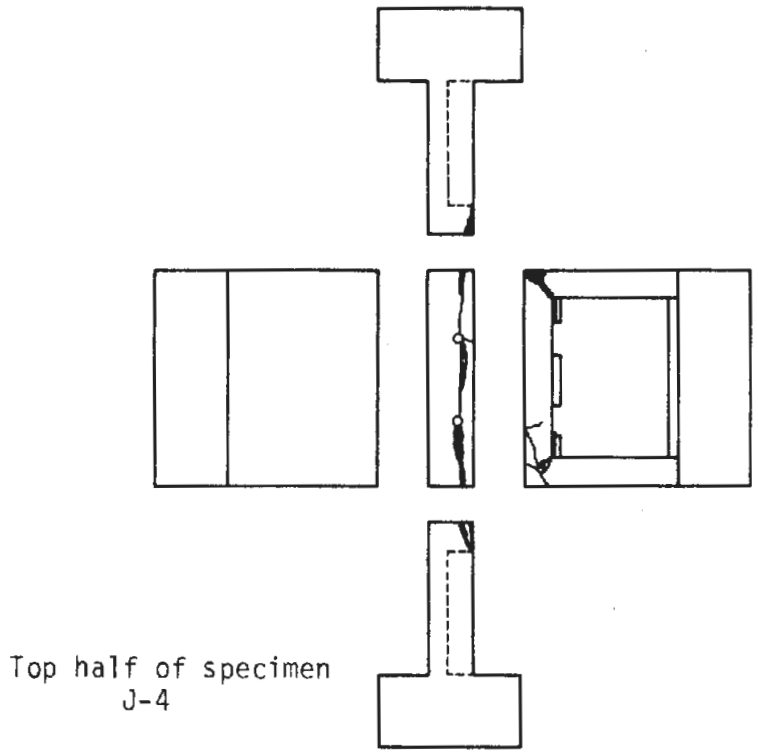

FIGURE 3.15 CRACKING OF SPECIMEN J-4 AFTER TEST

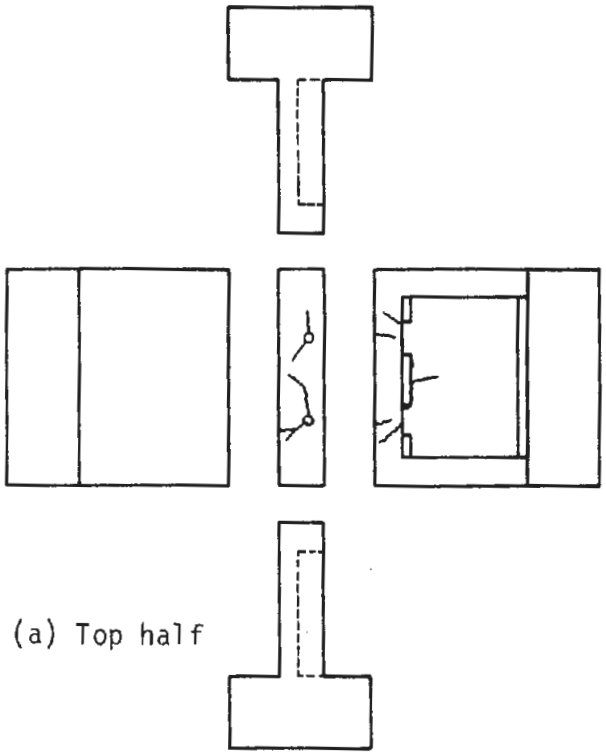

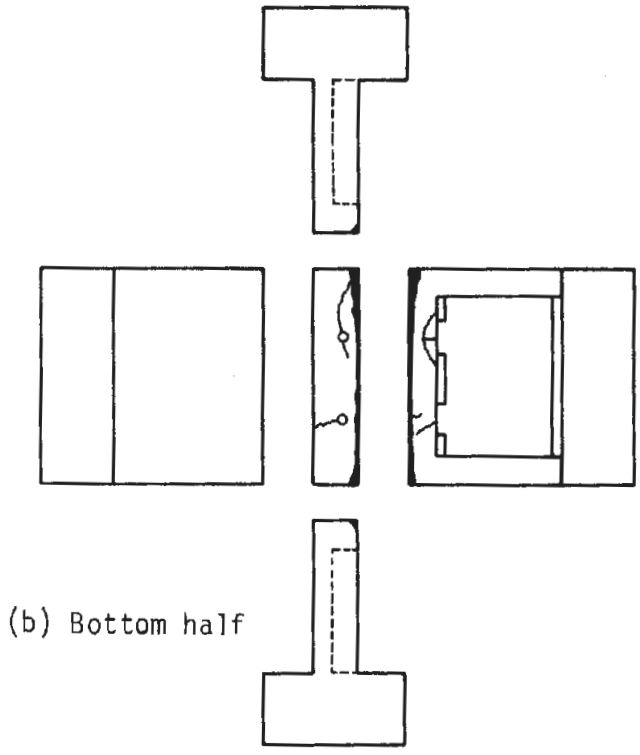

FIGURE 3.16 CRACKING OF SPECIMEN J-5 AFTER TEST

loose after the test. Further investigation of specimen J-4 showed that the bolts were also loose after the test, but the crushing under the bolt heads was not as extensive.

The complete history of bolt loadings is shown in Fig. 3.17, except that the creep and shrinkage loss of load of J-4 is not shown as this measurement was not considered reliable. The maximum load in the bolts of J-5 are shown to be only slightly higher than for J-4, though the difference might be considerably higher if the loss of load were known for J-4. The change in bolt loads during the test remained essentially constant for low moment, and then began to increase after 20 to 30 kip-in. (2.3 to 3.4 kN•m) of moment was applied, reaching a maximum load of about 11 kips (49 kN) in both tests.

The moment-rotation relationships for the joints are shown in Fig. 3.12 where it is seen that the curves are quite close for the two specimens. The eccentricity, therefore, does not affect the maximum moment very much, but the maximum load is quite different for the two cases (Table 3.2). The difference in initial bolt tension should be kept in mind but clouds the comparison somewhat. The failure appears to be in the region of a very steep part of the failure envelope where the load is rising rapidly, but the moment is changing very little. The behavior is very ductile, and large deformations are possible before there is appreciable loss of moment.

3.3.3 ZERO ECCENTRICITY

Load was applied to specimen J-6 at the calculated plastic centroid of the segment section. Though considerable rotation occurred at

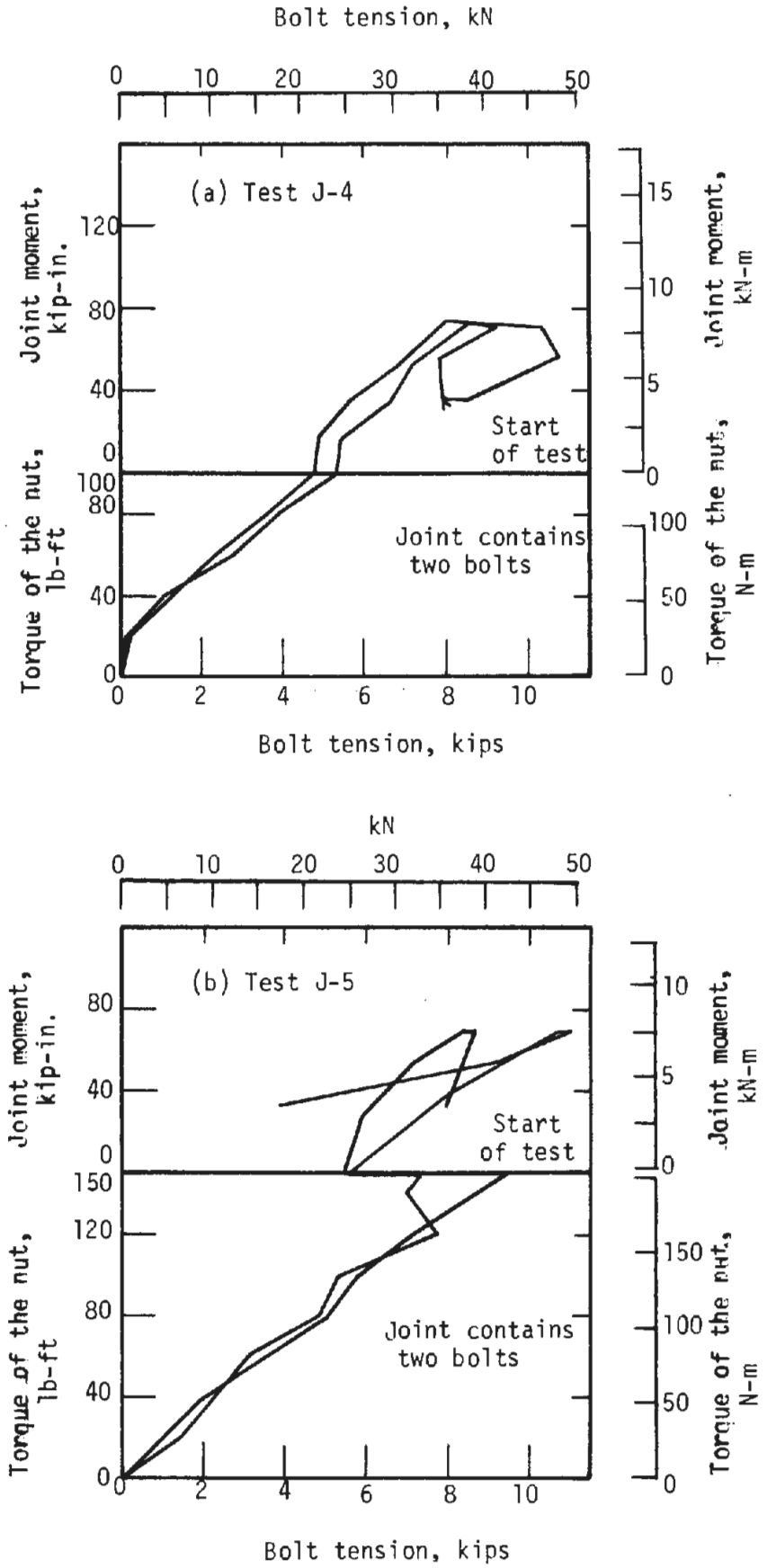

FIGURE 3.17 BOLT TENSION DURING INITIAL TORQUING AND DURING THE TEST

the joint as shown in Fig. 3.12, the failure mode indicated a reasonably uniform strain as crushing occurred both on the inside and outside of the specimen. Photographs of the failed specimen are shown in Fig. 3.18 and drawings of the major failure regions are shown in Fig. 3.19. The joint opening was negligible and indicates the fairly uniform strain distribution in the specimen although the load must have been applied slightly inside of the real plastic centroid, as shown by the joint rotation in Fig. 3.12. The bolt forces shown in Fig. 3.20 indicate that at the start of loading there was a small reduction in the initial force resulting from 150 lb-ft (203 N•m) of torque on the nut. As lateral deformation continued, the bolt tension was restored essentially to its original value where it remained. The maximum load on the specimen was 210 kips (935 kN) or at least 5 times larger than any of the other maximum loads.

3.4 DISCUSSION OF RESULTS

The tests of concrete segment joints were designed to determine the strength of the joint without specific joint reinforcement other than the randomly oriented steel fibers and the main circumferential segment reinforcement that continued into the joint. With this information it is possible to determine what additional reinforcement in the joint is required to provide the strength desired. Other objectives were to determine the modes of failure for joints of this type and to develop a technique for computing their strength.

When a positive moment is applied such that the segment shell is in compression, failure occurs in diagonal tension at the end diaphram.

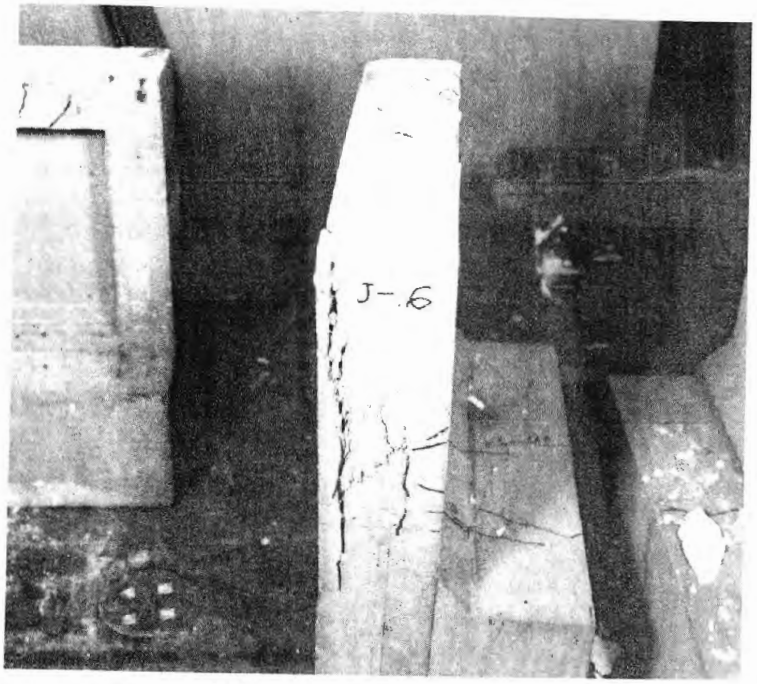

(a) Specimen J-6

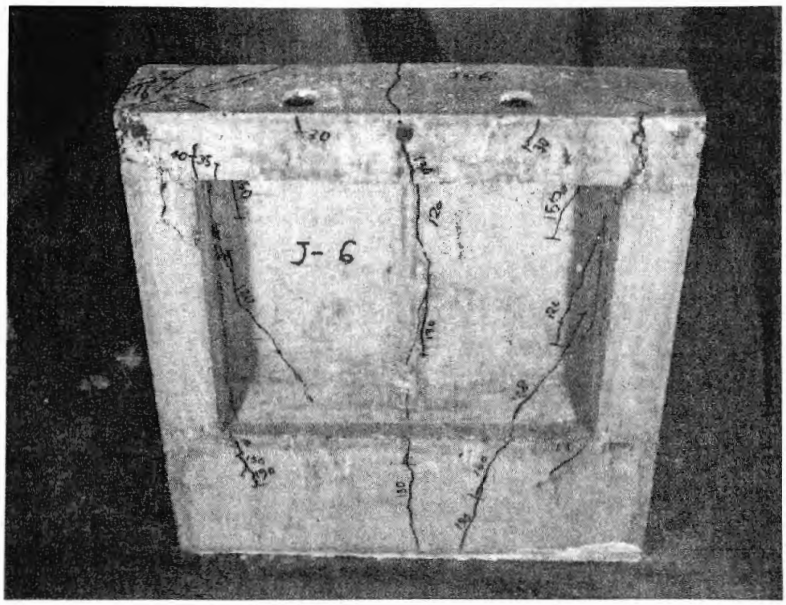

(b) Specimen J-6

FIGURE 3.18 SPECIMEN J-6 AFTER TEST

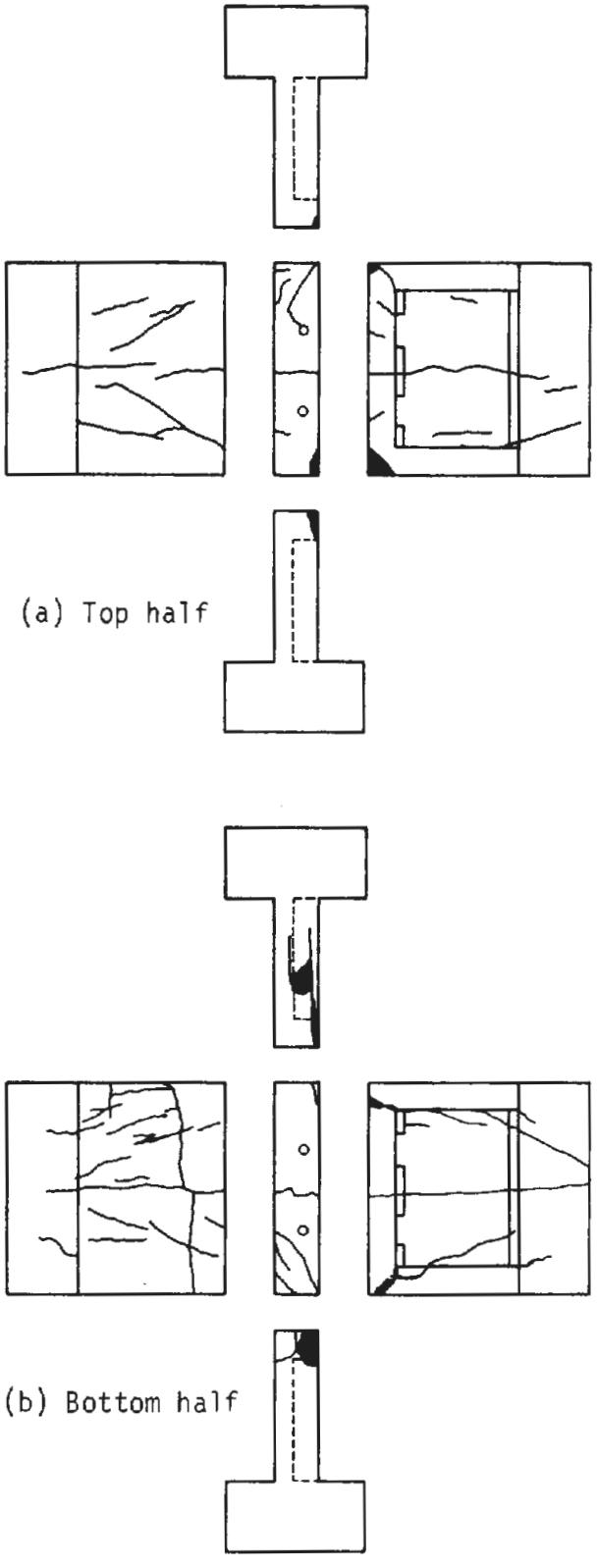

FIGURE 3.19 CRACKING OF SPECIMEN J-6 AFTER TEST

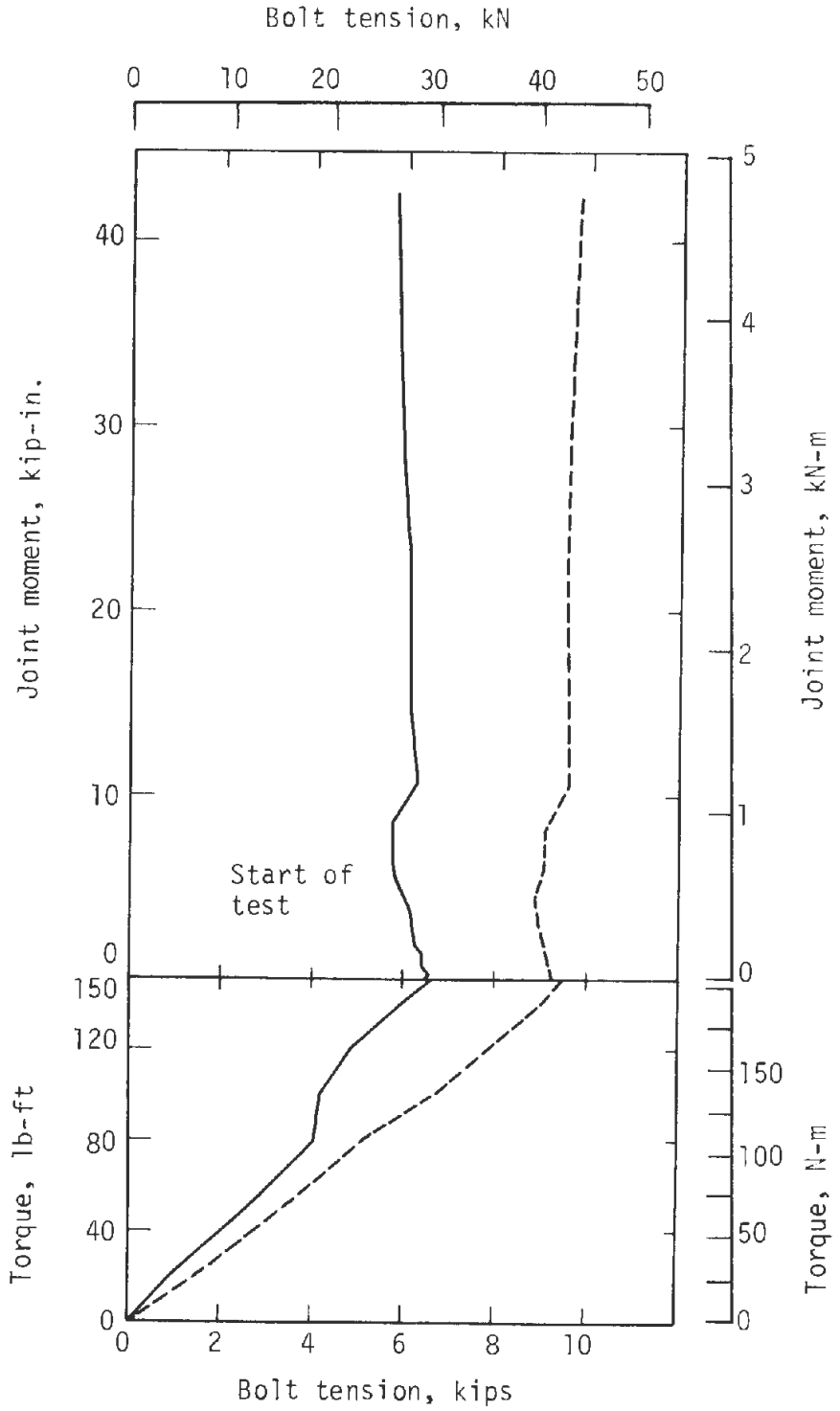

FIGURE 3.20 BOLT LOAD-MOMENT FOR TEST J-6

The part of the end diaphram containing the bolts separates from the remainder of the joint as shown in Fig. 3.7. This is shown further by the curves in Fig. 3.6 which indicate that the joint opened very little between the bolts and a relatively large amount at the ends. Maximum moment occurred just before the diagonal tension failure, and it is significant that considerable deformation can occur before this failure. When the maximum moment was reached the joint ends were opened on the order of 0.075 in. (1.90 mm), and a joint rotation of 0.02 to 0.25 radians had occurred. Even after maximum moment, the strength fell off relatively slowly so that when the peak rotation was doubled the moment was still 50 percent or more of the maximum.

The moment resisted by the forces on the failure surface described above can be calculated in an approximate manner for maximum load. The diagonal tension crack isolates a small cantilever on which the bolt forces act, so the cantilever as well as the diagonal tension force resist the bolt forces. If the resistance of the cantilever and diagonal tension force could be estimated so that the bolt force is known, then the joint capacity could be computed. With the measurement of maximum load and bolt force, it is possible to reverse the calculation to obtain a failure criterion which can be used to determine the failure loads at eccentricities other than those used in the tests.

Consider Test J-1 in which the following quantities were measured at maximum load.

P = applied force = 42.5 kips (189.0 kN)

2Q = bolt forces = 8.65 kips + 11.65 kips = 20.3 kips (90.5 kN)

e = initial eccentricity = +2.66 in. (67.6 mm)

S = deflection = 0.33 in. (8.4 mm)

f'_c = concrete compressive strength = 8,480 psi (58.45 MPa)

f_{ct} = splitting tensile strength = 795 psi (5.48 MPa)

f_r = modulus of rupture = 960 psi (6.62 MPa)

From the summation of vertical forces in Fig. 3.21(a), where the joint has been separated and the forces shown, the following expression is determined for the compression force C:

$$C = P + 2Q = 42.5 \text{ kips} + 19.3 \text{ kips} = 61.8 \text{ kips}$$

$$= 189 \text{ kN} + 85.9 \text{ kN} = 274.9 \text{ kN}$$

The forces Q are reduced by 0.5 kips (2.0 kN) each for loss due to creep and shrinkage which is estimated from J-2 giving 2Q = 19.3 kips (85.9 kN). This compression force does not correspond to ultimate conditions from crushing of the concrete as there was no sign of crushing. Thus, the location of C cannot be found from the ultimate stress block for the concrete. The location of the force can be found approximately by taking moments about the bolt force in the free-body diagram shown in Fig. 3.21(a). Then;

$$C = 61.8 \text{ kips} = \frac{1}{2} f_c \text{ ksi (24 in.)(1.35 in.)} \qquad f_c = 3.81 \text{ ksi}$$

$$C = 275.0 \text{ kN} = \frac{1}{2} f_c \text{ GPa (609.6 mm)(34.3 mm)} \qquad f_c = 26.25 \text{ MPa}$$

This stress is less than 1/2 f'_c so the assumption of linear compressive

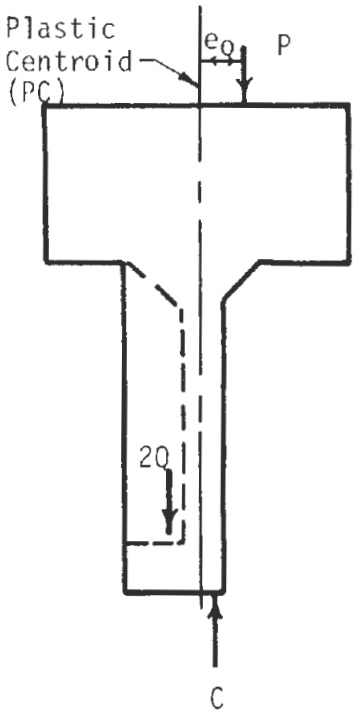

(a) Equilibrium of the specimen

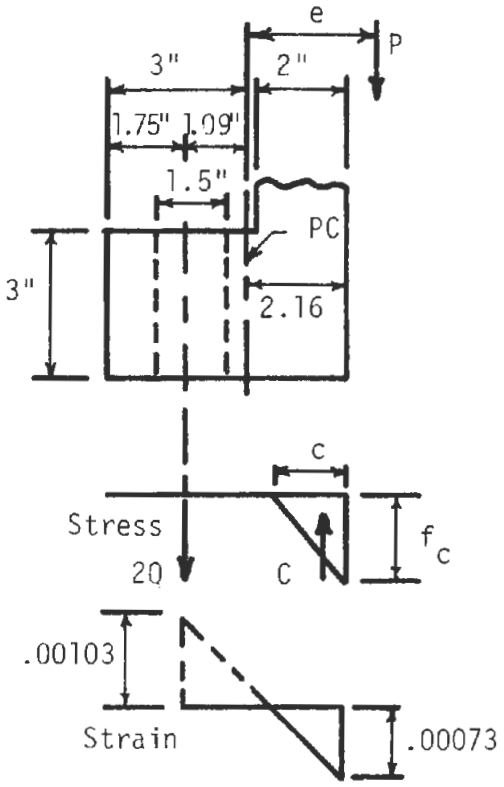

(b) Tension failure criterion

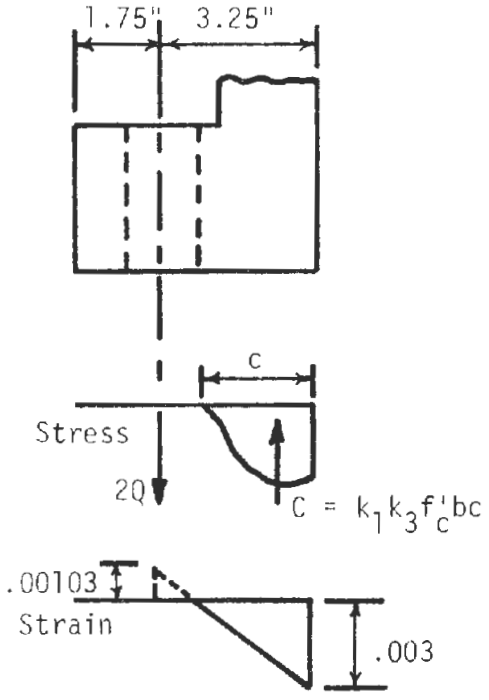

(c) Compression failure criterion

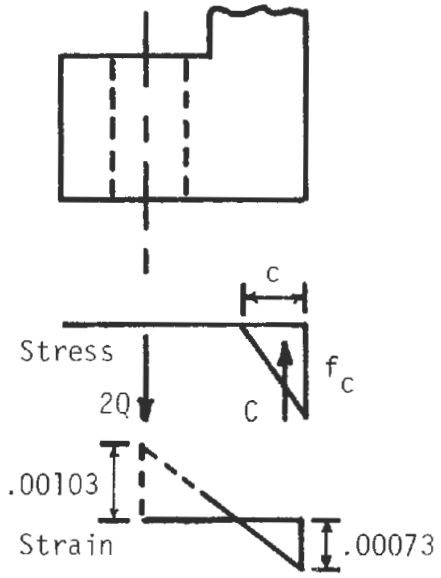

(d) Pure moment

FIGURE 3.21 ASSUMPTIONS MADE IN CALCULATIONS FOR SPECIMEN J-1

stress is a reasonable one. If Young's modulus is computed from the ACI formula, a value of 5,200 ksi (36.0 GPa) is obtained. The concrete compressive strain is 0.00073 and the corresponding pseudo strain in tension is 0.00103 computed on the basis of linear strain on the section. This is the equivalent tensile strain corresponding to failure in diagonal tension.

If the eccentricity is reduced, a value will be reached when the moment is small and a diagonal tension failure in the concrete will no longer occur. At this eccentricity the compression force, C, becomes so large that crushing occurs in the extreme concrete compression fibers. For this type of failure, the normal compression failure criteria can be applied. At some eccentricity, tension and compression failure will occur simultaneously, which is called balanced conditions. The corresponding load and moment can be found by applying both failure criteria (tension and compression). From Fig. 3.21(c) it is found that c = 2.42 in. (61.5 mm) from the geometry of strain. Then,

$$C = 0.65(0.85)(8.48 \text{ ksi})(24 \text{ in.})(2.42 \text{ in.}) = 272 \text{ kips}$$

$$= 0.65(0.85)(58.47 \text{ MPa})(609.6 \text{ mm})(61.47 \text{ mm}) = 1210 \text{ kN}$$

$$2Q = 19.3 \text{ kips}$$

$$= 86.0 \text{ kN}$$

$$P_b = C - 2Q = 272 - 19.3 = 253 \text{ kips}$$

$$= 1210 - 85 = 1125 \text{ kN}$$

$$M_b = 272 \text{ kips } (1.37 \text{ in.}) + 19.3 \text{ kips } (1.09 \text{ in.}) = 394 \text{ kip-in.}$$

$$= 1210 \text{ kN } (34.8 \text{ mm}) + 85 \text{ kN } (27.7 \text{ mm}) = 44.5 \text{ kN•m}$$

$$e_b = M_b/P_b = 1.56 \text{ in.}$$

$$39.6 \text{ mm}$$

where the subscript b corresponds to balanced conditions.

The capacity of the joint subject to pure moment can also be obtained. In this case the compression and tension forces must balance. The forces are shown in Fig. 3.21(d).

$$2Q = C \quad 19.3 \text{ kips} = \frac{1}{2} f_c \text{ ksi } (c \text{ in.})(24 \text{ in.}) = 12 f_c (c)$$

$$85.85 \text{ kN} = \frac{\frac{1}{2} f_c \text{ MPa } (c \text{ mm})(609.6 \text{ mm})}{1{,}000} = 0.3048 f_c (c)$$

where c is the distance from the neutral axis to the outside face of the segment (Fig. 3.21(d)).

From the geometry of the strain distribution

$$c = \frac{\varepsilon_c}{0.00103 + \varepsilon_c} \quad 3.25 \text{ in.}$$

$$c = \frac{\varepsilon_c}{0.00103 + \varepsilon_c} \quad 82.6 \text{ mm}$$

From the stress-strain properties of the concrete

$$f_c, \text{ ksi} = E_c \varepsilon_c = 5200 \text{ ksi } (\varepsilon_c)$$

$$f_c, \text{ MPa} = E_c \varepsilon_c = 35.85 \text{ GPa } (\varepsilon_c) \times 10^3 \frac{\text{MPa}}{\text{GPa}}$$

Solution of these equations gives c = 1.68 in. (42.7 mm) and results in P = 0, M_o = 58.3 kip-in. (6.59 kN•m).

The maximum axial force of the joint might be considered the force which causes crushing of the concrete on the mating surface where there is no steel reinforcement since the steel does not extend through the joint. The question, then, is what concrete area should be used. By realizing that the force can only be transmitted to the joint through the webs and flanges of the segment, and that very little force is transmitted by the end diaphram between the webs, it is conservative to calculate the axial strength, P_o, based on the segment cross section rather than the joint cross section. For specimen J-1:

$$P_o = 0.85 f'_c A_c = 0.85 (8.48 \text{ ksi})[24 \times 5 - 18 \times 3] \text{ in.}^2 = 476 \text{ kips}$$

$$= 0.85 (58.45 \text{ MPa})[610 \times 127 - 457 \times 76] \text{ mm}^2 = 2115 \text{ kN}$$

With this information, an approximate failure envelope for the joint can be constructed. This analysis was also carried out for specimen J-2. In Fig. 3.22 the failure envelope for the joint is shown obtained by averaging these calculations for J-1 and J-2. The failure envelope is also shown for the segment and it is noted that the joint fails at a lower

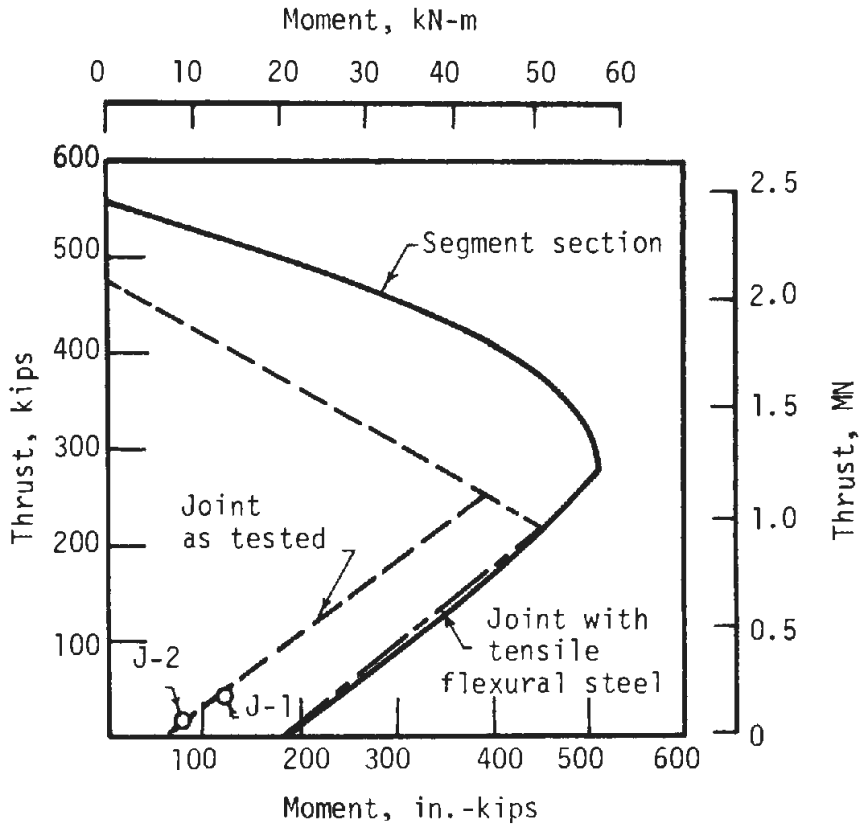

FIGURE 3.22 MOMENT-THRUST FAILURE ENVELOPE FOR THE SEGMENT AND JOINT SECTIONS, WITH POSITIVE MOMENT

moment-thrust combination than the segment. The additional steel required to make the joint as strong as the segment will be discussed later.

This type of analysis can be performed only if the bolt force can be estimated. In the above discussion it was measured, but it was found from the tests that it was limited by the diagonal tension in the end diaphram. Figure 3.23(a) shows a view from the inside of the segment of the end diaphram with the forces on the diagonal tension crack. A

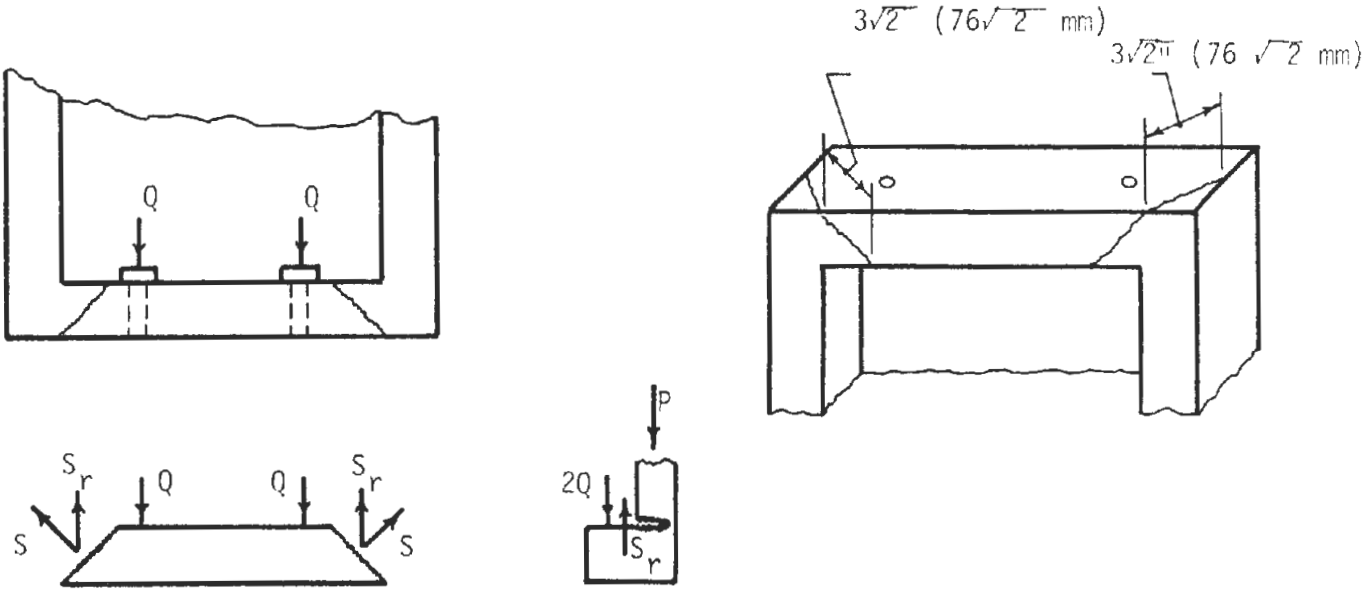

(a) Failure mechanism for positive moment

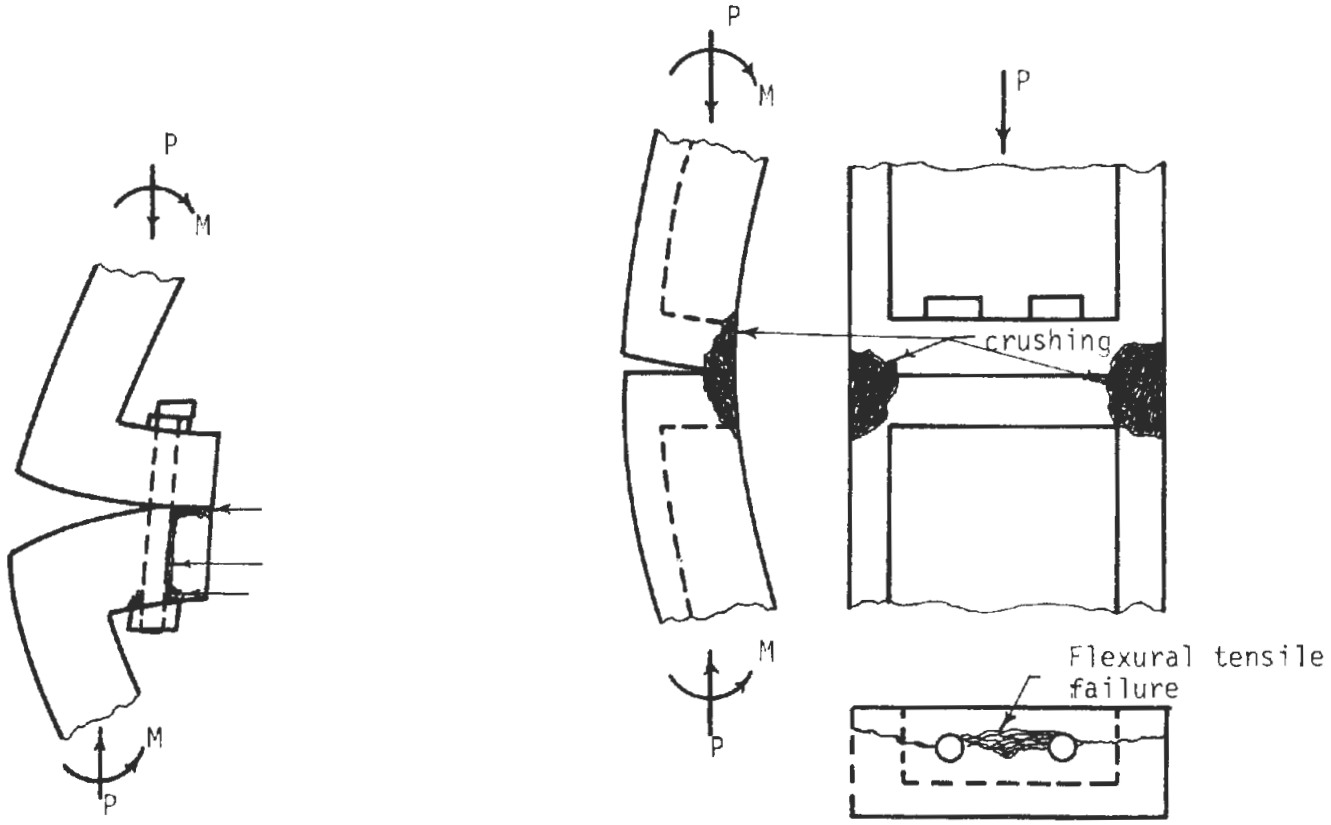

(b) Failure mechanism for negative moment

FIGURE 3.23 JOINT FAILURE MECHANISMS

three-dimensional view of the crack is also shown. Some of the bolt force is transferred through shear to the support of the small cantilever, but the greater part is transferred by diagonal tension directly to the side webs. It is conservative to make this assumption, so the stress is calculated on the diagonal tension surface for J-1 from the known bolt forces.

$$2Q = 2S_v = 2(f_t \cos 45°)\, A_t = 19.3 \text{ kips } (85.85 \text{ kN})$$

but $$A_t = (3 \text{ in.})\sqrt{2} \cdot (3 \text{ in.})\sqrt{2} = 18 \text{ in.}^2$$

$$= (76.2 \text{ mm})\sqrt{2} \cdot (76.2 \text{ mm})\sqrt{2} = 11.613 \times 10^3 \text{ mm}^2$$

therefore,

$$f_t = 0.758 \text{ ksi } (5.225 \text{ MPa})$$

where

S_v = vertical component of normal force on the diagonal-tension failure surface

A_t = area of diagonal-tension failure surface on one side of the separated chunk of concrete

f_t = tension stress perpendicular to the failure surface.

For specimen J-1 the splitting tensile strength was 0.795 ksi (5.48 MPa) and the modulus of rupture was 0.960 ksi (6.62 MPa). It appears that a reasonable estimate of the bolt force can be found from applying the splitting tensile strength to the diagonal tension failure surface. The

same comparison for specimen J-2 gives f_t = 620 psi (4.28 MPa) and f_{ct} = 820 psi (5.65 MPa) which gives a tension stress of 75 percent of the split cylinder strength. It is normal in conventional concrete to expect that f_t = (0.5 to 0.7) f_{sp} so the latter comparison probably represents a lower limit on the bolt force that can be used for fiber-reinforced concrete. Considerable scatter is expected in test results where failure depends on the tensile strength of concrete. Also, these suggested computational procedures must be considered tentative in that they are based on only two tests.

The Grade 50 (344.5 MPa minimum yield stress) reinforcing steel, normal to the diagonal tension failure surface, required to make the joint as strong as the segment section in the tension region of the failure envelope, was computed to be about 0.5 $in.^2$ (323 mm^2) by increasing the force across the diagonal crack by the nominal yield forces in the bars. With this steel added, the failure envelope is shown in Fig. 3.22 also.

When bending occurred with negative eccentricity, the mode of failure of the two specimens was different. In specimen J-4 the compression area was reduced drastically from that in J-1 and J-2, as it is restricted to the web area, because very little thrust can be transferred through the end diaphram between the webs. Thus, crushing of the concrete occurred only where the end diaphram joins the webs or side diaphrams, so the stress distribution along the inside edge of the mating surface is very nonuniform and can be separated as shown in Fig. 3.24(a) into two components, C_1 and C_2, where C_1 = 2Q. The moment between the flanges for

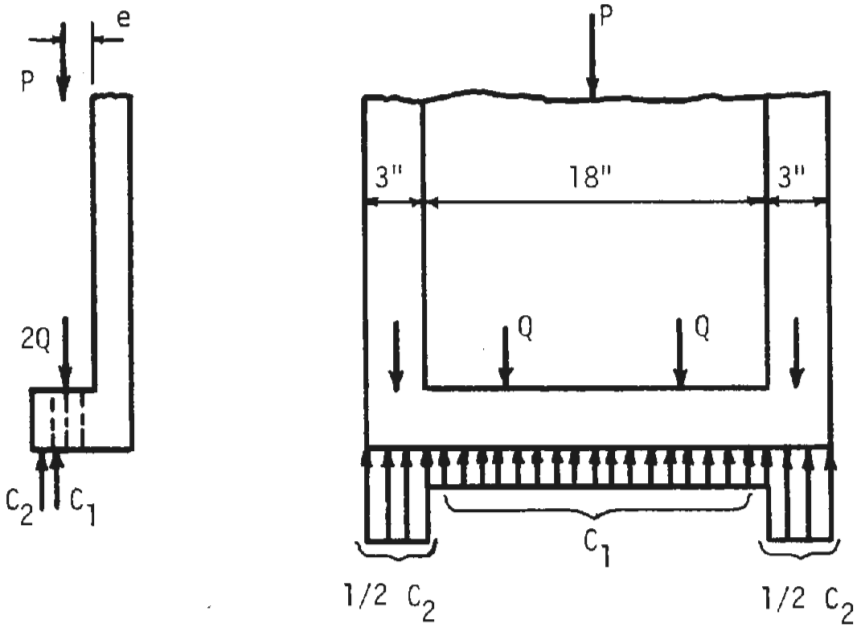

(a) Equilibrium of forces on one-half the specimen

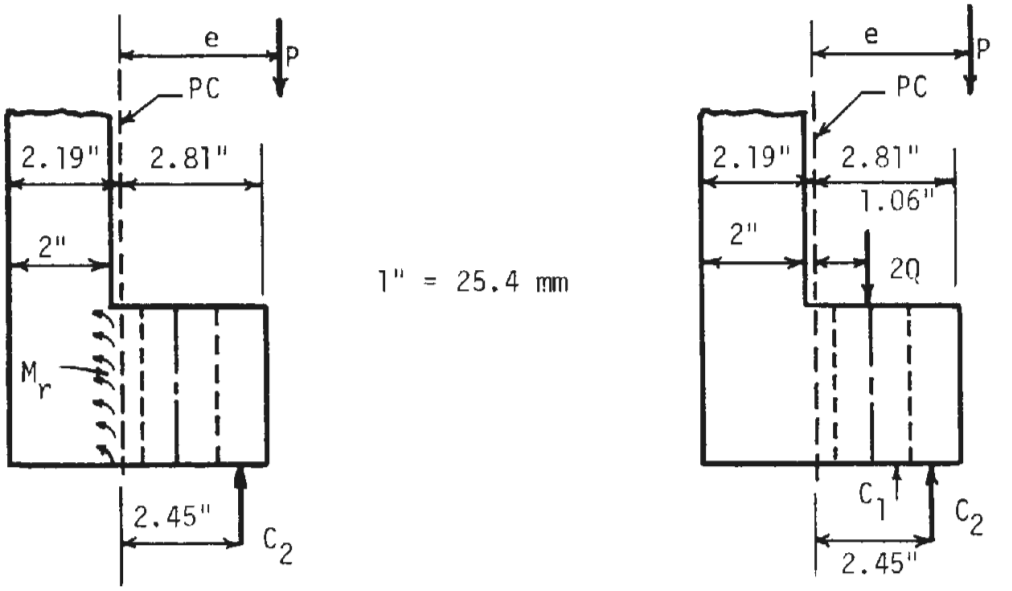

(b) Forces at the joint with 2Q and C_1 replaced by M_r

(c) Forces acting at the joint

FIGURE 3.24 JOINT FAILURE MECHANISM FOR SPECIMEN J-4 WITH NEGATIVE MOMENT APPLIED

specimen J-4 can be computed as the ultimate flexural strength of the cantilever beam between the flanges.

$$M_r = \frac{f_r I}{c} = \frac{0.81 \text{ ksi } (33.8 \text{ in.}^4)}{1.5 \text{ in.}} = 18.2 \text{ kip-in.}$$

$$= \frac{5.58 \text{ MPa } (1406 \times 10^4 \text{ mm}^4)}{38.1 \text{ mm}} = 2.06 \text{ kN·m}$$

where

$c = \frac{1}{2}$ (end diaphram thickness) $= \frac{1}{2}$ (3 in.) $= 1.5$ in.

$= 38.1$ mm

I = moment of inertia

$= \frac{1}{12}$ (15 in.)(3 in.)$^3 = 33.8$ in.^{4}

$= \frac{1}{12}$ (381 mm)(76.2 mm)$^3 = 1.405 \times 10^7$ mm^4

f_r = 810 psi (5.58 MPa)

M_r = moment at cracking of the concrete in the cantilever beam consisting of the segment end diaphram between the webs, with a length from the bolts to the inside edge of the segment

The width of the cantilever beam is taken as 15 in. (381 mm) because the bolt holes are removed at the failure section. If it is further assumed that the cantilever beam capacity is reached at the same time as crushing in the concrete, the maximum load can be calculated. The ultimate rectangular stress block is used for the concrete in the webs plus their extensions into the flange, and the bolt force at maximum load is used from the tests.

Then from Fig. 3.24(a) the force at the inside edge of each side web at crushing of the concrete is

$$\sum F_v = 0, \quad P = C_2 = k_1 k_3 f'_c tc = 0.75(0.85)(6.0 \text{ ksi})(2 \times 3 \text{ in.})c, \text{ in.}$$

$$\text{or} \quad P = C_2, \text{ kips} = 22.95c, \text{ in.}$$

$$= 0.75(0.85(41.37 \text{ MPa})(2)(76.2 \text{ mm})c, \text{ mm}$$

$$\text{or} \quad P = C_2, \text{ kN} = 4.009c, \text{ mm}$$

Forces C_1 and 2Q do not influence $\sum F_v$ because they are assumed equal, but result in a bending moment, M_r.

$$\text{Eccentricity} = e = e_o + \Delta = 3.31 \text{ in.} + 0.30 \text{ in.} = 3.61 \text{ in.}$$

$$= 84.1 \text{ mm} + 7.6 \text{ mm} = 91.7 \text{ mm}$$

$$\sum M_{PC} = 0 \quad P \text{ kips } (3.61 \text{ in.}) = C_2 \text{ kips } [2.81 - \tfrac{1}{2} k_1 c] \text{ in.} + M_r \text{ kip-in.}$$

$$P \text{ kN } (91.7 \text{ mm}) = C_2 \text{ kN } [71.4 - \tfrac{1}{2} k_1 c] \text{ mm} + M_r \text{ kN·mm}$$

where

M_r = 18.2 kip-in. (2.06 kN-m) and replaces the effect of C_1 and 2Q

Values of k_1 and k_3 are taken, from ultimate strength theory for ordinary concrete, to be 0.75 and 0.85 respectively. Combining these two equations gives c = 0.97 in. (24.6 mm) and P = 22.2 kips (98.8 kN). The resultant moment at the joint about the plastic centroid of the segment section is then, from Fig. 3.24(c),

$$M = C_2 \text{ kips } [2.81 - \tfrac{1}{2}(0.75)(0.97)] \text{ in.} + M_r \text{ kip-in.}$$

$$= 22.2 \text{ kips } (2.45 \text{ in.}) + 18.2 \text{ kip-in.} = 72.6 \text{ kip-in.}$$

$$M = C_2 \text{ kN } [71.4 - \tfrac{1}{2}(0.75)(24.6)] \text{ mm} + M_r \text{ kN-mm}$$

$$= 98.8 \text{ kN } (62.2 \text{ mm}) + 2.06 \times 10^3 \text{ kN-mm} = 8.20 \text{ kN-m}$$

The test values for P and M are 21.4 kips (95.2 kN) and 77.3 kip-in. (8.81 kN-m), which are quite comparable to the computed results of 22.2 kips (98.8 kN) and 72.6 kip-in. (8.20 kN•m) and provide a check on the proposed analysis to estimate P and M for negative eccentricities. The test results are shown on the moment thrust failure envelope of Fig. 3.25.

The above computational procedure applied to specimen J-5 yields P = 6.9 kips (30.7 kN) and M = 39.3 kip-in. (4.44 kN•m), compared with test values of P = 12.3 kips (54.7 kN), and M = 71 kip-in. (8.02 kN•m). The sources of this discrepancy are two; first, the peripheral shear forces and associated moments have been ignored in the analysis of the center block containing the bolts and secondly, observations during the test indicated bearing failures at the bolt holes. However, for J-4, which had a smaller negative eccentricity and smaller initial bolt torque, the proposed analysis was acceptable since these complicating factors were insignificant.

The load capacity of J-5 may be predicted from a set of computations based on the failure mode of crushing on the compression zone of the mating surface. Thus, from Fig. 3.26(a), for e = 5.79 in. (147.1 mm) $2Q$ = 19.7 kips (87.6 kN); f'_c = 6.48 ksi (44.68 MPa), and k_1 = 0.73.

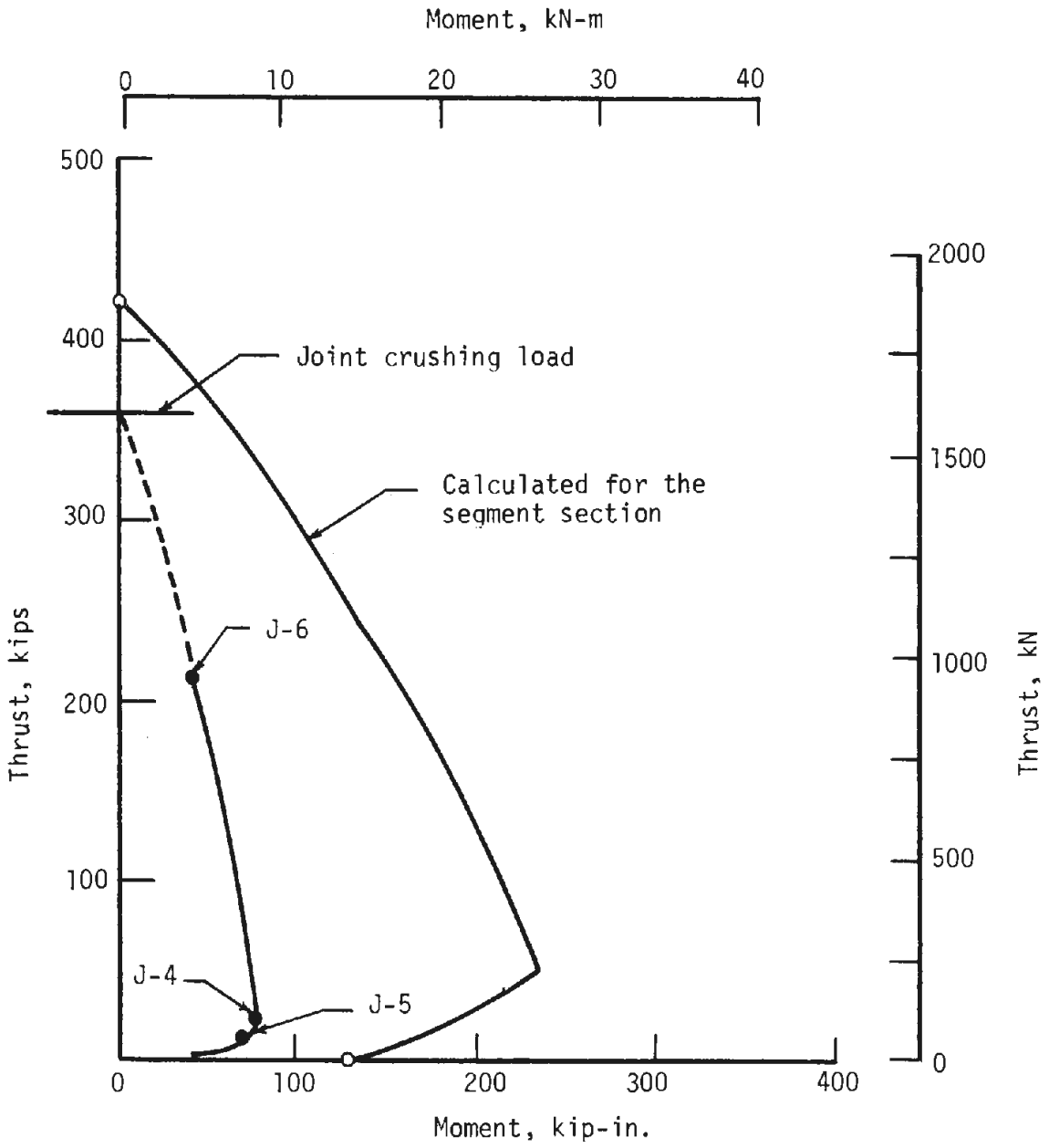

FIGURE 3.25 MOMENT-THRUST FAILURE ENVELOPE FOR THE SEGMENT AND JOINT SECTIONS, WITH NEGATIVE MOMENT

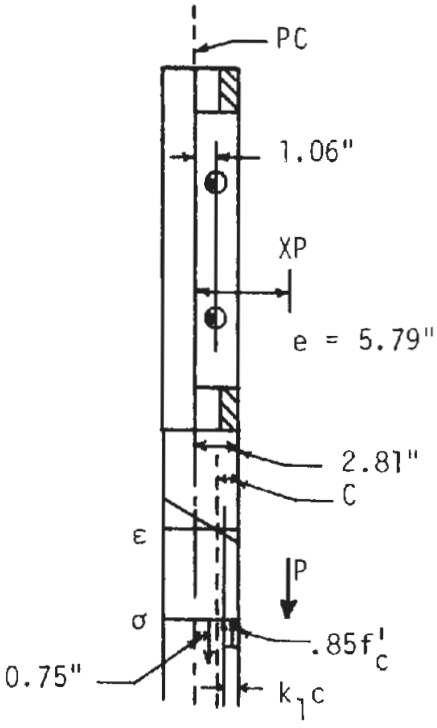

(a) Specimen J-5

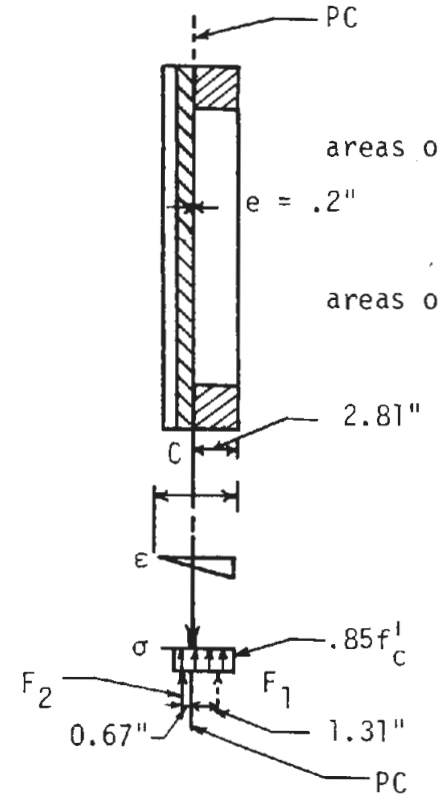

(b) Specimen J-6
areas of resultant force F_1

areas of resultant force F_2

1 in. - 25.4 mm

FIGURE 3.26 STRESS ON THE MATING SURFACE FOR SPECIMENS J-5 AND J-6

$$\sum F_v = 0 = -P \text{ kips} - 2Q \text{ kips} + 0.85 f'_c \text{ ksi } (k_1 \text{ c in.})(2)(3 \text{ in.}) = 0$$

$$= -P \text{ kN} - 2Q \text{ kN} + 0.85 f'_c \text{ MPa } (k_1 \text{ c mm})(2)(76.2 \text{ mm}) \cdot 10^3 = 0$$

$$\sum M_{PC} = 0 = -P \text{ kips (e in.)} + 0.85 f'_c \text{ ksi } (k_1 \text{ c in.})(2)(3 \text{ in.})(2.81$$

$$- k_1 \text{ c/2 in.}) - 2Q \text{ kips (0.75 in.)} = 0$$

$$= -P \text{ kN (e mm)} + 0.85 f'_c \text{ MPa } (k_1 \text{ c mm})(2)(76.2 \text{ mm})(71.4$$

$$- k_1 \text{ c/2 mm}) \cdot 10^{-3} - 2Q \text{ kN (19.0 mm)} = 0$$

which give c = 1.20 in. (30.5 mm), P = 9.3 kips (41.4 kN), M = 53.8 in.-k (6.08 kN•m); since c < 2.06 in. (52.3 mm), the assumption that the bolts are in the tension (opening) region of the mating surface is correct.

This same basic approach applied to specimen J-4 results in P = 19.5 kips (86.7 kN) and M = 70.4 kip-in. (7.95 kN•m), compared to the test values of 21.4 kips (95.2 kN) and M = 77.3 kip-in. (8.73 kN•m). To complete the discussion on specimen J-5, and based on Fig. 3.14, it is necessary to mention that a second region of distress probably occurred by crushing of the concrete under the bolt washers. For these tests, hardened washers were used with an inside diameter of 15/16 in. (24 mm) and outside diameter of 2-1/4 in. (57 mm). Thus, if the bolt is in contact with the side of the bolt hole, then the total nominal bearing area may be approximated by the area of the washer O.D. minus the area of the hole. This nominal bearing area is then 2.21 in.^{2} (1426 mm^2), which for the maximum bolt load of 11.0 kips (48.9 kN) results in a nominal average

stress of 5.0 ksi (34.5 MPa). This compressive stress is 77 percent of f'_c which is indicative of possible local compression failure.

The loss of bolt force due to creep was large for J-5 relative to J-2 in which the bolt torque was only 100 lb-ft (136 kN•m). The creep was higher in specimen J-5 because of the higher stress under the washer, and also there was a slight amount of very fine cracking observed in this specimen due to the initial bolt torque. The higher bolt force is desirable for strength and waterproofing, and could be used by increasing the washer bearing area.

In Fig. 3.25 the failure envelope for the segment and the approximate envelope for the joint subjected to negative moment are shown as constructured approximately from the test data. Test J-4 appears to approximate the balanced condition for the joint and test J-5 falls below J-4 in the tension failure region. The moment at zero axial load was found by assuming that the maximum bolt force was the same as determined from test J-4, and that the concrete stress was linear on the mating surface, and then calculating the moment corresponding to these assumptions.

Specimen J-6 was loaded at the computed plastic centroid for the segment section to determine a point on the upper portion (compression failure region) of the failure envelope. Some negative moment resulted in the test due to lateral deflection of the specimen, and the joint did not reach its theoretical axial strength. At failure a lateral displacement of 0.20 in. (5.1 mm) had occurred at the mating surface of the joint. The plastic centroid is not at the same location for the segment and joint and the plastic centroid does not coincide with the center of gravity in

the linear range; thus, the load was eccentric from the start of loading. This condition can start lateral deformation which will then continue to grow. Figure 3.18 shows that severe splitting cracks occurred in the segment parallel to the direction of compression. At higher loads, negative bending developed and cracks occurred in the segment portion on the outside of the shell surface. Near maximum load, crushing developed along the compression edge of the mating surface near the webs much the same way as in specimen J-4. The thrust and moment for specimen J-6 are shown on Fig. 3.25, where this point was also used in sketching the failure envelope.

Calculation of maximum axial load for the joint assuming compression failure on the gross area of the segment section gives the result of 358 kips (1592 kN) labeled "joint crushing load" on Fig. 3.25. This axial joint capacity is calculated on the basis that there is no reinforcement passing through the joint, and that no compression force is transmitted through the end diaphram, but only through the shell and side webs. Thus, the area used is the same as the segment area, but there is no reinforcement. The forces in the segment section are not uniform as there are much higher forces at the reinforcing bars. When these bars stop at the mating surface the stress distribution cannot suddenly become uniform so high forces are transmitted across the mating surface at the bars. The concrete will fail at these high stress zones before the force is reached which corresponds to maximum uniform stress. The center of gravity of forces on the mating surface may actually be nearer that in the segment section. Thus, the location of the resultant forces on the mating surfaces is difficult to find for calculation of moment about the plastic

centroid, and it is not possible to place the load at a point that will result in no moment for both the segment and the joint.

Computed values of maximum moment and thrust with an eccentricity of load equal to that which existed in test J-6 at the failure load are compared with the test values and with the pure thrust load in the table below. The basis on which the computations were made for an eccentricity

	Maximum load, kips (kN)	Moment at max·load, kip-in. (kN·m)
Test results for joint with e = 0.2 in. (5.1 mm); J-6	210 (935)	-42.0 (-4.75)
Computed for joint with e = 0.2 in. (5.1 mm); J-6	222 (988)	-44.5 (-5.03)
Computed maximum axial load for joint (e = 0.0 in.)	358 (1592)	0

of 0.2 in. (5.1 mm) is shown in Fig. 3.26(b), where the computed values of thrust and moment are associated with a neutral axis location 5.42 in. (137.7 mm) from the inside of the web. This means that the bolts are within the compression region of the mating surface. A change in the bolt tension would not be expected unless a force is applied that would overcome the pretension due to torque. A force that would do this is not expected under these conditions. This conclusion is substantiated in Fig. 3.20 where the bolt tension is shown to have remained unchanged during the test. Thus, the calculated moment and thrust at the mating surface are based on the assumption that the bolt tension and a corresponding force on the mating

surface are self equilibrating, and that the section is that of the segment but unreinforced. A standard beam-column analysis is then performed based on compression failure of the concrete.

In Table 3.3 the results are summarized for the joint tests and compared with prediction calculations. The values of calculated tensile strength in the concrete are compared with the splitting tensile strength for tests J-1 and J-2. Calculated values of thrust and moment at maximum

TABLE 3.3

COMPARISON OF TEST RESULTS AND PREDICTING EQUATIONS

Specimen number	Test results			Computations		
				e > 0	e < 0	
	f_{ct}, psi (MPa)	P, kips (kN)	M[1] k-in. (kN•m)	f_t,[2] psi (MPa)	P, kips (kN)	M, k-in. (kN•m)
J-1	795 (5.48)	42.5 (189.0)	+127.0 (14.35)	758 (5.23)	--	--
J-2	820 (5.65)	14.8 (65.8)	+ 74.8 (8.45)	620 (4.28)	--	--
J-4	--	21.4 (95.2)	- 77.3 -(8.73)	--	22.2 (98.8)	-72.6 -(8.20)
J-5	--	12.3 (54.7)	- 71.2 -(8.04)	--	9.3 (41.4)	- 53.8 -(6.08)
J-6	--	210.0 (934)	- 42.0 -(4.75)	--	222.0 (988)	- 44.5 -(5.03)

[1] Moment at maximum load; $M = P(e_o + \Delta)$

[2] Diagonal tension stress calculated at the maximum load, P

load are compared for the other three tests. In view of the uncertainty associated with the modes of failure and geometry of failure, the comparisons are quite reasonable.

In summary, several conclusions can be drawn from these tests which are useful in understanding the joint behavior. As the joint was constructed, it was more flexible and weaker than the segment section. The moment-thrust capacity is considerably less than that of the segment as shown in Figs. 3.22 and 3.25. The joint strength can be computed with reasonable accuracy provided the failure mode can be predicted. The real failure mode can be found by postulating all possible failure modes and electing the one giving the smallest ultimate load. Therefore, the segment joint can be redesigned to obtain the desired strength. For positive moment the calculation of strength is more straightforward than for negative moment. The strength can be improved for negative moment by using higher bolt forces, larger washers, and additional lateral reinforcement to prevent splitting. Also, the bolt hole size can be reduced to provide greater bearing area for the bolts. It may be necessary to change the dimensional proportions of the end diaphram to gain strength.

CHAPTER 4

TESTS OF LARGE-SCALE BOLTED SEGMENTED LINERS

4.1 INTRODUCTION

Three circular tunnel liners consisting of bolted reinforced concrete segments were tested with a loading that simulated tunnel ground loading. The segment design used was obtained by approximate scaling of the design for the proposed segmented concrete liner for the San Francisco Bay Area Rapid Transit system (Gamble, 1967; Bechtel Corporation, 1966). The resulting liner was 10 ft (3.05 m) outside diameter and 5 in. (127 mm) thick scaled from a design that was 17.5 ft (5.33 m) outside diameter and 7 in. (178 mm) thick.

The original design for the San Francisco system contained a large number of small pieces of reinforcing bars for shear reinforcement and ties. Fabrication of the reinforcement cage was therefore expensive and there was some feeling that with simpler reinforcement the cost of the segments would be reduced significantly. One objective of the tests was to determine if part or all of the secondary reinforcement could be replaced by randomly oriented steel fibers in the concrete. Therefore, the test segments were cast with 0.9 percent by volume of steel fibers in the concrete mix and only the primary circumferential and longitudinal steel reinforcement.

Most methods of analysis for interaction of tunnel liners with the ground require some measure of the relative stiffness of the liner and

medium. Evaluation of the segmented liner's stiffness or deformability is heavily dependent on the properties of the joints between the segments. Radial (longitudinal) joints are generally less stiff than the segment and open up slightly, resulting in a concentrated angle change at the joint. If the joints are staggered between rings, the amount of interaction between the rings depends on the slip that occurs on the circumferential joints. To determine the extent of this interaction, two single ring specimens and one 3-ring specimen were tested and the deformations measured. The equivalent uniform section properties that provide the same deformability of the liner as measured in the tests were determined and compared with the calculated section properties.

A description of the behavior of a tunnel liner includes its load-deformation characteristics to failure and the manner in which failure occurs. It also includes the extent of cracking, joint opening and any other occurrence that affects its strength and servicability throughout its useful life. Prediction of the behavior is an important step in the design of a liner. One objective of these tests was to measure the behavior so that the accuracy with which it may be predicted can be determined. This part of the investigation is not complete and this report describes primarily the experimental portion of the study. Also the measurements of overall deformation, joint rotation and joint opening may be used in studies of watertightness of segmented tunnel liners.

The loading system used for the tests is an approximation to typical ground loading. It represents an active load on the top of the liner with the corresponding reaction on the bottom. These forces are

equal so the shear stress at the interface between the ground and liner is not modeled. Radial lateral forces are also applied that are a function of the lateral deformation of the liner. Therefore, the test arrangement models the interaction of the liner with a passive resisting mechanism which represents the ground. The magnitude of all applied forces and the corresponding displacements of the loading points was measured. With this information, the accuracy with which an interaction analysis can predict the behavior can be determined. A series of 12 equally spaced loads around the liner distributed over about 8 in. (203 mm) was used; it is anticipated that prediction of behavior under more realistic ground loads will be possible from analysis if it is first done with the test loading.

Replacement of the shear reinforcement with steel fibers in the concrete was not a complete success in these tests as it appears that the liner failures may have been influenced heavily by lateral movement of reinforcing bars that precipitated an inclined crack through the section. Lateral bar movement resulted from the bending of circumferential bars at the end of the segment in the failure zone.

The equivalent uniform moment of inertia determined in the tests for the 3-ring specimen S3 was found to be on the order of one-third the calculated gross moment of inertia. The radial (longitudinal) joints in the tests were quite flexible so this probably represents a lower limit for the practical case. There was not a great deal of difference between the load-deformation stiffness of the 3-ring liner and the single rings tested, indicating that the interaction between rings is small with the type of circumferential joint used in these tests.

4.2 SPECIMEN PREPARATION

The specimens used for the bolted concrete segment liner tests were cast in the laboratory using steel forms fabricated in the laboratory shop. Only one or two segments were cast at a time, so some variability of the concrete between segments resulted. The same mix was used and the materials carefully proportioned by weight so this variability was probably less than would exist in practice. Once the segments were cast, they were bolted together in the test configuration; that is, with the longitudinal axis of the tunnel oriented vertically. Bending forces due to the self weight of the liner were negligable in the tests, and if important in a particular situation they could be superimposed on those that occur from the applied loads.

Three specimens were tested that have been designated S1, S2, and S3. All three were complete circular liners of segments bolted together. S1 and S2 were one ring long or 2 ft (610 mm), while S3 was three rings long or 6 ft (1.83 m). In each ring there were 7 segments, 5 of which were identical and encompassed a 60 degree (1.05 rad) arc of the circle. This type of segment will be called segment A. The remaining 60 degrees (1.05 rad) was made up of a shorter segment of 45 degrees (0.79 rad) designated as segment B and a key of 15 degrees (0.26 rad) designated as segment K. All the segments had a waffled configuration on the inside to allow for bolting on all sides.

Thickness of the segment was 5 in. (127 mm) with a 2 in. (51 mm) thick shell or flange and the ring was 10 ft (3.05 m) outside diameter in the assembled configuration.

4.2.1 FABRICATION

Forms were constructed of 1/8 in. (3.2 mm) steel plate bolted together for convenient assembly and removal from the specimen. Pans to form the hollow inside of the segments were first made of wood but they were damaged when removed. Pans were then made with steel plates bolted together so that they could be disassembled for removal. A photograph is shown in Fig. 4.1(a) of a form with wood pans and the reinforcing bars, and in Fig. 4.1(b) of the form with steel pans.

Holes were cast at the side and end webs for bolting segments together in the circumferential and longitudinal directions. The holes were 1-1/8 in. (29 mm) diameter for accepting 7/8 in. (22 mm) bolts. The inside surfaces of the webs around the holes were made parallel to the outside surface of the web so that the bearing of the bolt head and nut would be on parallel surfaces.

Reinforcement consisted of circumferential and longitudinal reinforcing bars and random steel-fiber-reinforcement in the concrete. The steel bars were #3 and #4 (9.52 and 12.70 mm dia.) bars, grade 40 (275 MPa minimum yield stress) which were positioned as shown in Figs. 4.2 and 4.3. The volume percent of circumferential bar reinforcement based on the gross dimensions of the waffled segment section was 1.21 percent for the inside and 1.24 percent for the outside tension steel. In addition, bars were placed transverse to the segment or longitudinal in the tunnel. The purpose of these bars would be to help resist jacking forces from a shield or tunnel boring machine. Properties of the steel

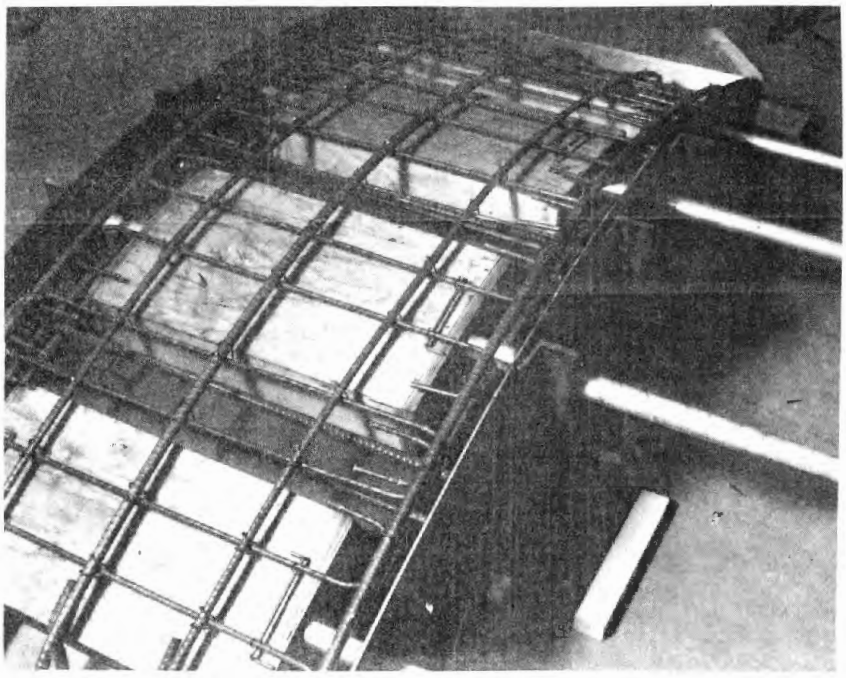

(a) Form with original wood pans and reinforcement

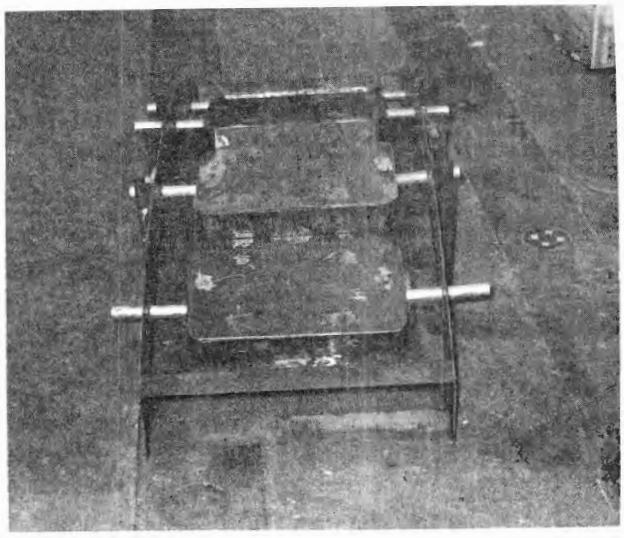

(b) Form with steel pans

FIGURE 4.1 PHOTOGRAPHS OF SEGMENT FORMS

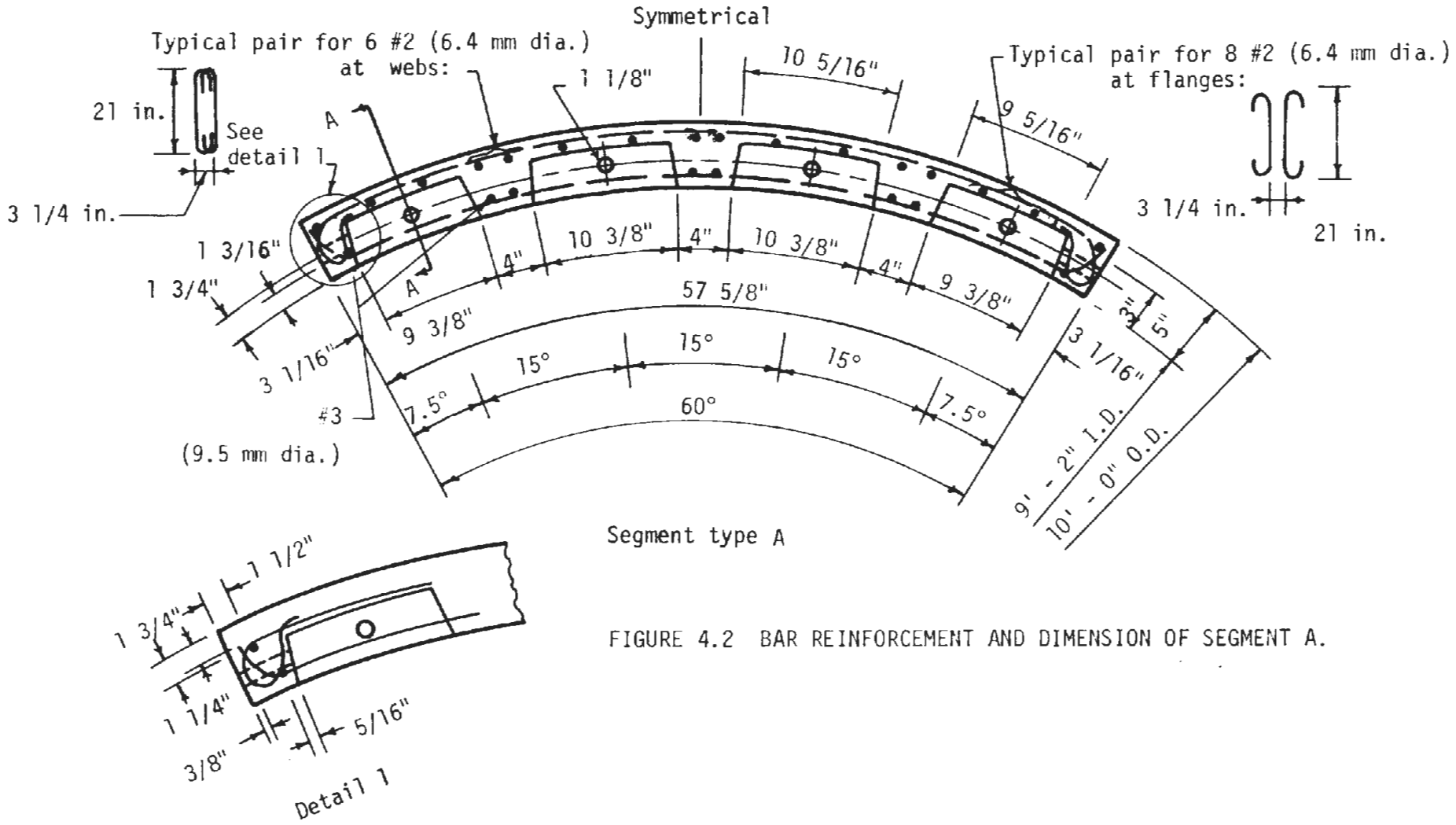

FIGURE 4.2 BAR REINFORCEMENT AND DIMENSION OF SEGMENT A.

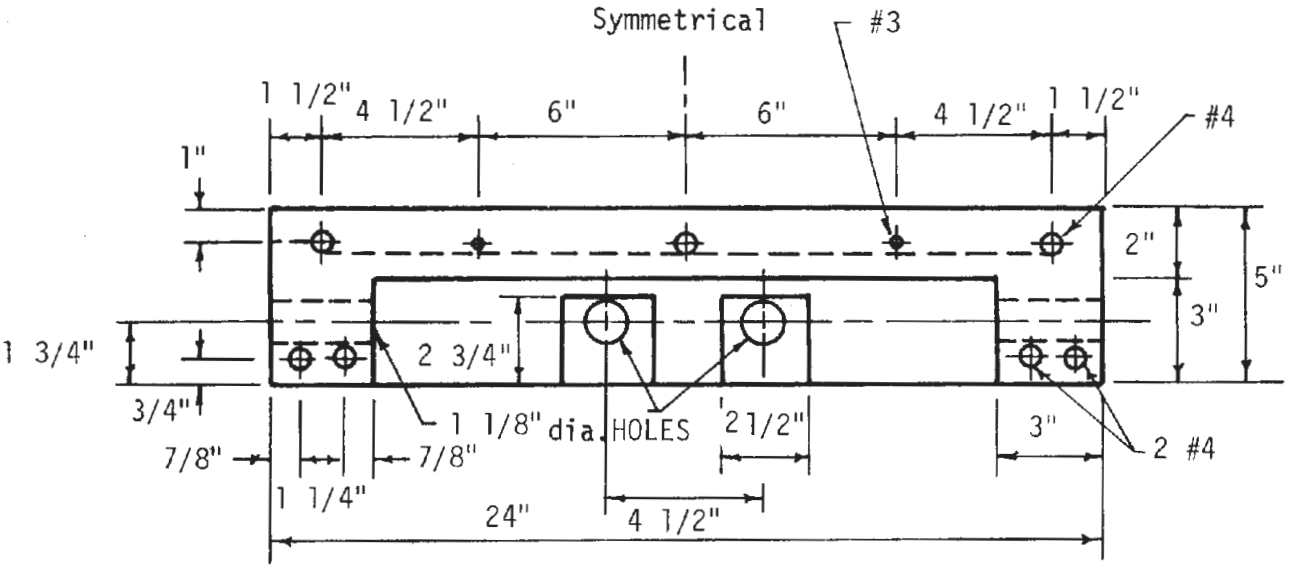

Section A-A

1 in. = 25.4 mm

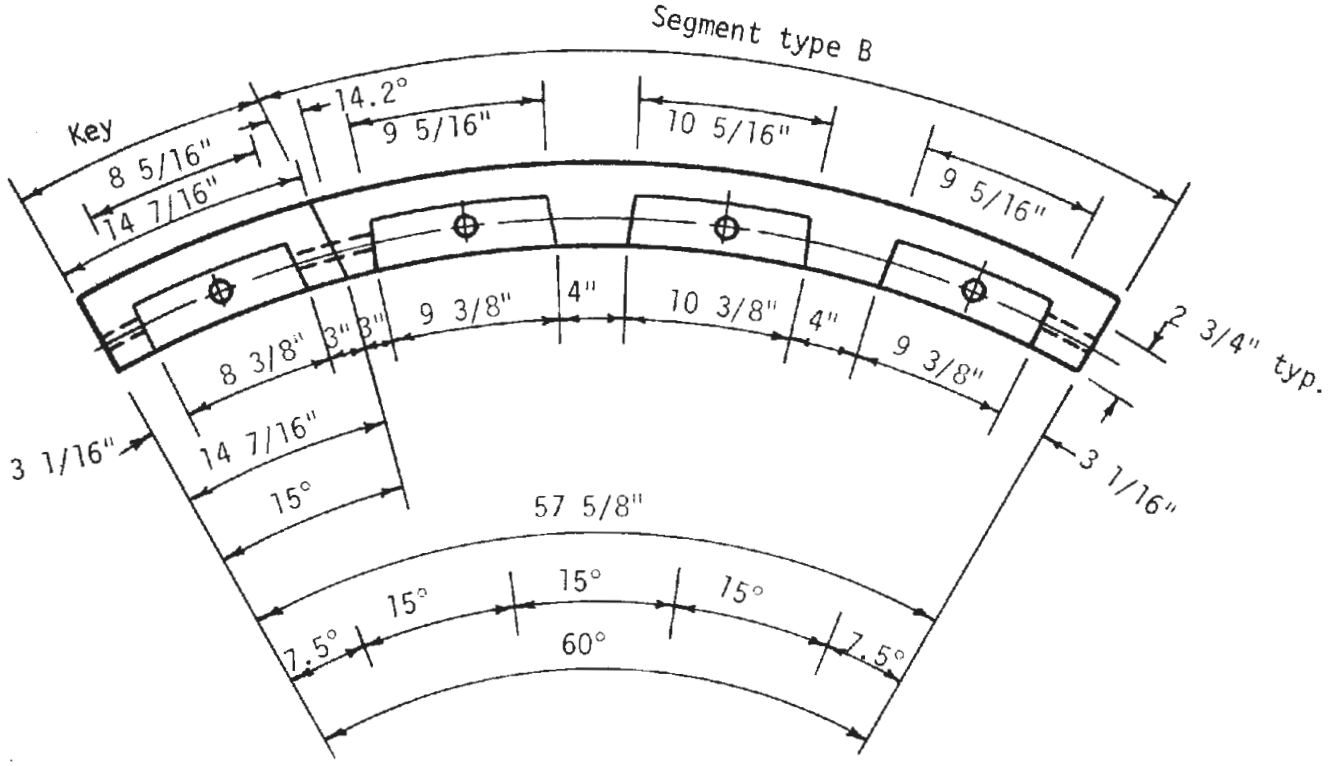

1 in. = 25.4 mm

Segments type B and K

FIGURE 4.3 CROSS SECTION OF SEGMENTS, AND DETAILS OF SEGMENTS B AND K.

bars are shown in Table 4.1 and indicate a yield stress of 50.2 ksi (346 MPa) for the #3 bars and 55.8 ksi (385 MPa) for the #4 bars.

The concrete was mixed in a 1/4-cu yd (0.20 m^3) pan type mixer. A fiber content of 0.9 percent by volume of USS steel fiber (Fibercon) was sprinkled into the mixer with the aggregate and cement. Then water and sufficient liquid air entrainer was added to provide a total air content of 5.5 percent. Properties of the resulting concrete are summarized in Table 4.1 for all three specimens. The average compressive strengths varied from 5900 to 6400 psi (40.70 to 44.15 MPa) and the modulus of rupture from 875 to 925 psi (6.03 to 6.38 MPa). The average strengths were obtained by testing cylinders from every batch of concrete. The modulus of elasticity varied from 3,120 to 3,310 ksi (21.50 to 22.80 GPa) which is below the values that would be obtained by the formula 57,000 $\sqrt{f'_c}$ suggested in ACI 318-71. The reason for the lower values lies in the method of test. A 600 kip (2670 kN) hydraulic testing machine was used with head movement control set at 0.01 in./min (0.25 mm/min) for tests of cylinders for rings S1 and S2, and 0.03 in./min (0.76 mm/min) for test S3. This was done to obtain a stress-strain curve that is more typical of the liner test conditions and to obtain the descending branch of the curve. A typical stress-strain curve obtained this way is shown in Fig. 4.4 where the peak strain occurs at 0.003 and the initial modulus of elasticity is 3,280 ksi (22.60 GPa). The presence of the fibers may cause a larger strain at peak stress than occurs in conventional concrete tested as a faster rate.

When casting the segments, they were vibrated on a shake table

TABLE 4.1

SUMMARY OF MATERIAL PROPERTIES

Concrete

Specimen	Compressive strength, psi (MP_a)	Modulus of rupture, psi (MP_a)	Splitting tensile strength, psi (MP_a)	Modulus of elasticity, ksi (GP_a)
S1	6400 (44.15)	875 (6.03)	655 (4.52)	3220 (22.20)
S2	6200 (42.75)	870 (6.00)	640 (4.41)	3120 (21.50)
S3	5900 (40.70)	925 (6.38)	615 (4.24)	3310 (22.80)

Reinforcing bars

Bar Size*	Yield stress, ksi (MP_a)	Ultimate stress, ksi (MP_a)
#3	50.2 (346.0)	75.6 (521.2)
#4	55.8 (384.5)	90.6 (624.5)

*Bar areas: #3 = 0.11 $in.^2$ (0.71 cm^2)
#4 = 0.20 $in.^2$ (1.29 cm^2)

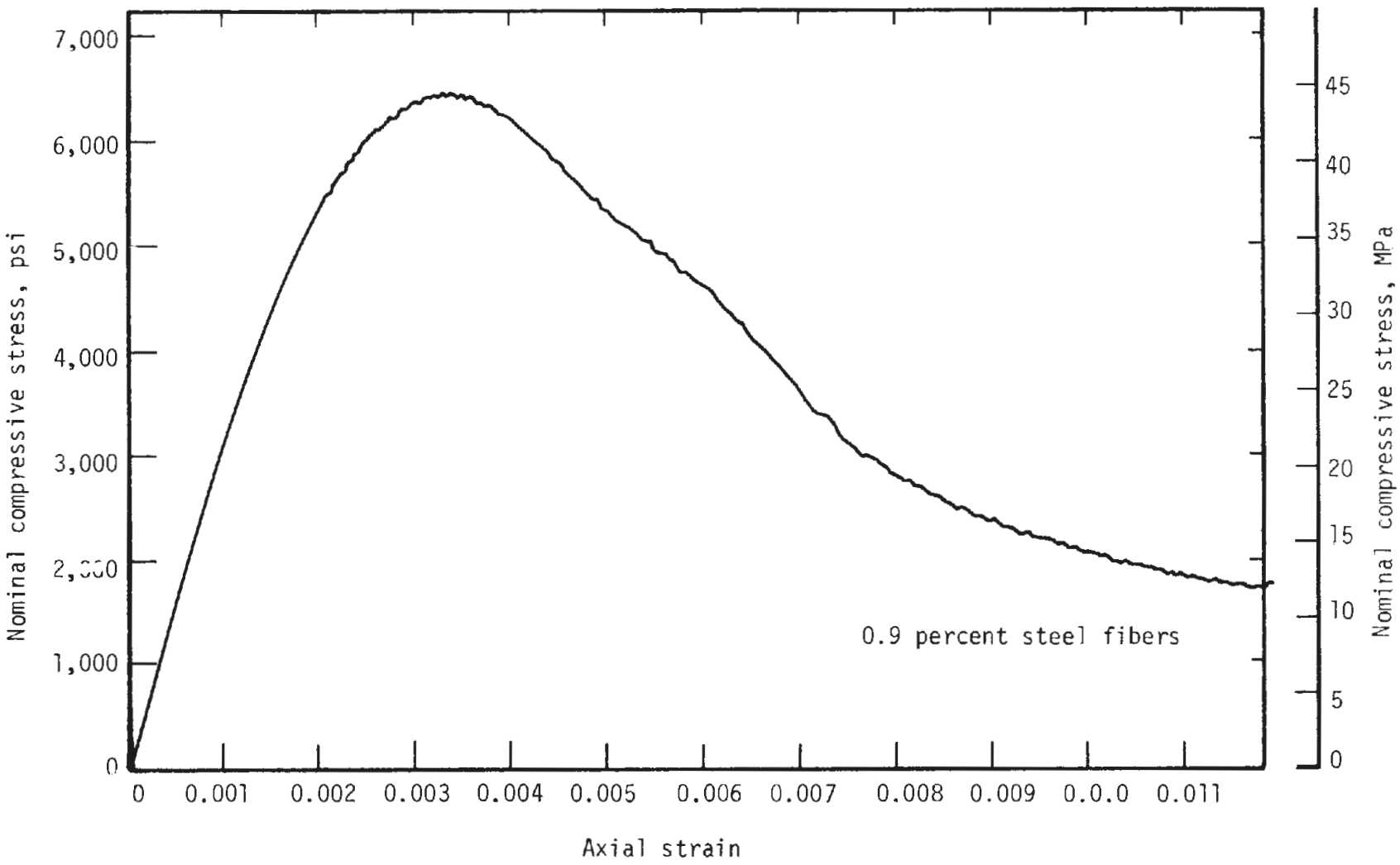

FIGURE 4.4 TYPICAL STRESS-STRAIN CURVE FOR STEEL FIBER REINFORCED CONCRETE

and cured under wet burlap and plastic sheeting for 7 days. After 7 days, curing continued in the laboratory atmosphere until time of test.

The segments were assembled in a circular configuration in the test device to avoid moving the liner after assembly and subsequently bolted together with 7/8 in. (22 mm) bolts. All 3 rings were assembled in specimen S3 before the bolts were finally tightened. The bolts in longitudinal joints (ends of the segments) were tightened first.

The longitudinal joint surfaces mated well and did not require any treatment, but the circumferential joints did not mate well in specimen S3. Bolting together the poorly mated circumferential surfaces would have resulted in high local stresses and some initial cracking, so the joints were injection grouted. The bolts were tightened with a torque wrench to 150 ft-lb (203 N-m). Photographs of specimens S1 and S3 assembled for testing are shown in Fig. 4.5.

4.2.2 INSTRUMENTATION

Diameter changes were measured on 6 different diameters spaced 30 degrees (0.52 rad) around the specimen with both LVDT's and dial gages. The load applied by each hydraulic ram was measured with a load cell between the ram and the specimen.

Since the liner is an indeterminate structure 3 internal force components must be determined experimentally so that the variation in internal forces around the liner can be computed. To accomplish this, strain gages were placed circumferentially at four strategic locations near the quarter points on the inside and outside of the specimen in order to locate

(a) Specimen S1

(b) Specimen S3

FIGURE 4.5 SPECIMEN S1 AND S3 ASSEMBLED FOR TESTING

the points of pure thrust or zero moment. With these points of zero moment known, the moment and thrust can be calculated for any other section in the ring. It was realized that moment and thrust near a joint would be influenced greatly by it, and that the moments in each ring of segments in specimen S3 would be different. The loading was approximately symmetrical about 2 axes. However, the joint pattern is not symmetrical about the same axes so the moments and shears were not symmetrical.

The gages used to locate the points of zero moment at a typical location are shown in Fig. 4.6 for specimen S3 between the east and south sections. The number of gages that could be read automatically was limited, so four representative levels were gaged as shown, with 5 gages at each level. A total of 80 gages was then needed for 4 locations around the specimen on the inside and an equal number on the outside. A few additional gages were placed at the midheight of the segments on the outside as a check on the other readings. Specimens S1 and S2 were gaged like the middle segment of S3, as shown in Fig. 4.6, with strain gages near the top and bottom edges.

The electronic instrumentation was read automatically with equipment that successively switched the circuits and read the voltage across the instrument. The reading was printed by a teletype and punched on a paper tape. The tape was read by another teletype that sent the information to a computer where the data was processed and printed out as strain, load, or deflection depending on the type of measurement.

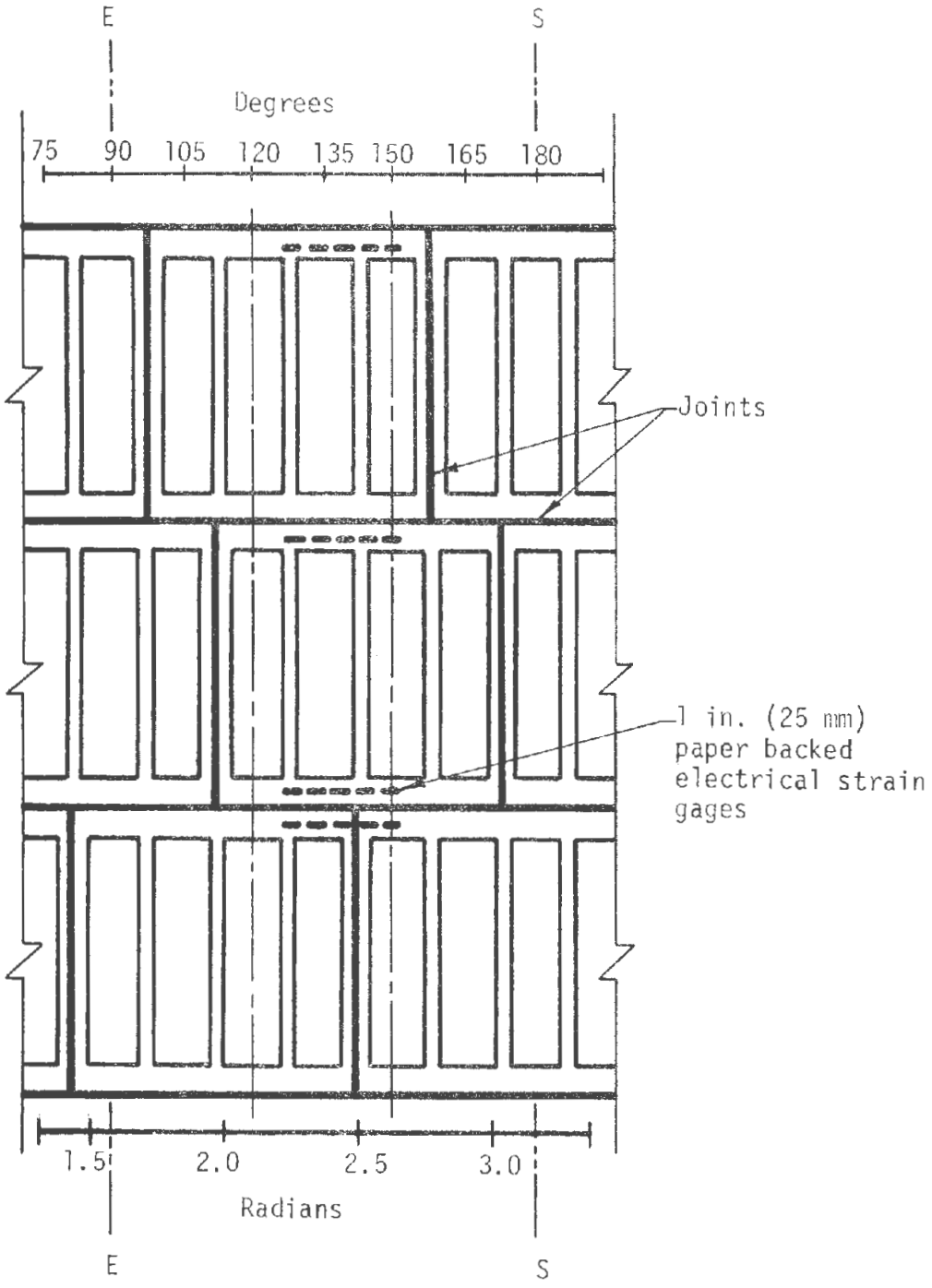

FIGURE 4.6 STRAIN GAGE LOCATIONS FOR SPECIMEN S3

4.3 TEST PROCEDURE

The test procedure was similar to that used for previous tests of monolithic liners reported by Paul, et al. (1974). Two 60-ton (535 kN) rams were used at each load point for specimen S3 and one ram for specimens S1 and S2. The load arrangement is shown in Fig. 4.7. Active loads were applied at 3 load points symmetric about the north and 3 symmetric about the south. The remaining rams on the east and west applied passive forces that were a function of the deformation of the load point. The rams applied load to the test specimen through ball joints and W8x48 (203

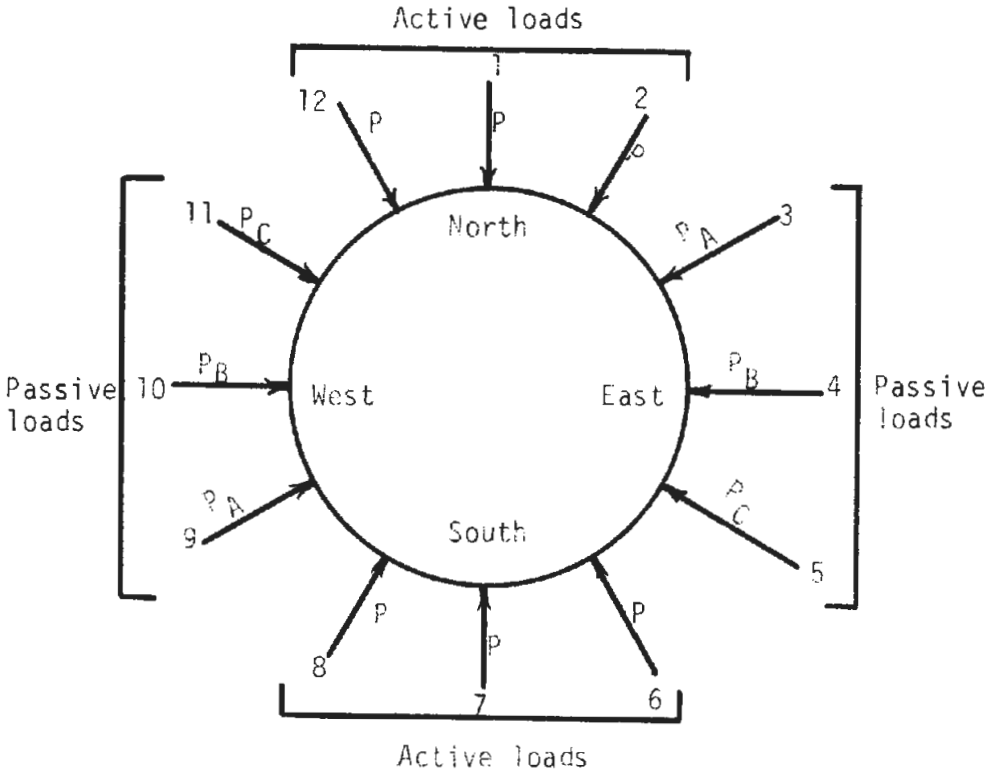

FIGURE 4.7 LOADING OF THE SPECIMENS

x 1210 mm) spread beams which were grouted to the specimen to assure uniform bearing. The loads were applied to the spread beam at points 12 in. (305 mm) and 60 in. (1524 mm) above the bottom of the specimen for S3. Load was applied at midheight of specimens S1 and S2. The ram reactions were resisted by concrete abutments bolted to the test floor as shown in Fig. 4.8 where the entire test arrangement is shown for specimens S1 and S3. A cylindrical bearing was placed between the ram and abutment to prevent transfer of a shearing force to the specimen at all load points except those at the north, south, east and west sections.

The weight of the specimen rested on nests of rollers between steel plates located 90 degrees (1.57 rad) apart at the north, south, east and west sections and oriented to roll in the radial direction.

All passive loads in all three tests were adjusted so that they would have a linear load-deflection relationship. This control was accomplished by connecting the load-point displacement (diameter change) to the X axis and the ram loads (average of loads at each end of the diameter) to the Y axis of an X-Y recorder so that the load and displacement could be continuously monitored. The load-deflection relationship desired was drawn on the graph paper of the recorder and during application of active load the passive load was adjusted so that the pen of the recorder followed the predetermined line. The loads were adjusted by manipulating the ram pressures.

The loading arrangement used in these tests ideally should cause only radial movement of the north, south, east and west load points because the loads were symmetrical about the north-south and the east-west diameters. Thus brackets were placed at these locations to allow movement

(a) Specimen S1

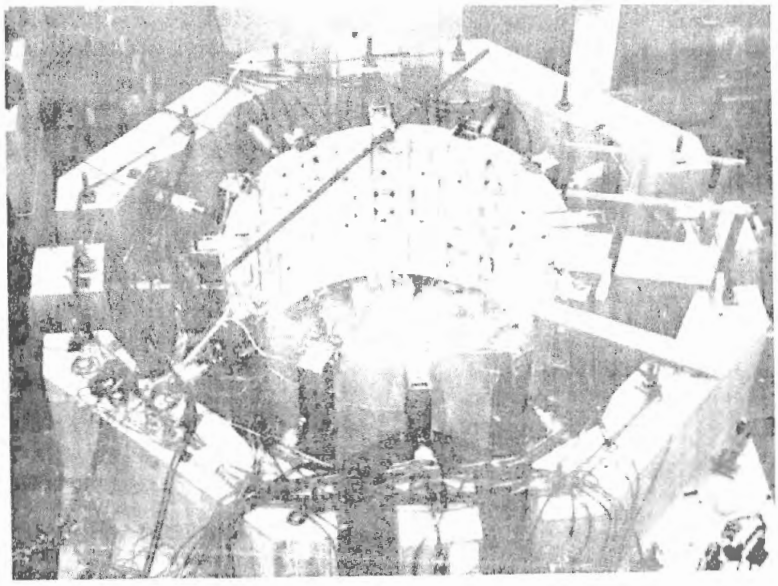

(b) Specimen S3

FIGURE 4.8 SPECIMEN S1 AND S3 READY FOR TESTING

only in the proper direction. These brackets, shown in Fig. 4.9, were placed at midheight of the specimen, and prevented tangential movement of the load spread beam. Rollers between the bracket and spread beam limited the radial force due to friction when radial movement occurred.

Load increments were applied by increasing the oil pressure to the active rams while the passive rams were adjusted. Once the load was attained all hydraulic valves were closed while instrumentation readings were taken. This required from 25 to 30 minutes and, at high load levels, the creep of the specimen allowed some loss of load. Loads were therefore read at the start and at the end of the instrumentation readings.

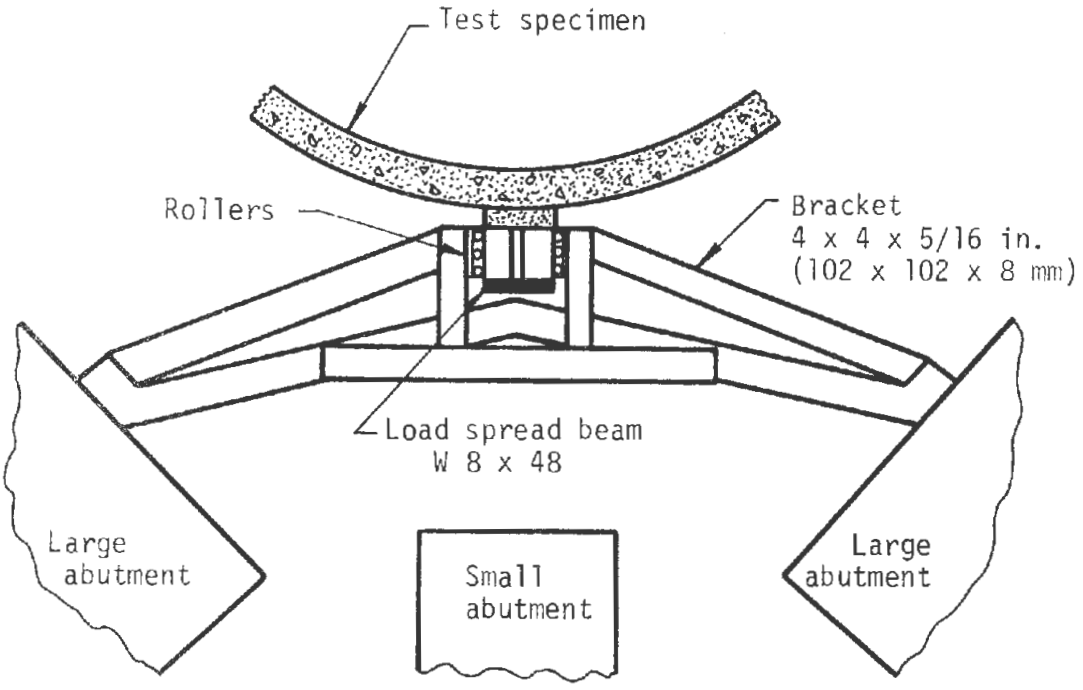

FIGURE 4.9 BRACKETS LOCATED AT THE NORTH, SOUTH, EAST AND WEST SECTIONS TO PREVENT RIGID-BODY MOTION OF THE SPECIMEN

Joint locations relative to the load points influence the distribution of shear and moment within the specimen. The layout of joints is shown in Fig. 4.10 for the three tests. Symmetry was maintained about the north-south axis for specimen S1 and S2, and for the middle ring of S3. The key in the top ring of specimen S3 was rotated 30 degrees to the west and in the bottom ring 30 degrees to the east. The average section properties for all three rings in specimen S-3 were therefore symmetric about the north-south diameter.

4.4 TEST RESULTS

Results of the 3 tests are presented in this section, and discussed and compared with other tests in the next section. Each specimen was loaded several times before the final loadings to check the instrumentation and loading mechanism, but the load level used for these check tests was very low, generally less than 5 kips (22 kN) average active load, so the specimen behavior under the final loading was not influenced by them. Consequently, only the last loading of each specimen is discussed.

It was intended that the passive forces have force-displacement behavior (stiffness) that would allow a direct comparison of the single ring behavior with that of the 3-ring specimen. Thus the stiffness of the passive load point should be 3 times as great for the 3-ring specimen as for the one-ring specimens. For the larger specimen a constant stiffness of 500 kips/in. (87.6 kN/mm) was selected which corresponds to 167 kips/in. (29.2 kN/mm) for each ring. The latter value was then used for the single ring tests.

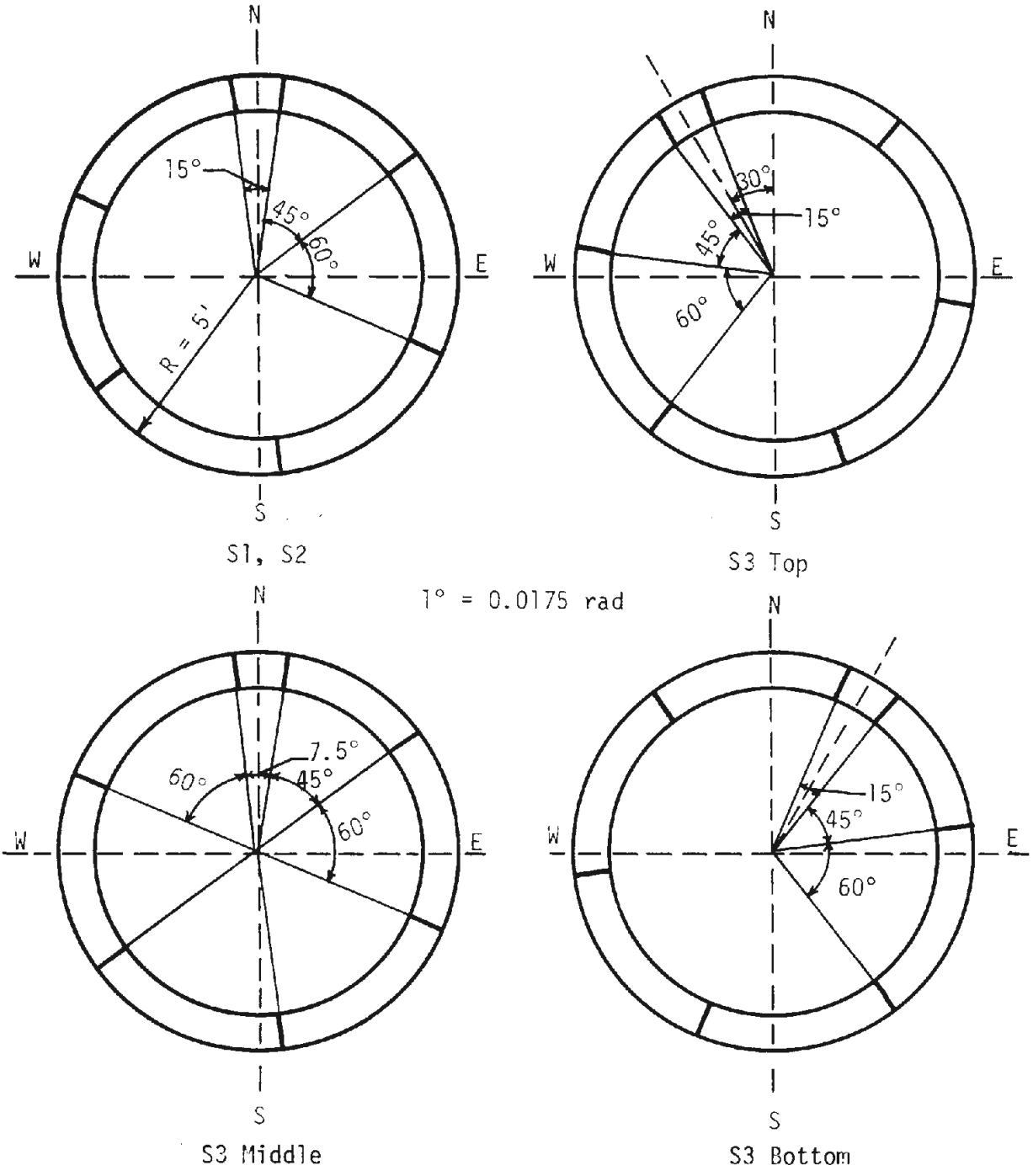

FIGURE 4.10 JOINT LOCATIONS FOR THE SEGMENTED LINER SPECIMENS

Passive forces influence the liner behavior a great deal; therefore, it is important to determine whether the intended passive force stiffness was followed and consequently to what extent the tests can be compared directly. Figures 4.11 to 4.13 show the force-displacement curves for the passive forces. The measured forces lying on the same diameter were averaged because the rams at these locations are connected hydraulically and therefore should have the same force. The displacement used is one-half the diameter change. For tests S1 and S2 the measured forces and displacements are shown, but the forces for test S3 were divided by 3 to obtain the value for one ring of segments for direct comparison.

There were some deviations from the intended passive force stiffness of 167 kips/in. (29.2 kN/mm) as indicated by the average stiffness shown on the figures. The effect of these deviations is to influence the deformation of the liner and thus the moments in the region of the associated force. Maximum deviations from the intended stiffness were -4 percent for S1, +10 percent for S2 and -7 percent for S3.

Deformations associated with the application of active loads are a significant measure of overall structural response. Figures 4.14 to 4.16 show for each test the diameter change, ΔD, in the north-south and east-west directions as the average active load P increased; the active stiffness is defined as $P/\Delta 1$, as contrasted to the passive stiffness in Figs. 4.11 to 4.13 where the passive forces vs. one-half the corresponding diameter change are shown. Response up to failure was primarily linear, though in all cases there was some curvature of the north-south load-deformation curve near maximum load. This is most evident in test S3, though there

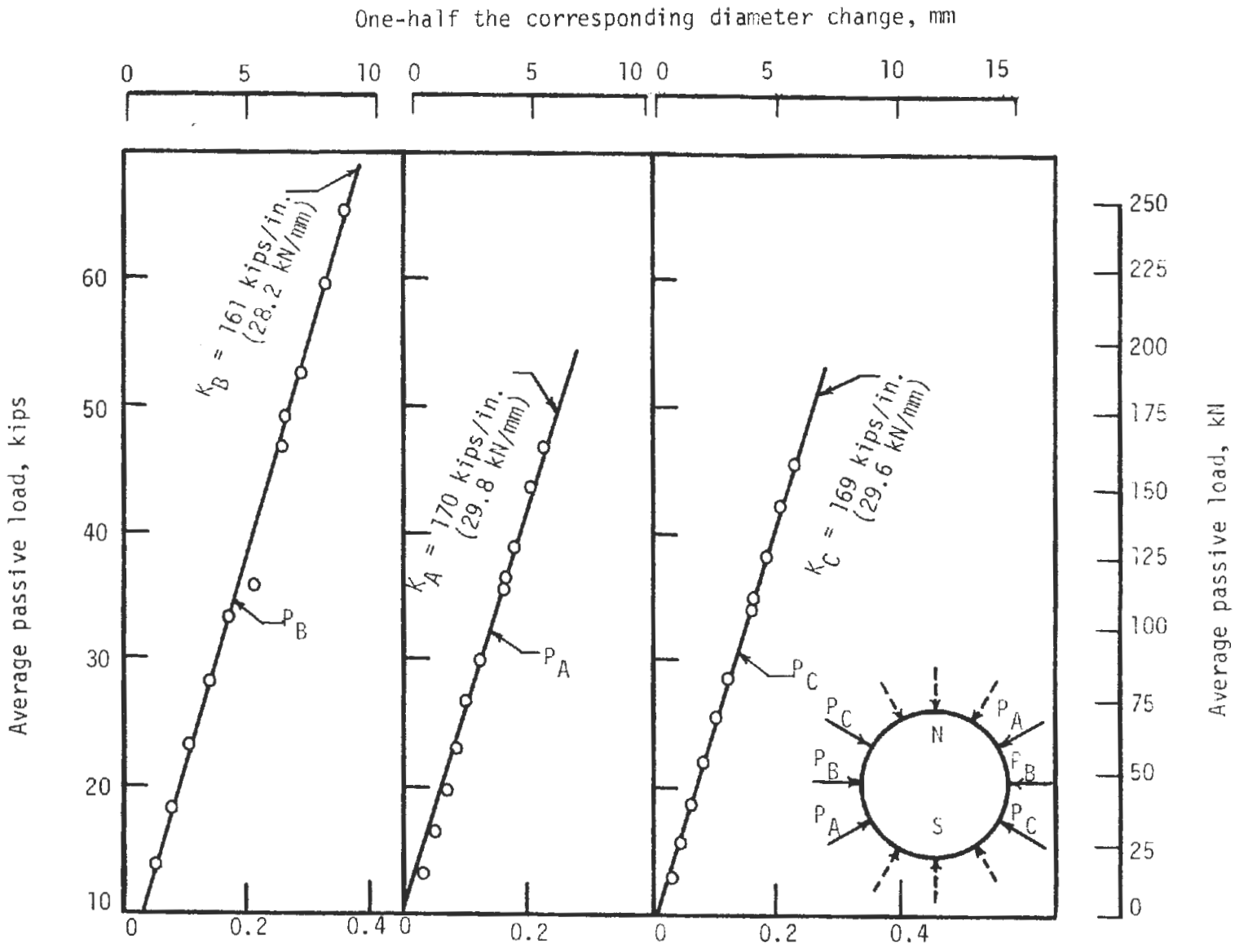

FIGURE 4.11 PASSIVE LOAD - DEFLECTION RELATIONSHIP FOR TEST S1

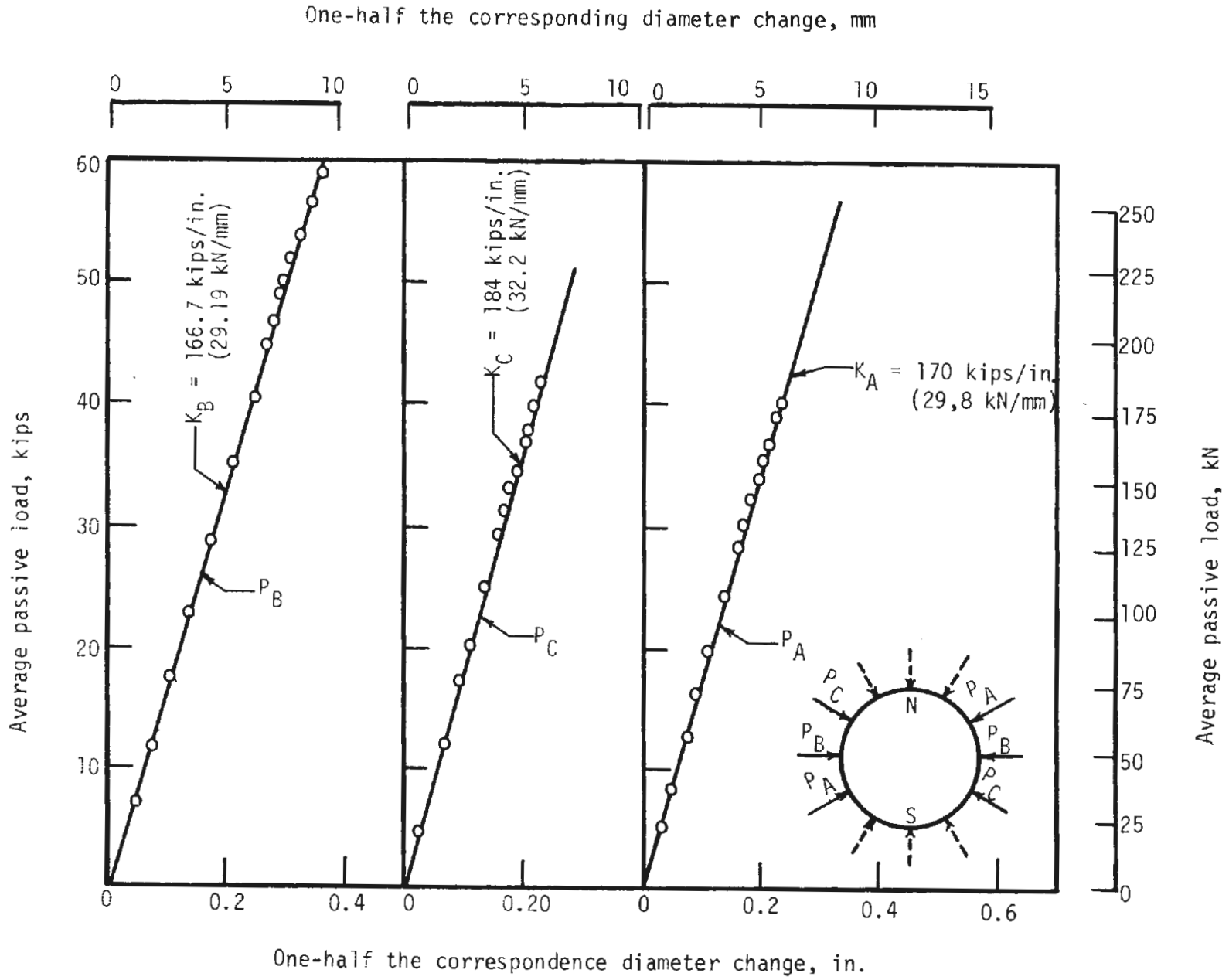

FIGURE 4.12 PASSIVE LOAD - DEFLECTION RELATIONSHIP FOR TEST S2

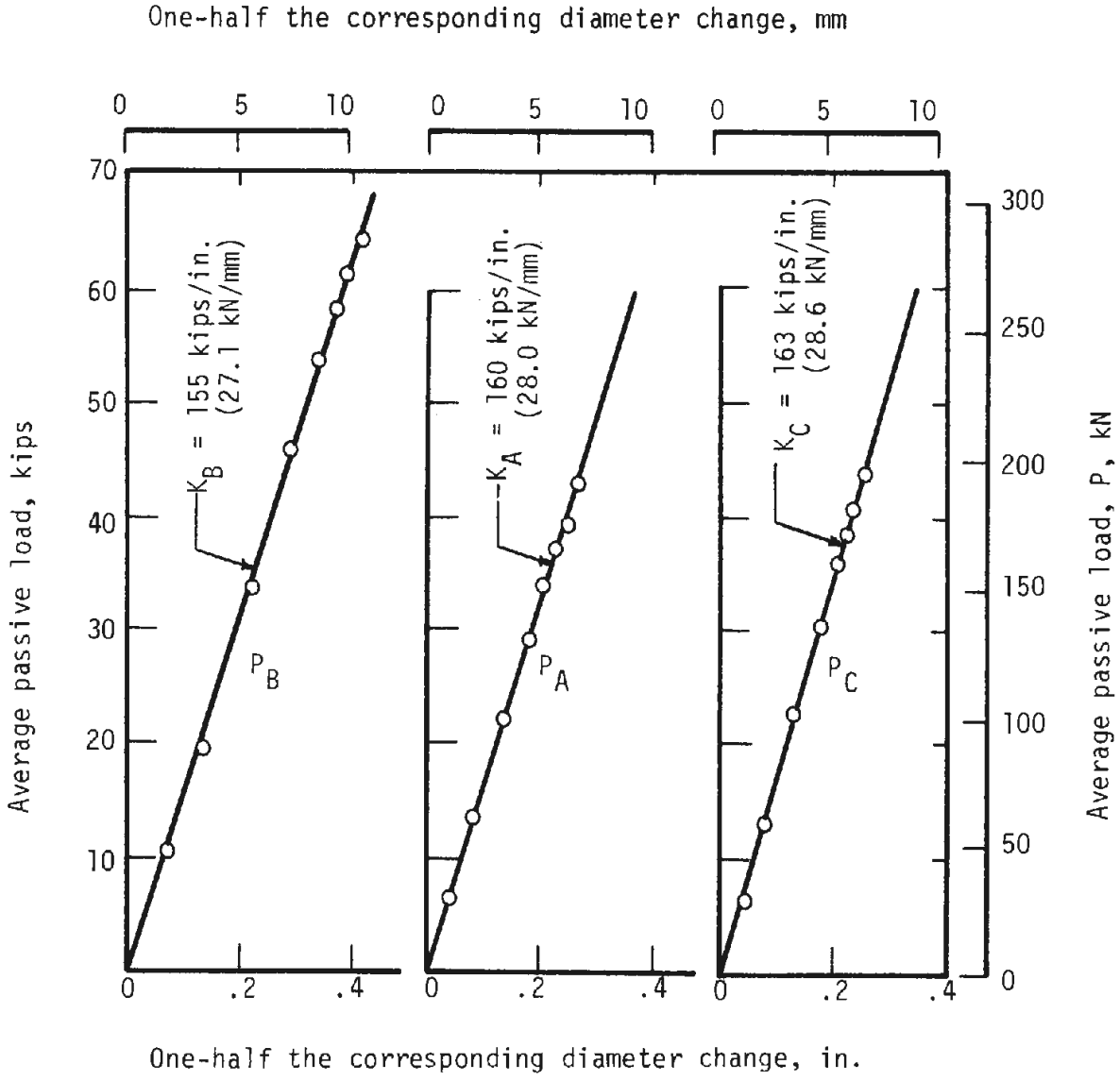

FIGURE 4.13 PASSIVE LOAD - DEFLECTION RELATIONSHIP FOR TEST S3

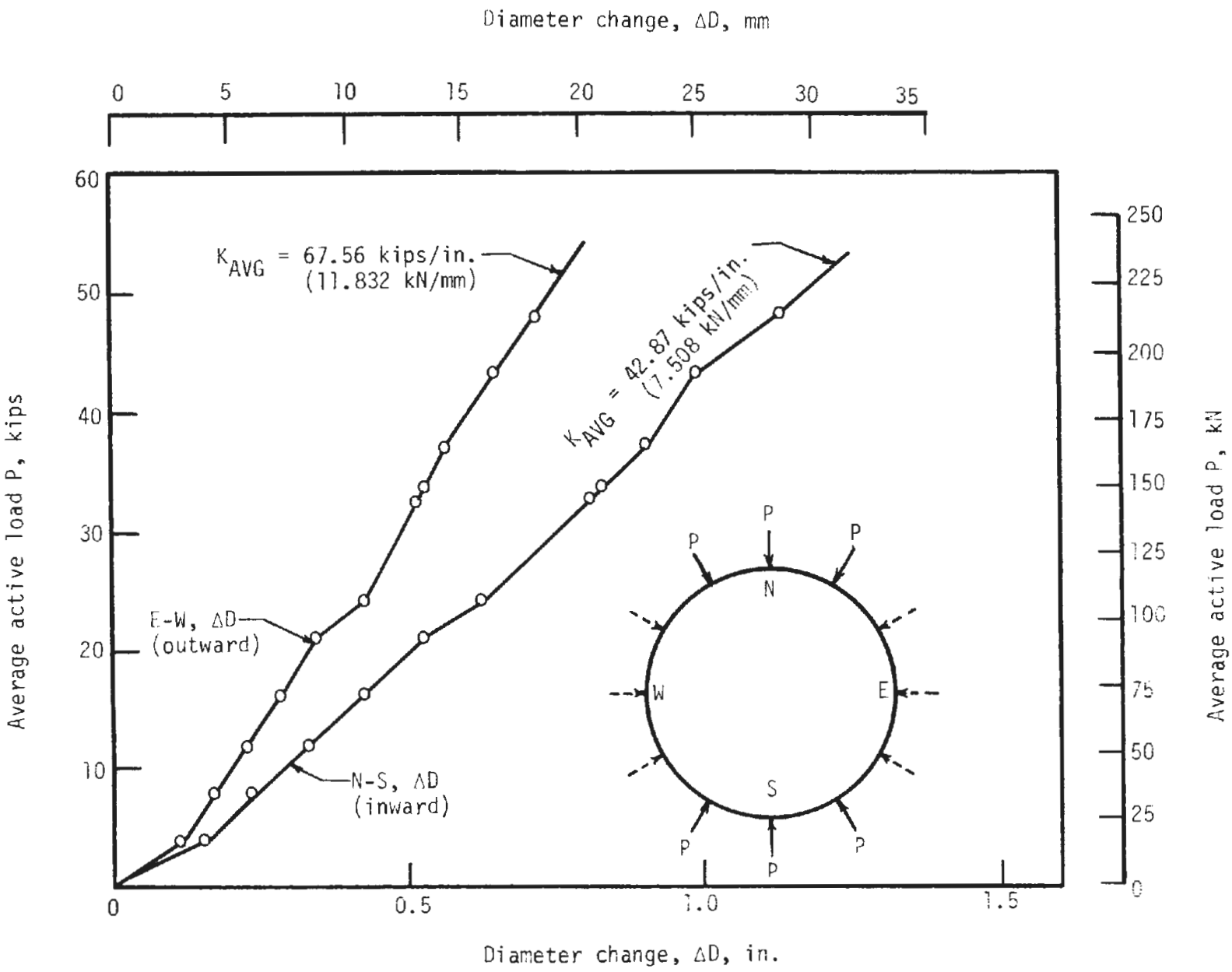

FIGURE 4.14 AVERAGE ACTIVE LOAD - DIAMETER CHANGE FOR TEST S1

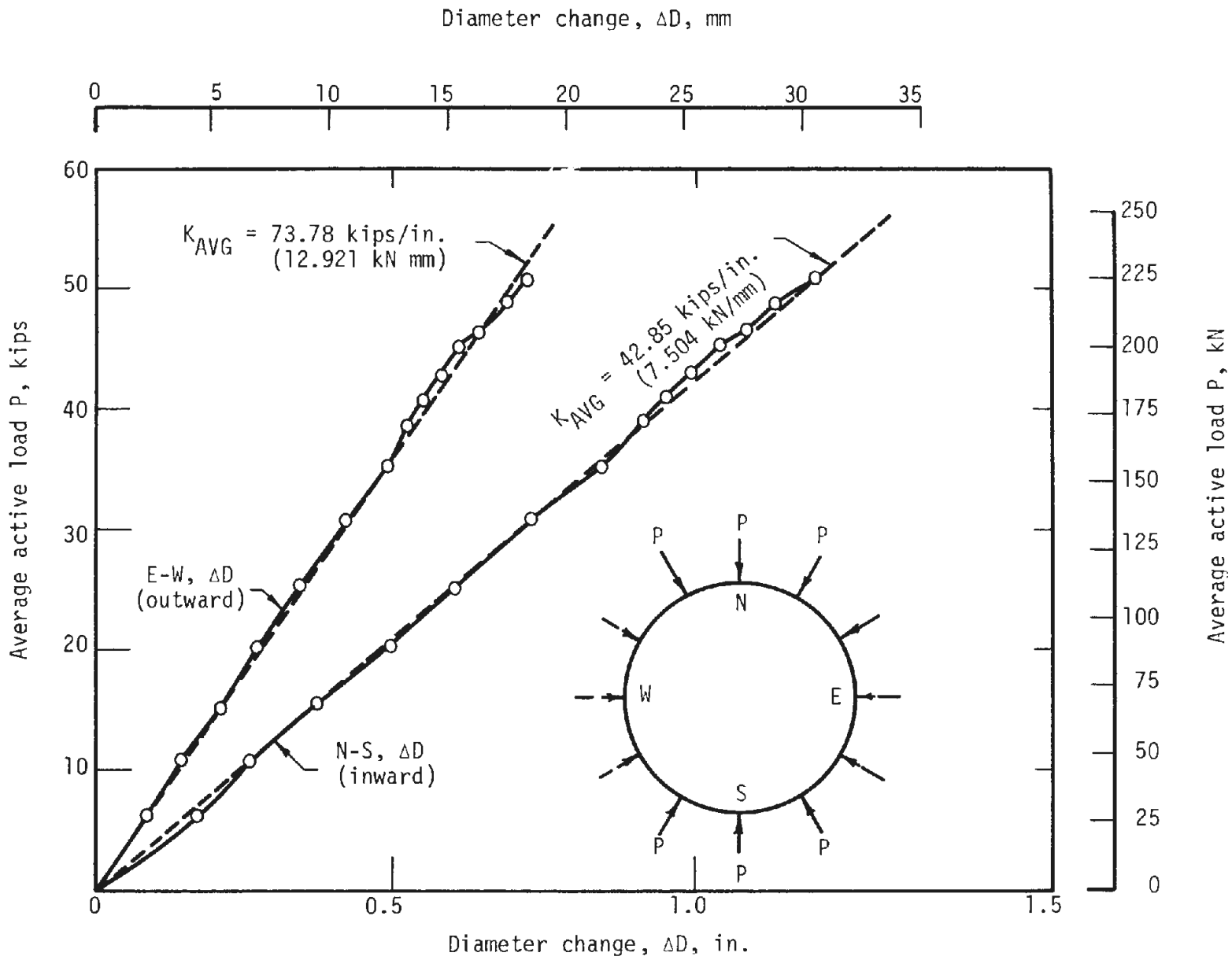

FIGURE 4.15 AVERAGE ACTIVE LOAD - DIAMETER CHANGE FOR TEST S2

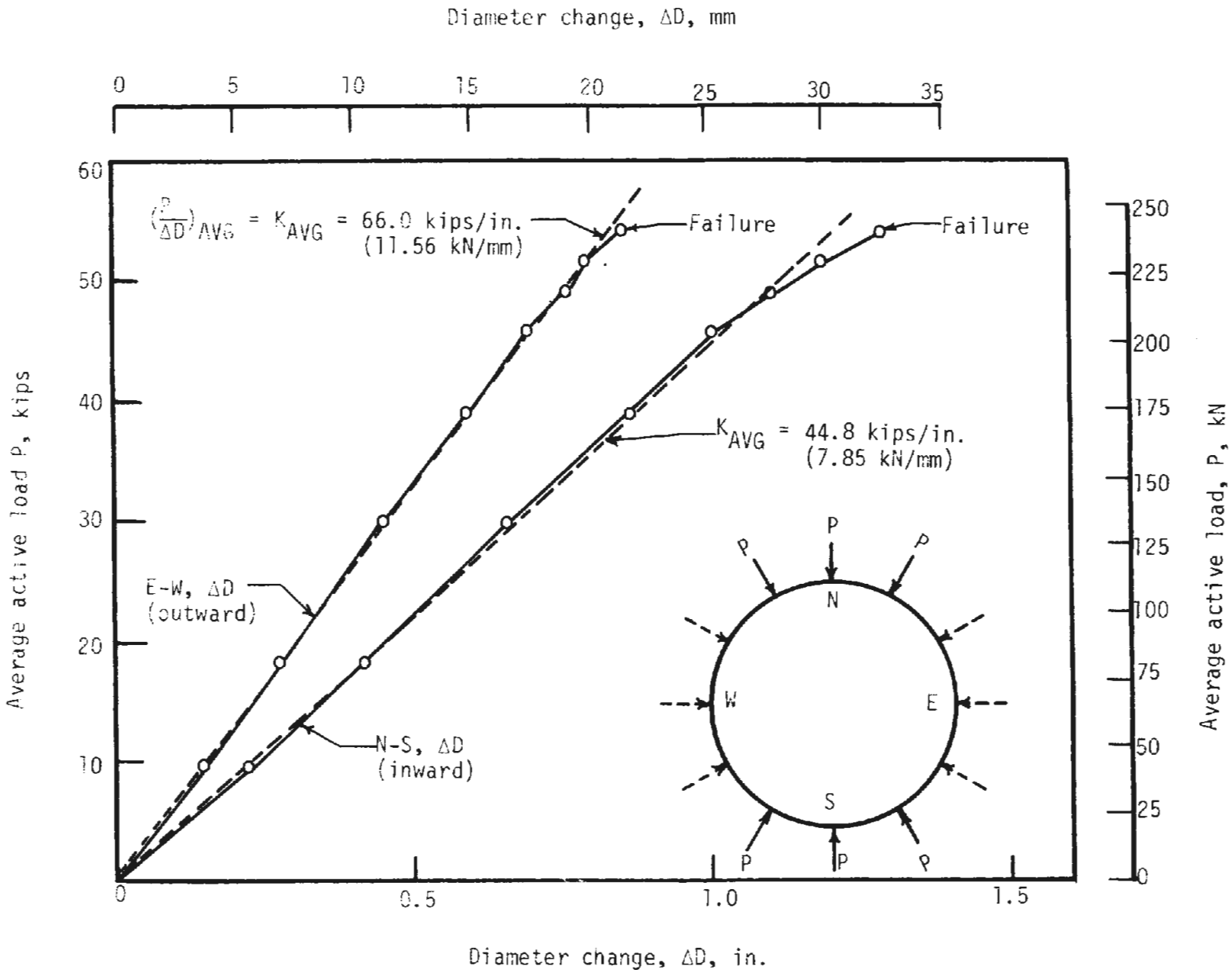

FIGURE 4.16 AVERAGE ACTIVE LOAD DIAMETER CHANGE FOR TEST S3

are some small deviations from linearity in the last load increment before failure in the other two tests. Thus it appears that the structure had just reached the nonlinear range shortly before failure.

The north-south diameter change is always larger than the east-west. Shortening of the circumferential axis due to thrust in the liner allows the north and south sections, where the active loads are applied, to move together more than the east and west sections move outward. Thus, the difference in these deformations is associated with the thrust.

The passive forces depend on both the passive force stiffness and the liner stiffness. In the linear range of behavior of the liner (the passive forces always remain linear in this case) the passive forces increase linearly with active load, and when the liner becomes nonlinear this relationship changes. In Fig. 4.17, the passive loads are shown as a function of active loads for the three tests. The relationships are almost linear. The range of values of P_A/P was 0.74-0.79 and P_B/P was 1.10-1.14. The active load P is the average of the forces P at each of the six active load points.

Prediction of maximum load requires an understanding of the internal mechanism of failure. The progress of cracking during the test and the appearance of the failure surface are also a valuable tool. The visual indications of failure will be considered first.

Specimen S1 failed suddenly so it was not possible to see where cracking began. The failure is shown in Fig. 4.18 where it extends from the joint just south of the east section to the load spread beam on the east over a circumferential distance of 18-1/4 in. (465 mm), while passing

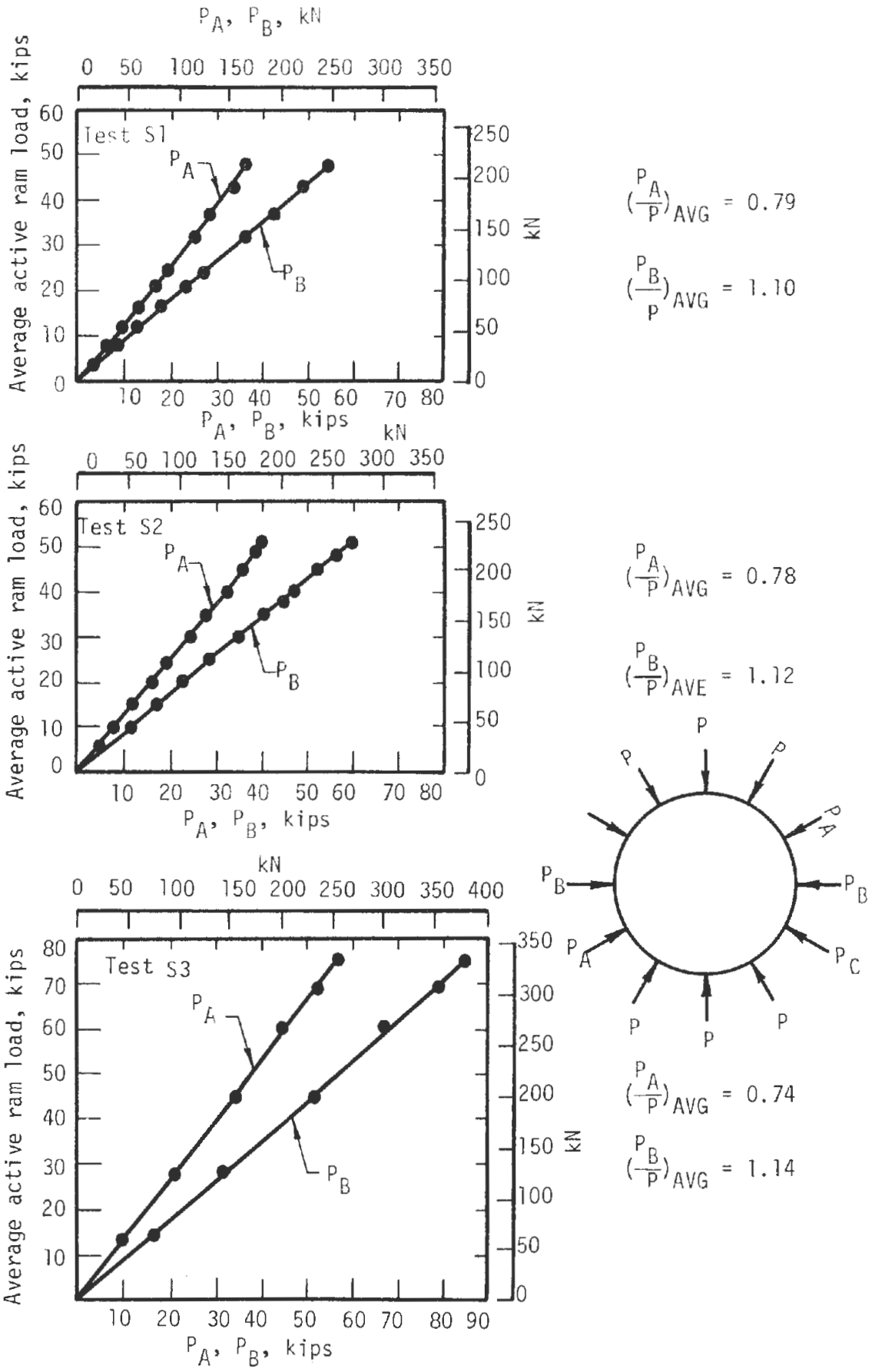

FIGURE 4.17 RELATION BETWEEN ACTIVE AND PASSIVE FORCES DURING TESTS

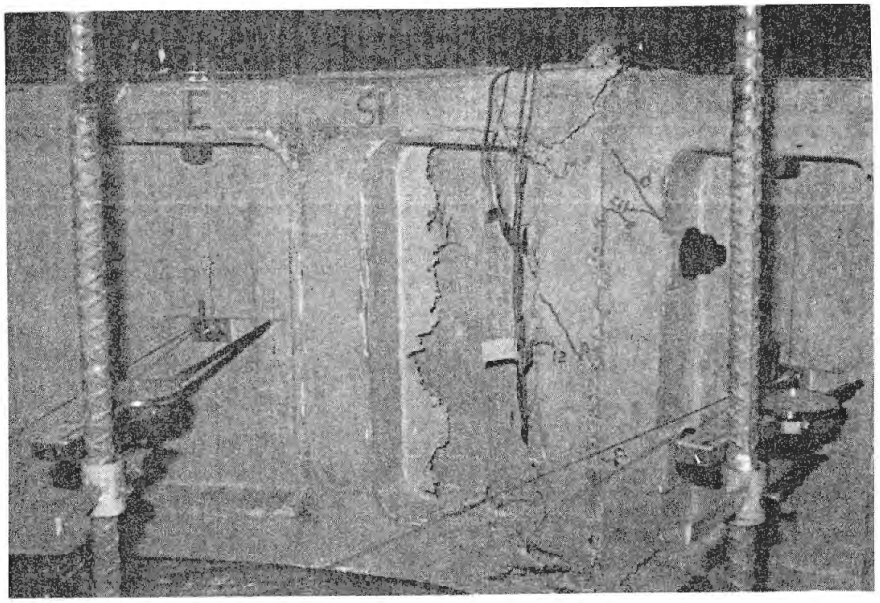

(a) View of failure from inside specimen

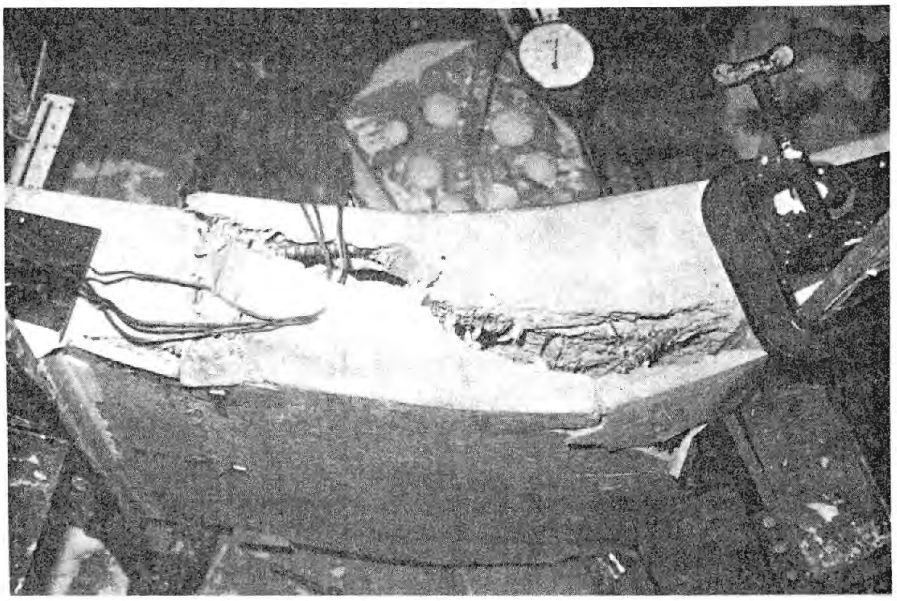

(b) View of failure from top edge of specimen

FIGURE 4.18 FAILURE REGION OF SPECIMEN S1

through one of the holes for the circumferential joint. The steel fibers protrude out almost perpendicular to the failure surface indicating the direction of movement of the surfaces, and that the reinforcing bars have buckled. The angle of the failure surface is about 15 degrees (0.26 rad) to the segment axis for the arc between the joint and bolt hole, whereas beyond this hole the crack gradually flattens out to reach the load spread beam.

Specimen S2 was tested in the same way as S1 in order to follow the progress of failure more carefully. It failed in the same location and at almost the same active load. Photographs of the failure are shown in Fig. 4.19 where the overall appearance is similar. By watching this region more carefully, a circumferential crack was noted on the top surface of the segment extending from the joint toward the east section. This crack appeared at an average active load of 40.5 kips (180.2 kN); remains of the marking may be seen in Fig. 4.19(b) at the joint between the two wires. This crack, plus the buclking of the bars, present the possibility that failure started as a splitting failure along the inside circumferential reinforcing bar at the joint. At this location the circumferential bars in the webs are bent toward the outside face of the segment. This bend with the large axial force in the bar due to bending and thrust probably caused a component of force in the bar toward the inside surface of the segment. The concrete could not resist the tension resulting from this radial component of force so the concrete split circumferentially allowing the bar to buckle. Without the resistance of these bars, the segment could not resist the thrust so the failure surface extended through the section

(a) View of failure
from inside specimen

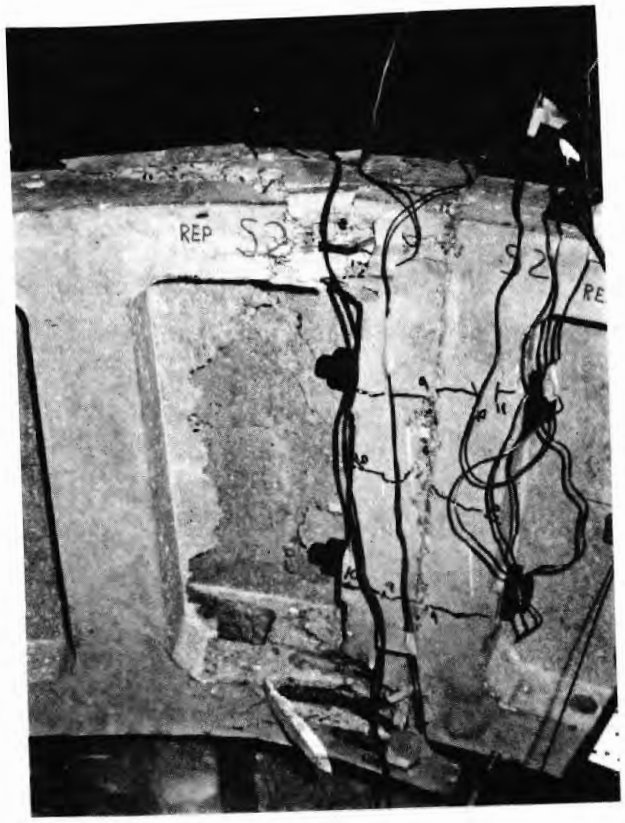

(b) View of failure from top edge of specimen

FIGURE 4.19 FAILURE REGION OF SPECIMEN S2

buckling the bars near the outside surface as well, and the concrete failed in a compression mode on an inclined surface.

This failure is similar in appearance to that experienced in the joint test J-4 described in Chapter 3 and shown in Fig. 3.14(a). In this test the eccentricity was small and the associated moment caused compression on the inside. The appearance of the end face of the failed segment from specimen S1 in Fig. 4.20 is similar to that of the joint end face in Fig. 3.14(a).

The failure of specimen S3 was similar to those in S1 and S2, as shown in Fig. 4.21. On the top surface of the top segment a crack essentially in the circumferential direction may be seen that formed at load increment 10 or an average active load P per ring of 46.9 kips (208.6 kN). The failure in each segment is associated with a joint and occurred between 35 and 50 degrees (0.61 and 0.87 rad) clockwise from north between loadpoints 2 and 3 (Fig. 4.7). Buckling of the reinforcing bars in the webs occurred near the joint on the inside and away from the joint on the outside as shown in Fig. 4.21. The failure was not as sudden in this case as for tests S1 and S2 and appeared to begin in the middle ring and progress outward. In addition, a crack had formed just west of the north section as shown in Fig. 4.22. It was a diagonal crack in a region of high shear and had opened up wide enough so it was clearly visible as shown in the figure. Thus it would appear that failure was imminent in this segment though it would not have been associated with a joint.

Typical crack locations for specimens S1 and S3 are shown in Fig. 4.23. Numbers on the marks indicate the approximate load increments

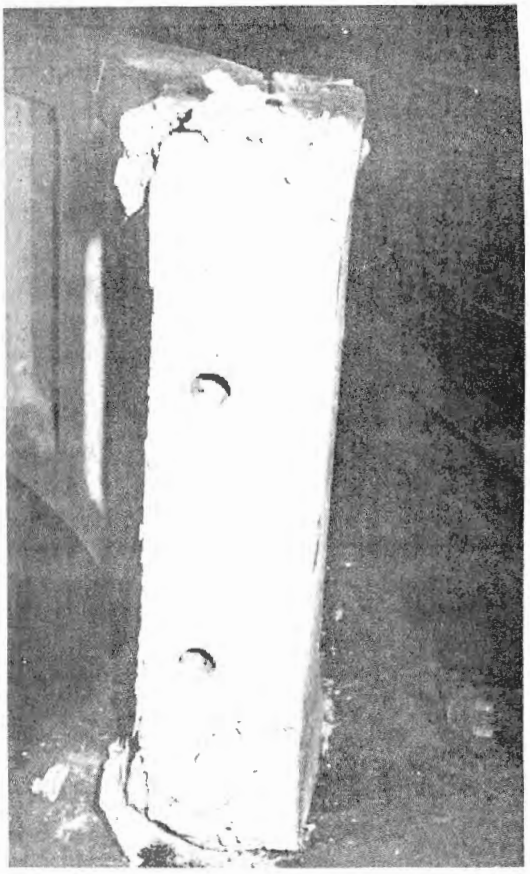

FIGURE 4.20 APPEARANCE OF THE END FACE OF THE FAILED SEGMENT OF SPECIMEN S1

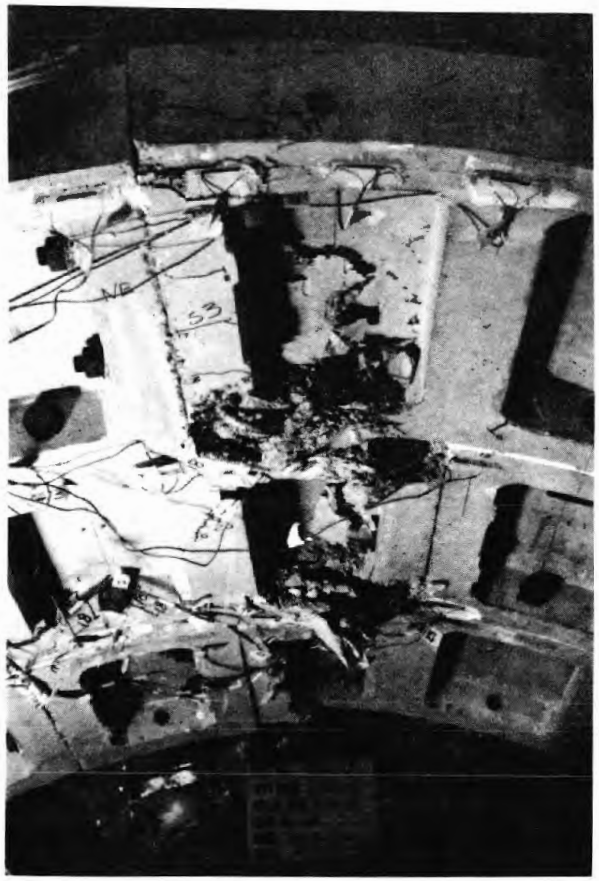

(a) View of failure from inside

(b) View of failure from outside

FIGURE 4.21 FAILURE REGION OF SPECIMEN S3

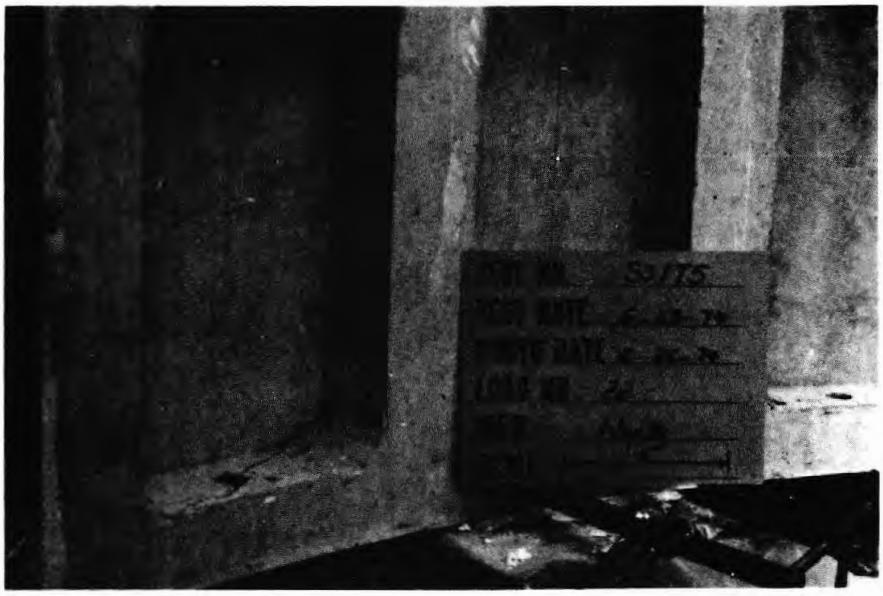

FIGURE 4.22 CRACK THAT FORMED NEAR THE NORTH SECTION OF SPECIMEN S 3

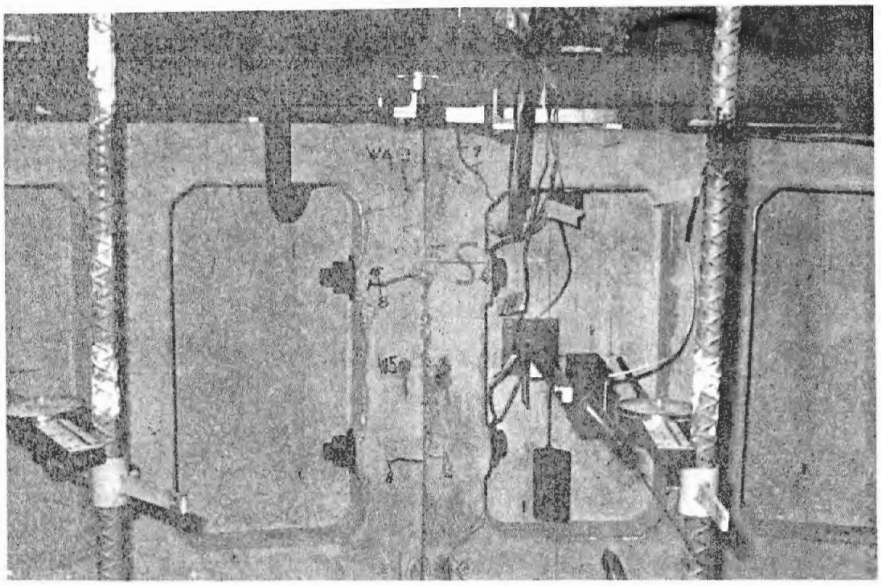

(a) Specimen S1

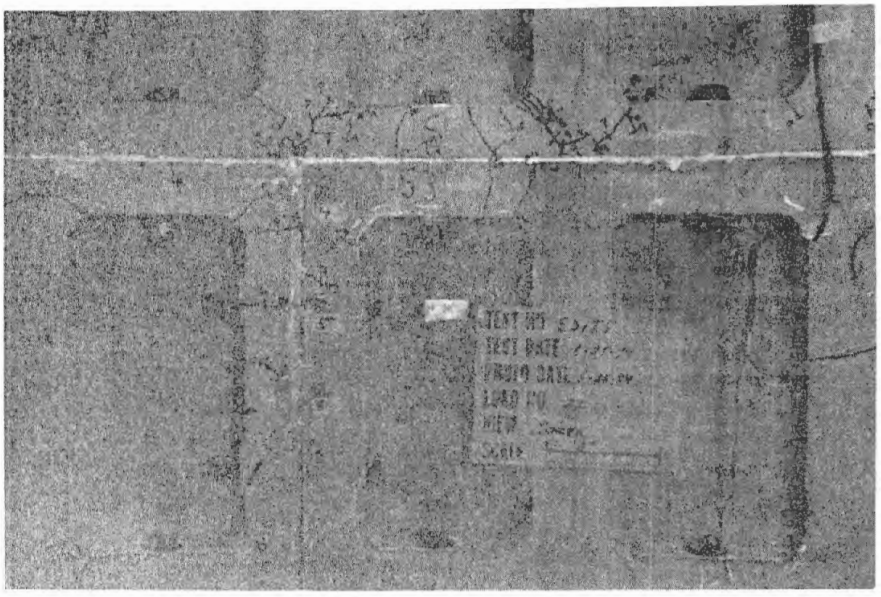

(b) Specimen S3

FIGURE 4.23 TYPICAL CRACK LOCATIONS NEAR THE SOUTH SECTION DURING TESTING OF S1 AND S3

at which the cracks formed. In general, cracks occurred at the corners where high tensile strains are concentrated, and parallel to the bolt holes through the end of the segments. Also in specimen S2 there were cracks across the segment webs on the inside surface associated with bending stresses.

Thrust, shear and moment in the region of failure for the last increment of load before failure are shown in Figs. 4.24 and 4.25 for the liner tests S2 and S3. The thrust, moment and shear at the section where failure started are similar in the two cases. The other curves on the plot of shear force will be discussed later. Failure began near the joint where thrust is high, moment is maximum, shear is small. Also moment is negative so the inside face, and thus the inside reinforcing bars, are in compression due to moment and thrust combined. For specimen S2 at the last load increment the maximum thrust was 91 kips (405 kN) and peak moment was 115 kip-in. (9.60 kN-m). For specimen S3 the thrust was 102 kips (453.5 kN) and moment 125 kip-in. The load per ring of segments at failure (total divided by 3) was larger for specimen S3, than the maximum loads for S1 and S2 (Table 4.2).

The internal thrust-moment paths for critical sections in specimens S2 and S3 are shown in Figs. 4.26 and 4.27. Also shown on these figures are the calculated failure envelopes for the segment section, and for the failure envelope from Chapter 3 for the joint when subjected to negative moment. For both tests the thrust-moment path is shown for the joint near the failure region and for the section of maximum moment shown on Figs. 4.24 and 4.25. These latter figures show the variation of the

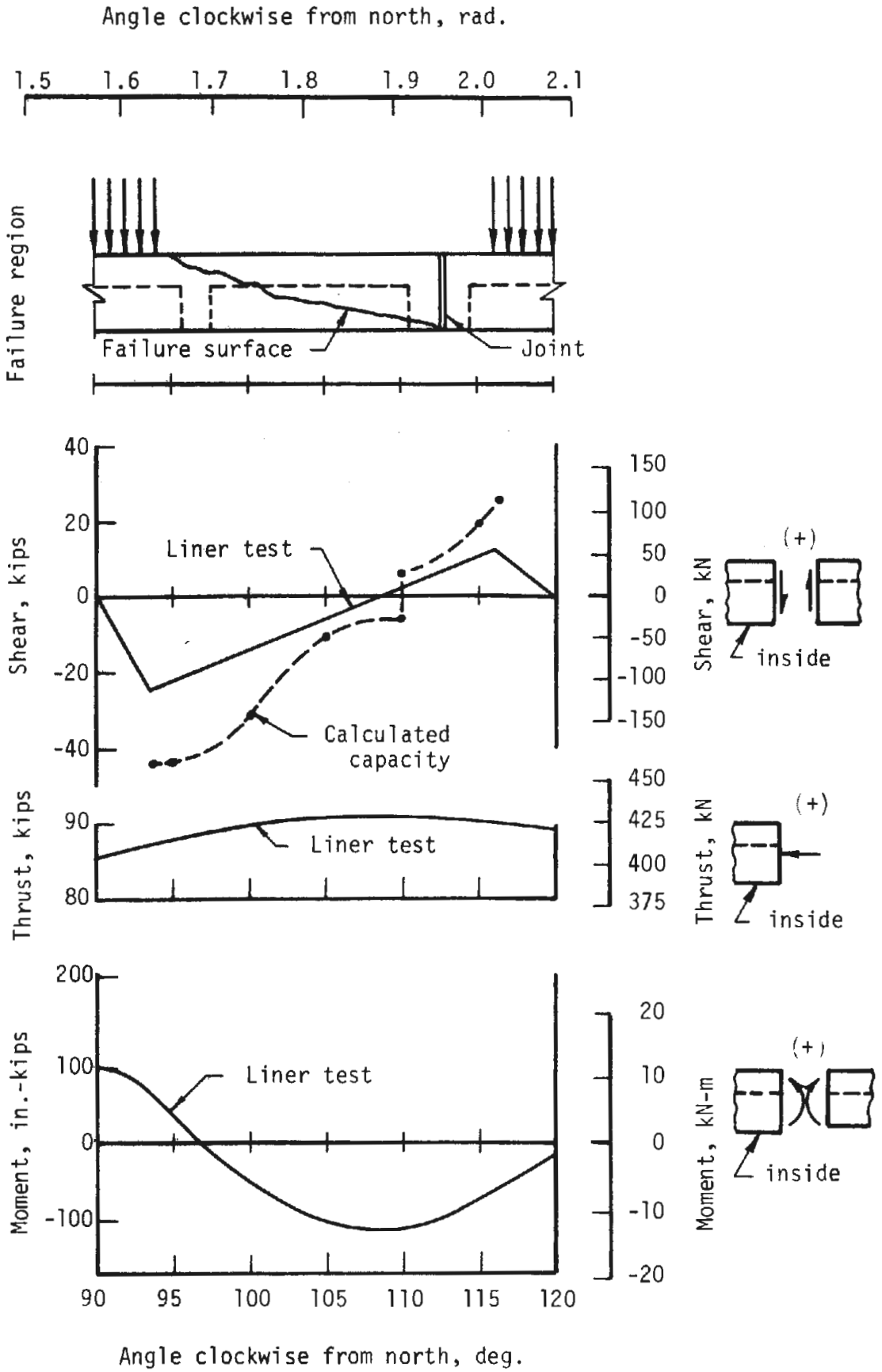

FIGURE 4.24 SHEAR, THRUST AND MOMENT FOR THE FAILURE REGION AT MAXIMUM LOAD IN TEST S2

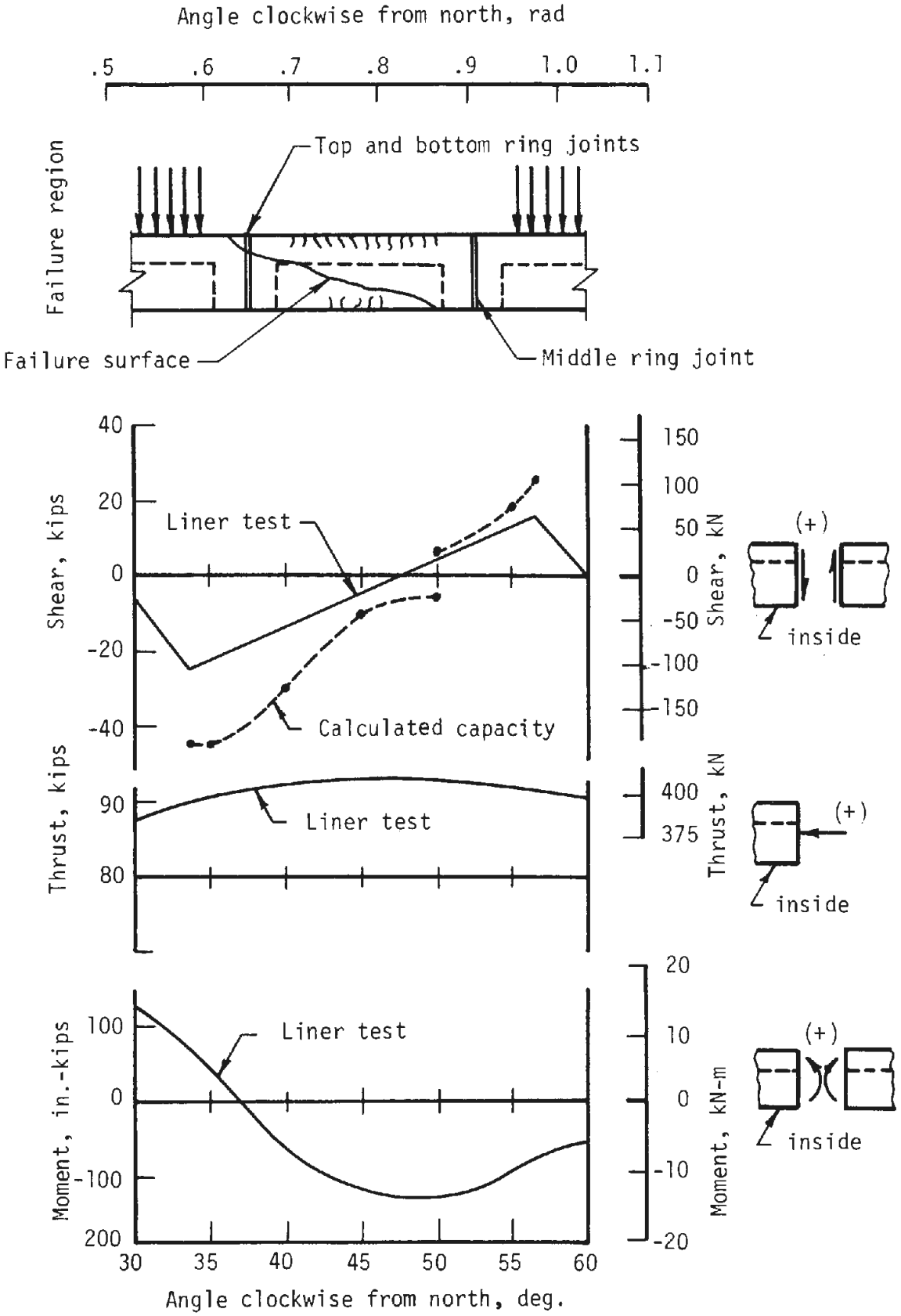

FIGURE 4.25 SHEAR, THRUST, AND MOMENT FOR THE FAILURE REGION AT MAXIMUM LOAD IN TEST S3

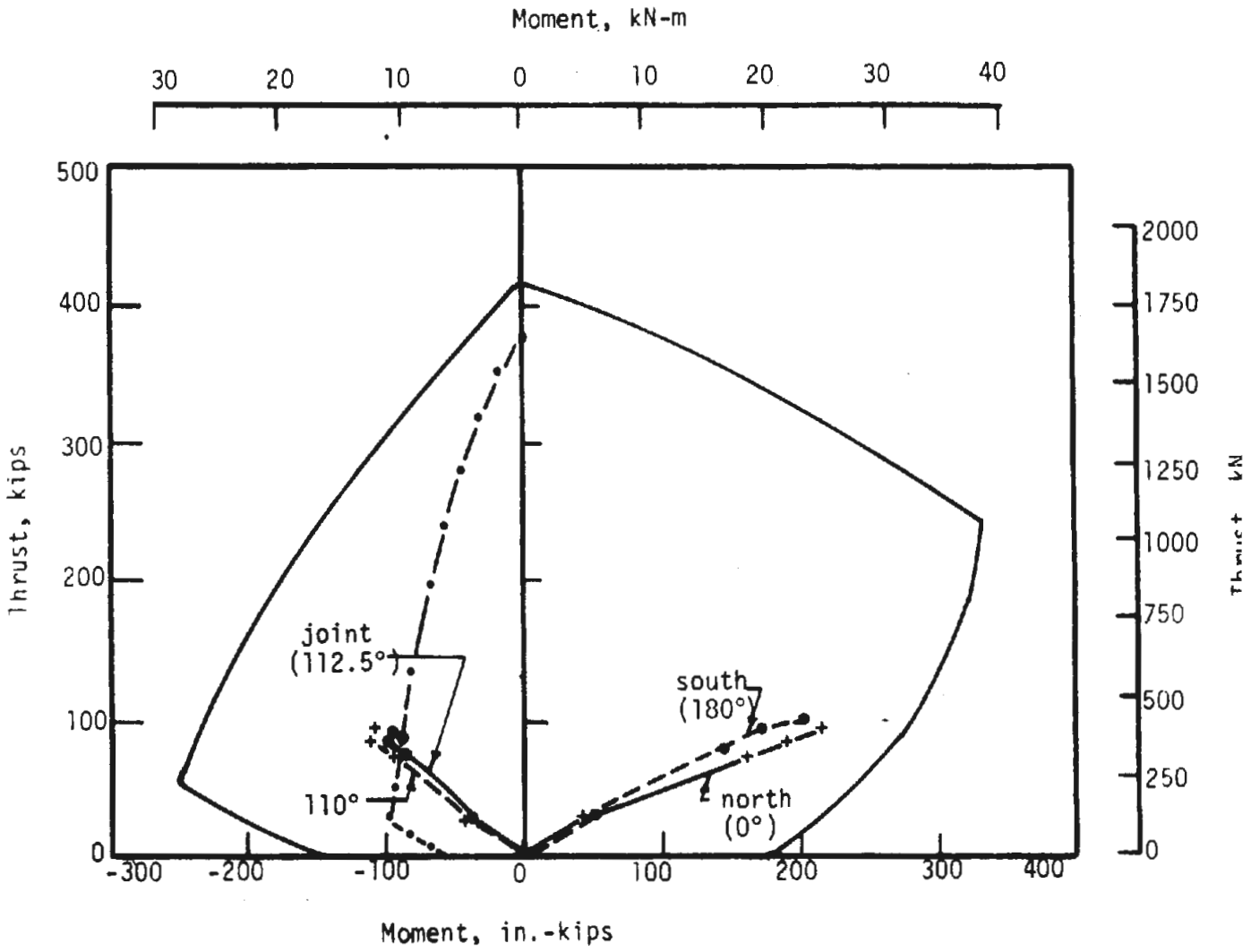

FIGURE 4.26 THRUST-MOMENT COMPARISON FOR CRITICAL SECTION IN TEST S2

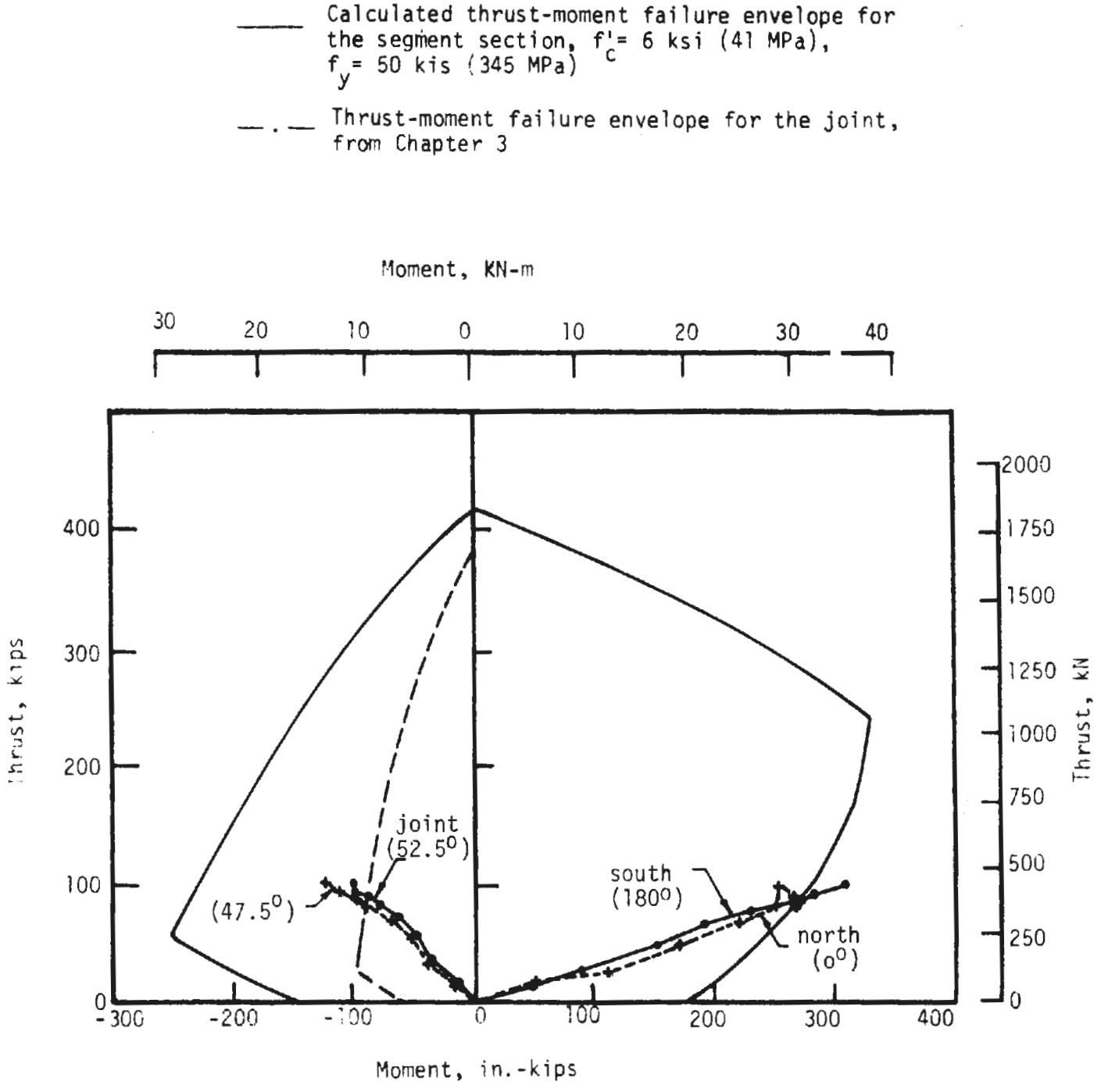

FIGURE 4.27 THRUST-MOMENT COMPARISON FOR CRITICAL SECTION IN TEST S3

moment and thrust along the failure region for the last load increment on the moment-thrust path curves of Figs. 4.26 and 4.27.

The peak measured active loads, diameter changes at peak load and calculated average stiffnesses are summarized for all three tests in Table 4.2.

Opening of the mating surfaces on the inside of the joints 172.5 and 352.5 degrees (3.0 and 6.15 rad) measured clockwise from north in the middle ring of test S3 were monitored with a two-inch-gage-length Whittemore gage. Measurements were made at the middle of the joint and one inch (25 mm) from each end using metal tabs which were glued to the concrete, as gage points. The same technique was used in the joint tests described in Chapter 3. Similar measurements were made in tests S1 and S2, but those in S3 are representative of the results.

When a joint is subjected to moment and thrust, the thrust causes the mating surfaces to close while the moment causes them to close on one side and open on the other. Therefore, joint behavior is a function of both moment and thrust. If the ratio of moment to thrust remains constant, the behavior can be shown as a function of moment, but if it does not, there is no clear way to show the complete relationship. If the thrust is larger at a given moment in two comparable joints, then the joint opening will be smaller.

In Figs. 4.28 and 4.29 the inside joint opening is shown as a function of moment and as a function of thrust at the section. Comparison of these results with comparable values for the joints in Chapter 3 demonstrate the influence of the adjacent segments on the opening of the joint.

TABLE 4.2

SUMMARY OF TEST RESULTS

Test Specimen	Loads at increment prior to failure		Diameter change at increment prior to failure		Test average of medium-liner stiffness (active)	Test averages of medium stiffnesses (passive)
	Active[2] P_{N-S}, kips (kN)	Passive P_B, kips (kN)	Active ΔD_{N-S}, in. (mm)	Passive ΔD_{E-W}, in. (mm)	$P_{avg}/(\Delta D_{N-S})$, k/in (kN/cm)	$(P/(\Delta D/2))_{A,B,C}$, k/in (kN/mm)
S1	47.0 (209.1)	55.36 (246.25)	1.128 (28.65)	0.713 (18.11)	42.87 (75.08)	170(29.8) 161(28.2) 169(29.6)
S2	50.8 (226.0)	58.93 (262.13)	1.206 (30.63)	0.723 (18.36)	42.85 (75.04)	170(29.8) 167(29.2) 184(32.2)
S3[1]	55.0 (244.7)	64.00 (284.69)	1.283 (32.59)	0.845 (21.46)	44.78 (78.42)	160(28.0) 155(27.2) 164(28.7)

[1]All loads are expressed for an equivalent 2ft (610 mm) - long liner; i.e., the sum of the radial loads at a particular location are divided by 3.

[2]Values of P_{N-S} at failure for tests S1, S2, and S3 were recorded as 50.40 kips (224.2 kN), 51.90 kips (230.9 kN), and 55.50 kips (246.9 kN), respectively.

[3]From Figures 4.11 to 4.13.

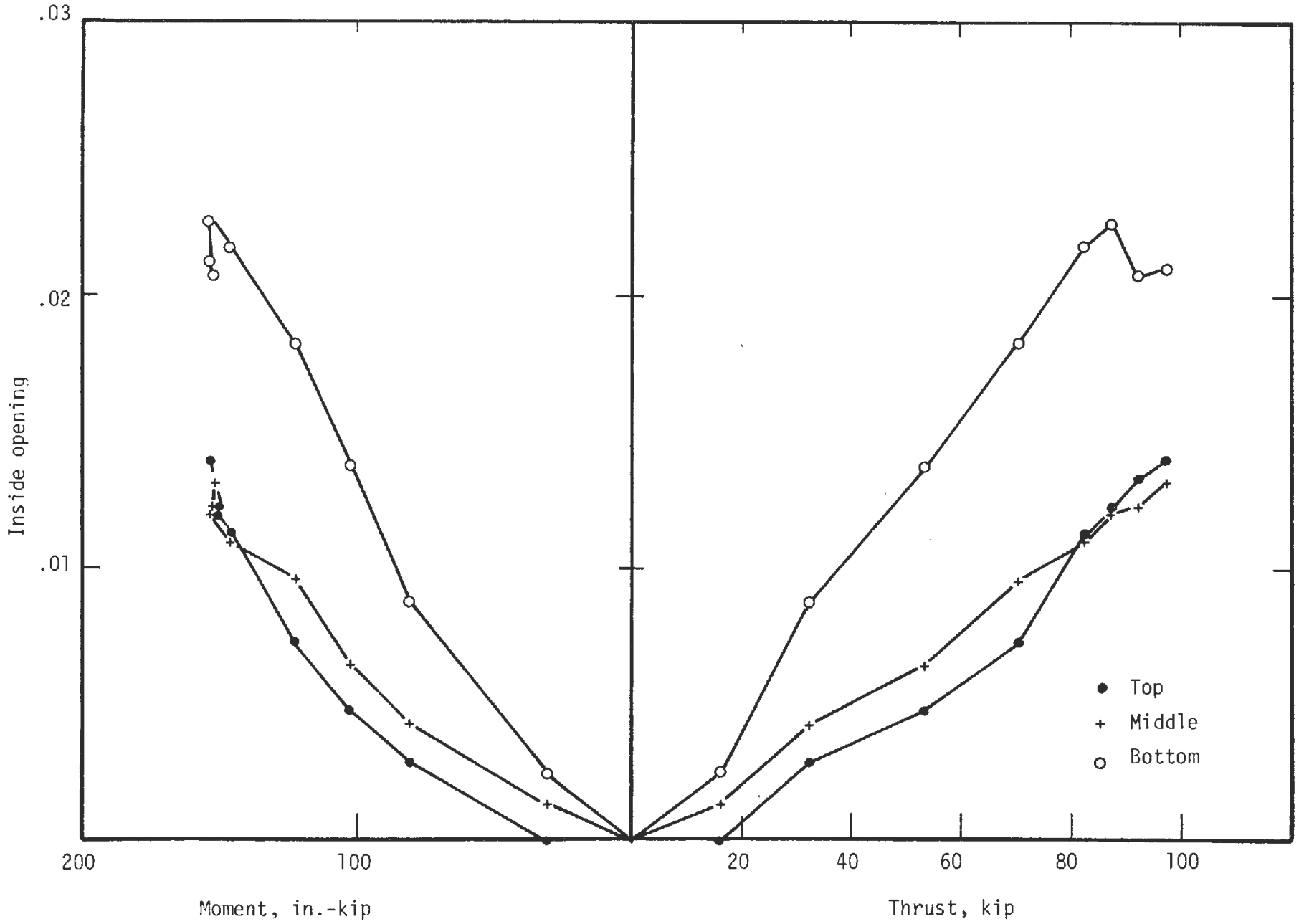

FIGURE 4.28 MOMENT-THRUST-OPENING FOR TEST S3
AT 172.5 DEGREES

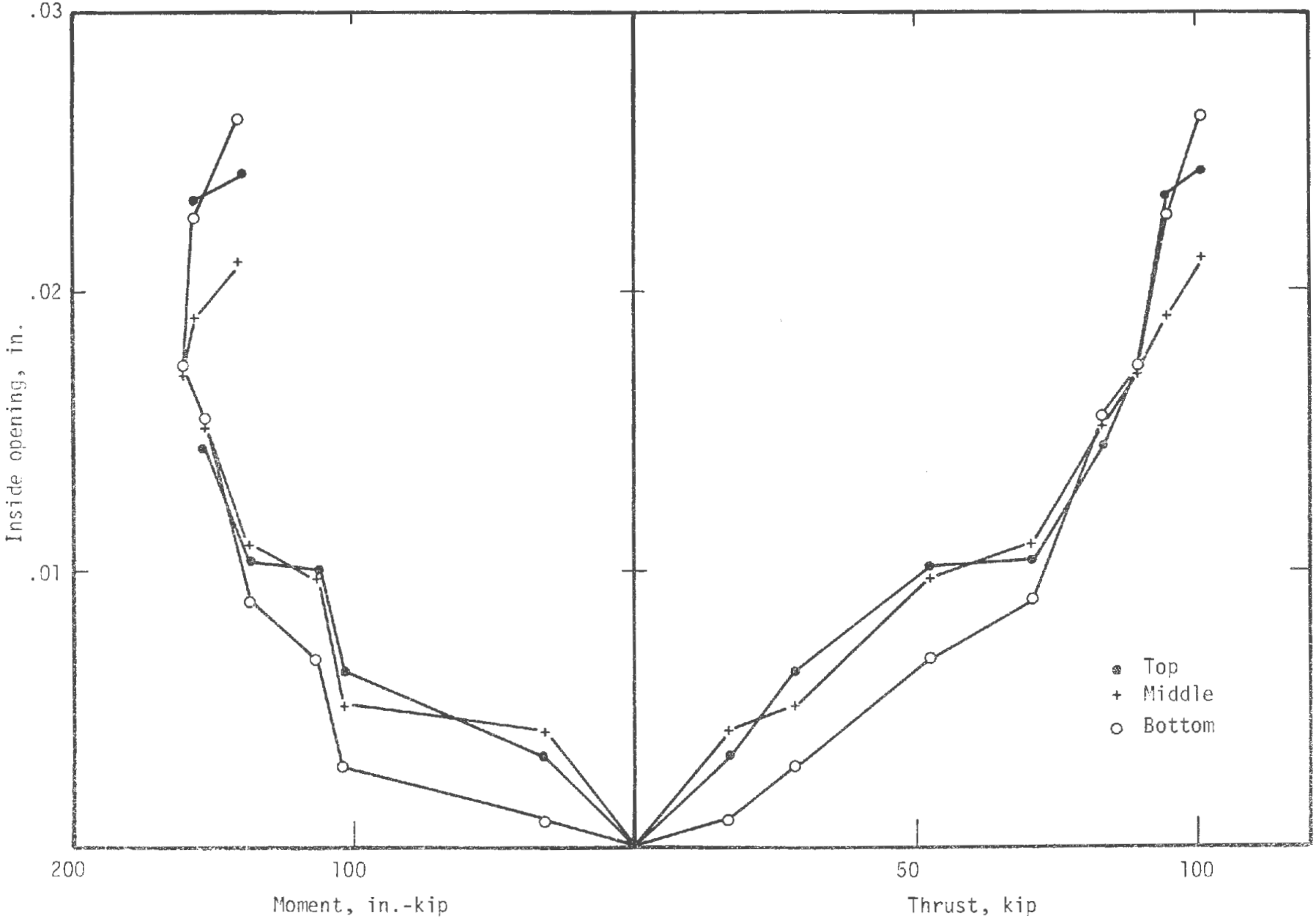

FIGURE 4.29 MOMENT-THRUST-OPENING FOR TEST S3
AT 352.5 DEGREES

In the joint tests, the opening was always largest at the joint ends and small at the center between the bolts. In Fig. 4.28, the opening is larger at the bottom of the joint, while it is about the same magnitude at the middle and top. In Fig. 4.29, the pattern changes with the bottom of the joint showing the smallest opening while the middle and top were about the same. One possible explanation for this may be that the restraint provided by adjacent rings caused less opening at the ends of the joint than occurred in the single joint tests.

Efforts to correlate the relative amounts of joint opening with the proximity of joints in the adjacent rings did not show consistent results. For the joint of Fig. 4.28, the bottom of the joint is 14 degrees (0.24 rad) from a joint in the bottom ring (Fig. 4.10). This might reduce the effectiveness of the bottom ring in preventing the bottom of the joint to open. However, for the joint of Fig. 4.29, the top of the joint was 14 degrees (0.24 rad) from a joint in the top ring, but the pattern does not hold. Thus, it is probably more reasonable to attribute the differences in joint opening to random fit between the rings.

Joint opening-moment curves with positive eccentricity, so the joint opens on the inside, are shown in Fig. 3.6 for the joint tests, J-1 and J-2. For test J-1, the initial eccentricity was 2.66 in. (67.6 mm) while that obtained for the curves in Figs. 4.28 and 4.29 are smaller. The range in computed eccentricity is 1.5 to 2.1 in. (38 and 53 mm) for Fig. 4.28 and between 1.4 and 2.1 in. (35 and 53 mm) for Fig. 4.29. Thus, the joint opening at a given moment should be less in the liner test and this is the case. Also, the curves show the same general shape in the

joint tests and liner tests. At the highest load increment the eccentricity was 1.6 in. (41 mm) in Fig. 4.28 and 1.4 in. in Fig. 4.29, so the maximum moment should be larger and this is also the case. For the joint of Fig. 4.28 the maximum moment is 152 in.-kips (17.2 kN•m) and that for Fig. 4.29 is 160 in.-kips (18.1 kN•m). The curves in Fig. 3.6 are quite ductile, indicating that the joints in the liner could have taken considerably more deformation before failure.

Rotation of the joint was measured at the section 112.5 degrees (1.96 rad) clockwise from north in the middle ring. Holes were drilled at each junction of the webs and the end diaphragm of the segment through the shell. Bolts through these holes clamped bars to both sides of the segment, perpendicular to the shell. Dial gages were attached to these perpendicular bars which were 3 in. on each side of the joint mating surfaces to measure the rotation of the joint. This device was similar to that used for the joint tests shown in Fig. 3.4 except that the horizontal bars in that figure were not through the segment shell.

The resulting moment-rotation curve is shown in Fig. 4.30 where the moment is negative (compression on the inside of the liner). The relationship is nearly linear to a moment of 95 in.-kips (10.7 kN•m) and a thrust of 100 kips (445 kN). The ratio of moment to thrust remained fairly constant throughout the test giving an eccentricity of slightly less than one in. (25 mm); for the last 4 load increments it varied from 0.86 to 0.95 in. (22 to 24 mm). A stiffness of the joint can be calculated, from the average straight line through the points, to be 28,600 in.-kips/rad, (3230 kN•m/rad).

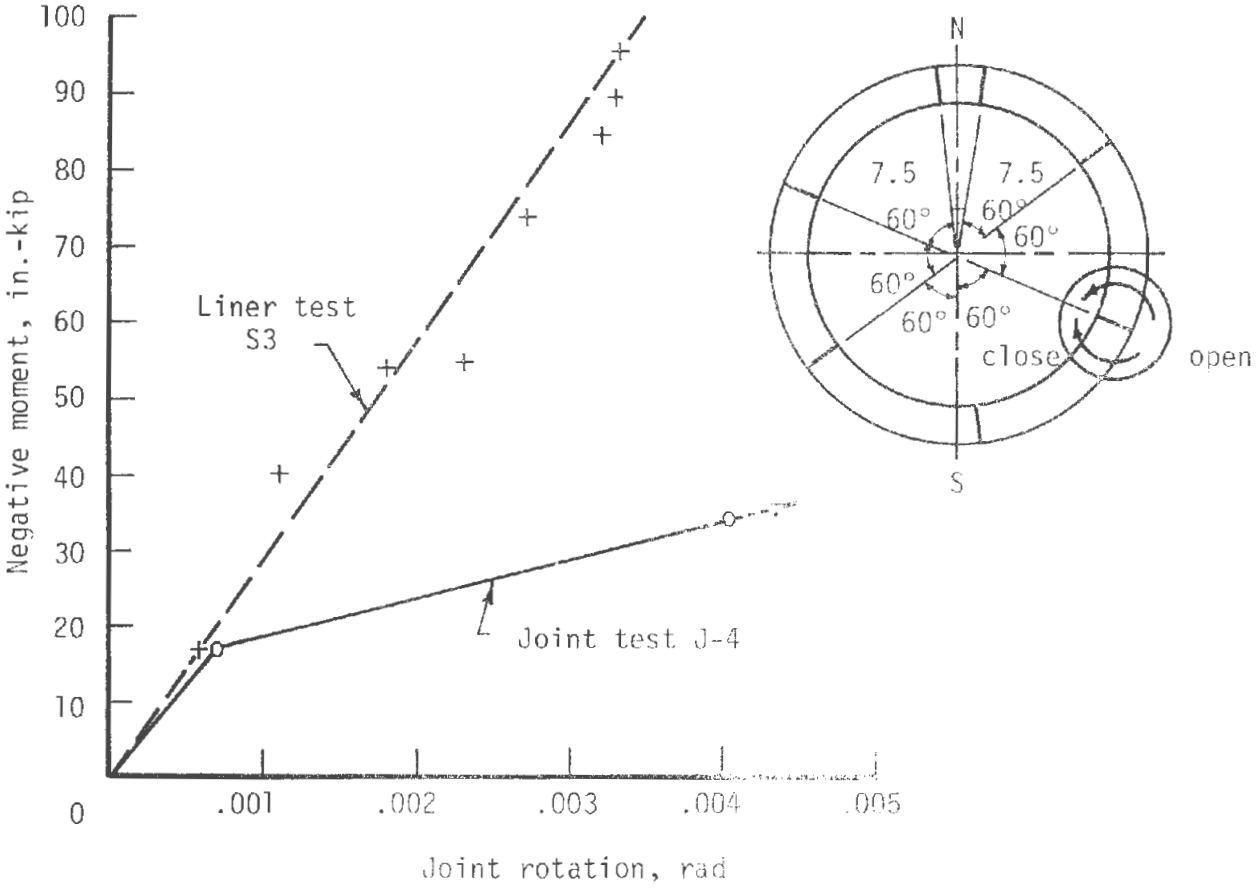

FIGURE 4.30 MOMENT-JOINT ROTATION IN MIDDLE RING OF TEST S3

Joint rotation-moment curves for isolated joints subjected to negative moment are shown in Fig. 3.12, for tests J-4 and J-5. The eccentricities in these tests were larger than for the ring test joint of Fig. 4.30. The initial part of the curve for joint test J-4 is shown in Fig. 4.30 and indicates that for the first load increment the stiffnesses were

the same, but for higher moments the deformation was much larger for the joint test. This could be the result of the larger eccentricity in the joint test or the help of the adjacent segments in the liner test in reducing the joint rotation.

4.5 DISCUSSION

One objective of the tests on large-scale segmented liners was to determine if the tie bars and shear reinforcement can be replaced by randomly oriented steel fibers. It appears that failure in these tests may have been precipitated by inward buckling of the inside longitudinal bars at the end of the segment and therefore the load on the liner might have been higher if these bars had been encircled by tie bars. From this point of view the increased tensile strength of the steel-fiber-reinforced concrete was not sufficient to replace conventional tie bars. However, the details of the bends of the bars at the segment end also contributed to the problem, so it may be possible to overcome the tendency for the bar to buckle inward by improving the bar details or by placing a tie bar at the segment end which will resist this inward force. The natural direction of the radial force in these bars is outward, or into the segment, so there is no reason to expect them to fail as they did if it were not for the end detail.

The shear equation (Eq. 2.8) in Chapter 2 for steel-fiber-reinforced members may be used for comparison of the shear capacity with the actual shear at the failure section. That equation represents failure conditions and was derived by assuming that the shear capacity of the concrete, V_c, on the

left side of the equation was reached at the same load that the design shear, V_u, and moment, M_u, occurred on the right side. The original derivation of the equation for conventional reinforced concrete beams was based on tests of simple beams in which the ratio M/Vd was given by the geometric quantity a/d. In this case "a" was the distance from the critical failure section in shear to the support where moment was zero. Also the shear was constant in this region. If the shear is assumed constant and equal to the value at the section being checked, then M/V approximately takes on the meaning of the distance from the section being checked to the inflection point. This is not strictly true; for curved members with thrust, the moment and shear are related just as they are for straight beams, except for the component of moment resulting from the thrust reacting with the resulting curvature of the member between loads. If the loads are close together or distributed, this difference is minor.

It is reasonable to use the value of the Vd/M ratio determined from tests at a particular section in the tunnel liner on the right side of the shear equation to calculate the shear capacity of that section. This calculated capacity can then be compared with the shear that existed at the section in order to determine if the segment section was near failure in shear. This was done for the region between 90 and 115 degrees for specimen S2 as shown in Fig. 4.24 and 34 and 55 degrees for specimen S3 as shown in Fig. 4.25, for the middle ring. The data used, and the resulting calculated capacities are shown below for specimen S3.
The calculated capacities are also shown on the shear plot in Fig. 4.25. In using Eq. 2.8, the flange thickness, h_f, was taken equal to zero when moment

Section degs	(rad)	Test values for S3: Shear kips	(kN)	Moment in.-kips	(kN·m)	Thrust kips	(kN)	Calculated shear capacity kips	(kN)
34	(.59)	-24.1	(107)	66.9	(7.6)	99.8	(444)	45.0	(200)
35	(.61)	-22.0	(98)	37.6	(4.2)	100.3	(446)	45.0	(200)
40	(.70)	-13.2	(59)	-61.4	(6.9)	101.8	(453)	29.7	(132)
45	(.79)	-4.3	(19)	-115.7	(13.1)	102.6	(456)	10.1	(45)
50	(.87)	+4.6	(20)	-124.6	(14.1)	102.6	(456)	10.1	(45)
55	(.96)	+13.5	(60)	-88.0	(9.9)	101.8	(453)	24.1	(107)
56	(.98)	+15.7	(70)	-72.7	(8.2)	101.5	(451)	31.4	(140)

was zero or negative. Also the value of effective depth, d, changed when the moment changed sign. When moment was zero (or very low) the calculated shear capacity became very large, but it is recognized that there must be an upper limit. For the points at 34 and 35 degs (0.59 and 0.61 rad) the limit was taken as $7.5\ M/(b_w d + 2h_f^2)\ f_r = 6.5$. This limit approximately represents the upper bound of the test data in Fig. 2.12.

This comparison indicates that the computed shear capacity is always larger than the shear that occurred. The capacity curve is closest to the actual shear diagram near 50 deg (0.79 rad) where the capacity is about twice the actual shear. The approximate nature of the equation must be recognized because of the limited data on which it is based. It can be concluded that the failure was not entirely due to shear unless the shear capacity was severely reduced by the splitting along the compression reinforcing bar near the joint.

Comparison of calculated and actual shear for test S2 was obtained from a similar calculation and is shown in Fig. 4.24. The same conclusion is reached from this comparison both in terms of failure in the test and shear capacity predictions.

Further insight into the mechanism of liner failure may be gained from the moment-thrust paths in Figs. 4.26 and 4.27. Figures 4.24 and 4.25 show that the moment and shear vary drastically within the failure region, so care must be exercised in the sections used in a comparison. The end of the moment-thrust paths for the failure region (negative moment) in both specimens lie outside the failure envelope for the joint tests, and well inside that for the section. If the joint in the liner behaves like that in the joint tests, then failure is indicated in the joint region. The joints in the liner test must be stronger than those in the joint tests because the paths end outside the envelope for the joint tests. It appears that failure may have been precipitated at the joint and then traveled into the segments as indicated earlier. The joints were similar for the segments in the liner tests and the joint tests, but there were 2 minor differences that would tend to increase the joint strength. The bolt holes in the segments were 1-1/8 in. (28.6 mm) OD and 1-1/2 in. (38.1 mm) OD in the joint tests. Also in the segments a reinforcing bar was added to the end diaphragm that was near the inside surface and parallel to the inner corner (Figs. 3.1 and 4.2).

Thrust-moment paths for the north and south sections are also shown in Figs. 4.26 and 4.27 (positive moment) and indicate for specimen

S2 that these sections were not near failure. However, failure is indicated in Fig. 4.27 for specimen S3 because the path ends outside the theoretical envelope. In test S3 a diagonal crack was noted at the north sections near the end of the test (Fig. 4.22) indicating that that section was indeed approaching failure. Again the envelope shown does not correctly represent the true envelope for this particular section and the correct one must lie to the right so that it will enclose the entire thrust-moment path curve.

Behavior of the segmented liner before failure is of interest in order to evaluate its working load response and its interaction with the ground. The effect of joint lap in the three ring liner may be seen in Fig. 4.31 where the stiffness of the three ring liner, S3, is compared with that of the one ring specimens, S1 and S2. In this case stiffness is defined as the average active load, P, divided by the diameter change, ΔD, in the active load direction (north-south direction). The stiffness of the three ring liner is converted to stiffness per ring for comparison and it is only slightly stiffer than the single ring specimens. As discussed earlier the average passive force stiffnesses were not exactly the same, but S1 and S3 were within 4.3 percent as shown in the table below.

Test	Average passive stiffness/ring, k/in. (kN/mm)	Variation from average, percent	Liner stiffness/ring, k/in. (kN/mm)
S1	167 (29.2)	5	42.9 (7.51)
S2	173 (30.3)	10	42.9 (7.51)
S3	160 (28.0)	6	44.8 (7.84)

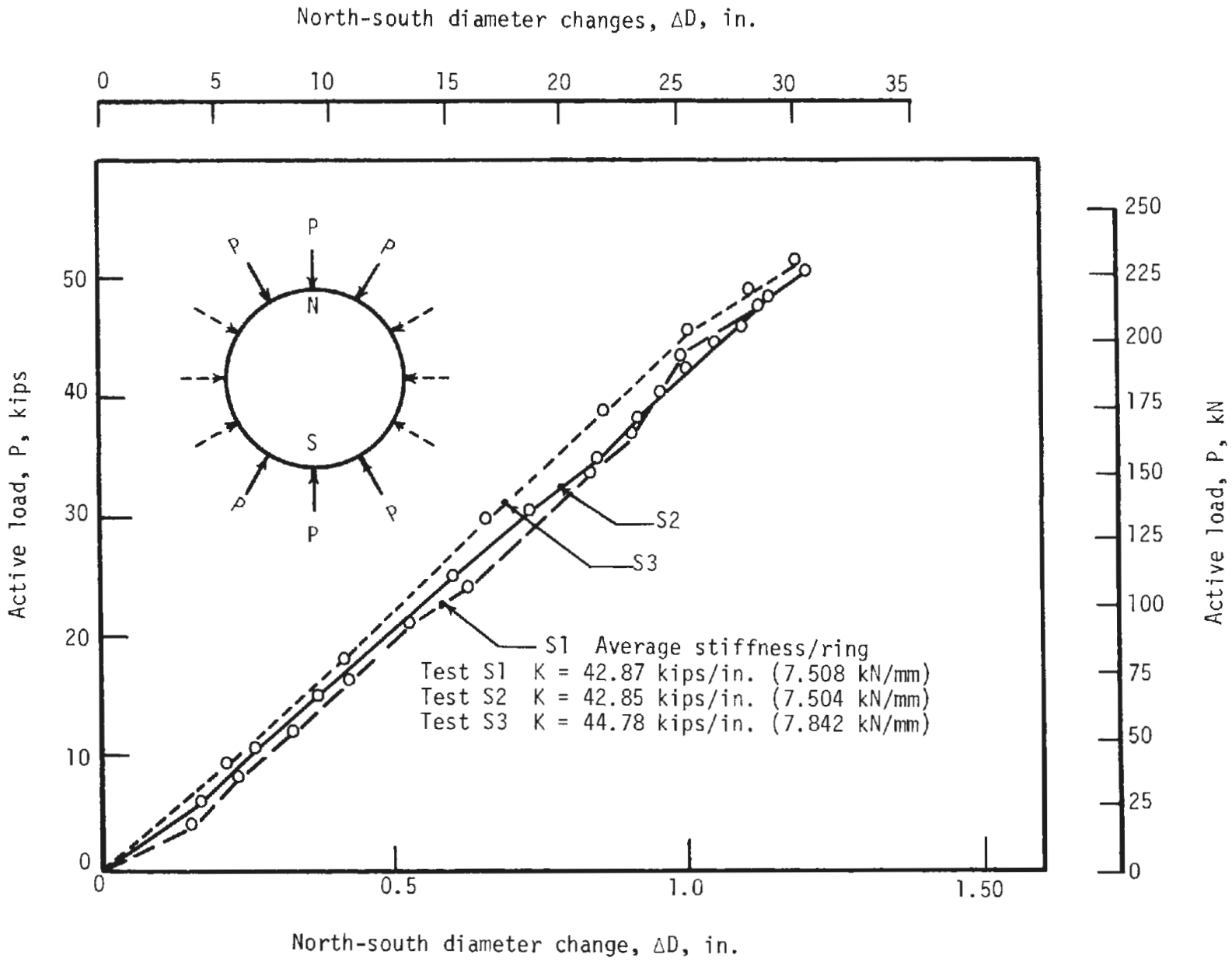

FIGURE 4.31 COMPARISON OF LINER STIFFNESS FOR THE THREE SEGMENTED LINER TESTS

A small difference in average stiffness of the passive forces does not appear to affect the liner stiffness greatly as shown by comparing tests S1 and S2 in the table, where the liner stiffness is the same, while the average passive force stiffnesses were different by 3.5 percent. The conclusion that may be drawn is that the interaction between rings with lapped joints did not change the liner stiffness more than about 4 percent in these tests. A larger stiffness might be expected in the 3-ring case because staggering of the joints would allow adjacent segments to reinforce the joints.

Reinforcement of joints by adjacent segments would be small if the rings were so poorly held together that they acted independently, like three separate rings. The circumferential joint was grouted so the contact between the rings was good, but the pressure mobilized by the bolts between them was relatively small. From Fig. 3.10 the bolt force with 150 ft-lb (203 N-m) of torque is about 9.5 kips (42 kN). There are 24 bolts in a circumferential joint, providing an area of mating surface per bolt of 75 $in.^2$ (0.048 m^2). The corresponding pressure between rings on the mating surface is only 0.13 ksi (0.90 MPa). This pressure may not be sufficient to mobilize enough friction force to make the rings act together.

Analysis of the liner is often based on uniform properties of the liner around its circumference so the abrupt change in section near the joints and at the longitudinal ribs are distributed throughout the section. Response of the liner was almost perfectly linear to failure so it is reasonable to use a linear analysis to predict the response. A linear STRUDL analysis was used to obtain the curve in Fig. 4.32 where the ratio $P/\Delta D$ in

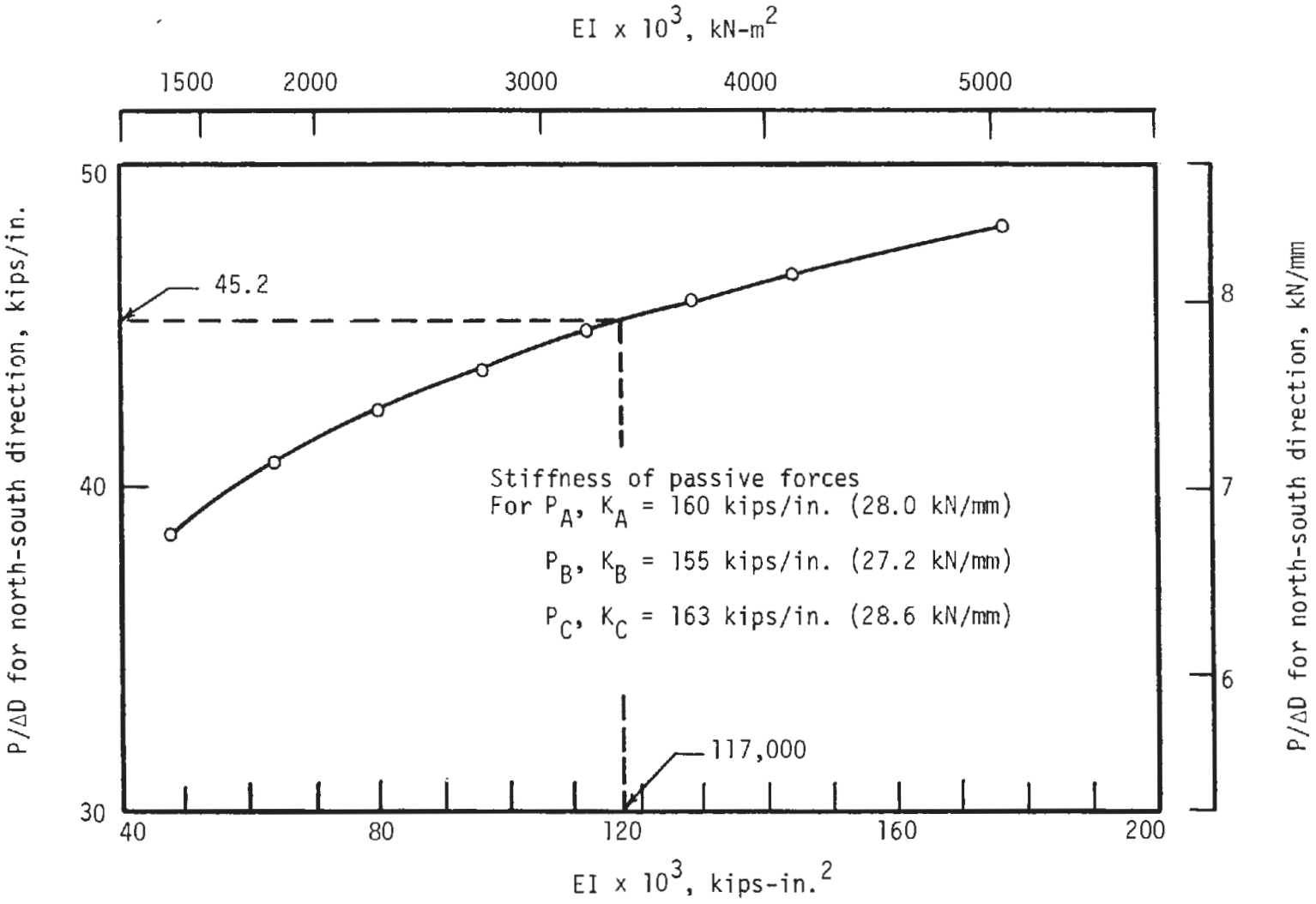

FIGURE 4.32 LINER STIFFNESS - SECTION STIFFNESS FROM A LINEAR ANALYSIS FOR TEST S3

the north-south direction is plotted as a function of section stiffness EI for the liner. One ring of liner was modeled by straight beam elements at 10 deg (0.174 rad) increments with the joints lying on the circle representing the center of gravity of the segment. Symmetry of load was assumed, but the actual passive force stiffness shown by Fig. 4.13 for test S3 were used. If the S3 test value of $P/\Delta D$ in the north-south direction of 45.2 kips/in. (7.91 kN/mm) is used to obtain the corresponding EI, a value of 117,000 k-in.^{2} (336 kN-m^2) results. The average E for the concrete in specimen S3 was 3310 ksi (22.8 GPa), so the corresponding moment of inertia, I, is 35.3 in.^{4} (14.7 x 10^6mm^4). This value is low compared with the calculated values of 113 in.^{4} (47.0 x 10^6 mm^4) for the uncracked gross moment of inertia and 161 in.^{4} (67.0 x 10^6 mm^4) for that of the uncracked transformed section for the segment section. It is much closer to the properties of the cracked section as shown in the table below.

Basis for calculation of I	Calculated I, in.^{4}	mm^4 x 10^6
Uncracked gross I	113	47.0
Uncracked tranformed I	161	67.0
Fully cracked I for positive moment	81	33.7
Fully cracked I for negative moment	45	18.7

The equivalent I is also influenced by rotation at the joints

and the extent of this influence can be seen if some reasonable computation of equivalent I is made for a joint. In Fig. 3.12, where moment-rotation curves for the joint tests are shown, an average slope of the curve for test J-1 is 10,000 in.-kip/rad (1,130 m-kN/rad) with positive moment applied. Assume that this rotation occurs over the 12 in. (152 mm) length of liner at the joint between the rotation measuring bars and that E is about 5100 ksi (740 MPa), the value for the joint test specimen. An average equivalent I for the joint of 24 in.^{4} (10.0 x 10^6 mm^4) is computed, which is below the equivalent I for the liner. The same type of computation can be performed for the moment joint rotation measured in test S3 and shown in Fig. 4.30 where the moment is negative. The average stiffness of the joint is about 28,600 in.-kips/rad (3230 kN-m/rad), and the equivalent I is calculated to be 52 in.^{4} (21.6 x 10^6 mm^4), if E is considered 3310 ksi (22.8 GPa) and the distance between measuring arms was 6 in. (152 mm). Thus, the joint rotations influenced the liner deformation and the equivalent moment of inertia.

CHAPTER 5

SUMMARY AND CONCLUSIONS

The tests described had two objectives; the first was to examine the use of randomly oriented steel fiber in the concrete mix as a substitute for shear reinforcement and tie bars, and the second was to study the behavior of segmented liners under controlled loading conditions. All tests were performed on specimens cast with steel-fiber-reinforced concrete. These studies were a preliminary effort in a continuing program concerning segmented concrete liners. Additional analyses and tests are planned.

The series of beam tests that were designed to have shear failures provided a set of data points that were used to modify the ACI formula for allowable shear stress in concrete beams, to account for steel fiber reinforcement. This formula is useful for predicting shear capacity of tunnel liners made of steel-fiber-reinforced concrete, but requires modification for section shape when waffled sections are used, and for the thrust that occurs in tunnel liners. Strictly empirical modifications for these factors were suggested that were drawn from the literature for conventionally reinforced concrete members.

The shear capacity formula thus modified was used to compare the actual shear in the failure section of the test liners with the calculated capacity. It was found that the capacity exceeded the shear present and it was concluded that the liner failures were not primary shear failures.

Additional tests are needed to resolve two questions that remain with regard to the shear capacity of steel-fiber-reinforced members. In the shear beam test series the $\rho_w V_u d/M_u$ ratio was not reached for which shear strength no longer varied with this ratio (Fig. 2.12). A few additional tests in the upper range of the ratio would provide the upper limit on shear capacity attributable to the concrete in the beam. Beam tests provide the effect of moment on shear capacity, but the influence of axial thrust and the combination of moment and thrust remain unresolved for steel-fiber concrete. Tests that would give the shear capacity of a given section with varying thrust in the range that normally occurs in tunnel liners, would help to resolve this question. The problem is somewhat different from that occurring in most structural members because the thrust is relatively high in tunnel liners.

The series of joint tests provide information about the joint behavior when isolated from the liner. The joints and the segments used in the liner tests were scaled geometrically in an approximate manner from that reported by Gamble (1967). During the joint tests, it was clear that the joint design would be the weak part of the liner, but the liner segments were being cast at the same time in order to maintain the testing schedule and it was not possible to change the joint details. The failures in the liner tests involved the joints and were similar to those that occurred in the joint tests. The crack patterns in the joints were also similar to those that were reported for the tests performed by the Bechtel Corp. (1966). These tests are also the ones reported by Gamble (1967).

The joint failure mechanism was determined for various eccentricities of load. The location of additional reinforcement to strengthen the joint then becomes clear. Also, with a knowledge of the modes of failure, it is possible to devise computational procedures to predict the capacity corresponding to that failure mode. This was done for the tests and the computational results were compared with the test results. Success of the computations in predicting the failure loads varied with the failure mode. These procedures are not as accurate as those used for computing segment section behavior, and a larger safety factor for joints than for the segment is desirable.

The segmented tunnel liner load-deflection curves were nearly linear to failure, as were the moment-thrust curves for various sections. Therefore, a linear analysis can reasonably be used to predict the overall behavior. The STRUDL analysis was used to match the load-deflection response of test S3 and it was found that the uniform equivalent moment of inertia required to obtain the same load-deflection curve was 22 percent of the uncracked transformed moment of inertia, and 44 and 78 percent of the positive and negative fully cracked moments of inertia, respectively. If a weighted average of the ribbed section of the segment and the diaphragms in the segments had been used for comparison, the percentages would be even smaller. This comparison shows that the joints influenced the deformation a great deal. It was shown that the equivalent moment of inertia for a joint was relatively low and depended on the direction of the applied moment.

There was little interaction between rings in the three-ring liner test, as shown by comparing the overall stiffness in the three-ring test with that of a single ring. The stress between the rings along the circumferential joints that results from the circumferential bolts is relatively low. Also, the bolts are considerably smaller than the bolt holes, so slip can occur in the circumferential joint. This probably accounts for the lack of interaction between rings, and in this respect may not be representative of field conditions because the shoving forces of a shield would press the segments together more tightly along the circumferential joint. It is not clear how much of the shoving force remains in the liner when the shield is well past, and there is little information available on the subject.

Both of the single-ring tests failed at the same location in the same way. In all three tests, failure occurred in a region of negative moment and was near a joint. In one of the single-ring tests and in the three-ring test, circumferential cracks were observed prior to failure on the top of the specimen, eminating from the radial joint surface. Thus, a splitting failure along the inside circumferential bars was indicated. Photographs of the failure region (Figs. 4.18 and 4.21) show these bars buckled inward. The drawings of the bar details (Fig. 4.2) show that these bars are curved in the joint, so compression in them would cause an inward force. This force precipitated splitting, and with the bar buckled and the concrete spalled off the inner surface, failure progressed through the section.

A tie bar could have prevented or delayed the failure, so the steel fiber in the mix did not successfully replace the tie bar. This

problem could be overcome by changing the bar detail in the joint or by placing tie bars only at the ends.

The liners from which the test specimens were approximately scaled, were required to accommodate a diameter change of 1 in. (25 mm) in the active load direction before failure to be favorably evaluated. This deflection corresponds to $\Delta D/D$ of 0.0048. For the 10 ft (3 m) OD test specimen this ratio corresponds to a diameter change ΔD = 0.56 in. (14 mm). The specimen S3 had this deflection at about 46 percent of its peak load. Thus, the test liner had adequate deformability. The ratio $\Delta D/D$ = 0.005 has been suggested as the specified deformation for obtaining design moments. The test liner at this deformation had about one-half its ultimate load, and had very little distress as there were no significant cracks observed at this load level.

The liners from which the test specimens were scaled were designed for a working compressive stress in concrete of 0.45 f'_c at the crownline. Using this as a design value, it is possible to determine design thrusts and moments for the liners described in this report. Using the fully cracked section properties with the ratio of moment to thrust obtained from the test S3 at the crown results in a design thrust of 34 kips (152 kN) and a design moment of 105 in.-kips (12 kN•m) for liner S3. The ultimate thrust and moment this liner withstood at the crown was 100 kips (444.8 kN) and 307 in.-kips (34.6 kN•m), respectively, or a factor of about 3 above the design values.

Major findings from this preliminary investigation into segmented liners may be summarized briefly as follows:

1) Steel fiber in concrete sections increases their shear resistance and with proper attention to reinforcing bar details may replace shear

reinforcement and tie bars in segmented liners. Shear forces on a section in the ground are generally less than thsoe occurring in the liner tests described so those tests represent a severe shear loading.

2) Modes of failure of radial joints in segments of a particular design was demonstrated. A reasonable procedure for determining the strength of a joint can be formulated once the mode of failure is determined.

3) Joints reduced the liner stiffness in the full ring tests described. The joints also determined the strength of the liners, though it is believed that joints can be designed to develop the strength of the segment section. There was little interaction between rings in the three-ring test because the circumferential joint could not transfer sufficient force between rings.

REFERENCES

ACI-ASCE Committee 326 (1962). "Shear and Diagonal Tension, Part 2," Journal of the American Concrete Institute, Vol. 59, No. 2, February, pp. 277-333.

ACI-ASCE Task Committee 426 on Shear and Diagonal Tension (1973). "The Shear Strength of Reinforced Concrete Members," Journal of the Structural Division, ASCE, Vol. 99, No. ST6, June, pp. 1091-1187.

Batson, G., Jenkins, E., Spatney, R. (1972). "Steel Fibers as Shear Reinforcement in Beams," Journal of the American Concrete Institute, Vol. 69, No. 10, October, pp. 640-644.

Bechtel Corporation (1966). "Precast Concrete Tunnel Liners," by Bechtel Corporation, San Francisco, for San Francisco Bay Area Rapid Transit District, February.

BRE News (1974). "GRC Makes Good," Department of the Environment, Building Research Establishment, Scottish Laboratory, Kelvin Road, East Kilbride, Summer.

Bresler, B. and MacGregor, J. G. (1967). "Review of Concrete Beams Failing in Shear," Journal of the Structural Division, ASCE, Vol. 93, No. ST1, Proc. Paper 5106, February, pp. 343-372.

Building Code Requirements for Reinforced Concrete (1971). ACI Standard 318-71, American Concrete Institute, Redford Station, Detroit, Michigan.

Gamble, W. L. (1967). "Structural Behavior of Precast Concrete Tunnel Liners," ACI Journal, Proceedings, Vol. 64, No. 1, January, pp. 1-11.

Ghaboussi, J. and Ranken, R. (1974). "Tunnel Design Considerations: Analysis of Medium-Support Interaction," University of Illinois at Urbana-Champaign, Report No. FRA-ORD&D 75-24, for Federal Railroad Administration, Department of Transportation, November.

Herring, K. S. and Kesler, C. E. (1974). "Concrete for Tunnel Liners: Behavior of Steel Fiber Reinforced Concrete Under Combined Loads," University of Illinois at Urbana-Champaign, Report No. FRA-ORDD 75-7 for Federal Railroad Administration, Department of Transportation, August.

Kani, G. N. (1964), "The Riddle of Shear Failure and Its Solution," Journal of the American Concrete Institute, Vol. 61, No. 4, April, pp. 441-467.

Parker, H. W., Deere, D. U., Peck, R. B., Birkemoe, P. C. and Semple, R. M. (1973). "Testing and Evaluation of Prototype Tunnel Support Systems," Report No. FRA-ORDD 74-11, Federal Railroad Administration, Department of Transportation (Order No. PB-231-912/AS from NTIS).

Paul, S. L., Kesler, C. E., Gaylord, E. H., Mohraz, B., Hendron, A. J. and Peck, R. B. (1974). "Research to Improve Tunnel Support Systems," University of Illinois at Urbana-Champaign, Report No. FRA ORDD 74-51, for Federal Railroad Administration, Department of Transportation, PB-235 762/AS, June.

☆U.S. GOVERNMENT PRINTING OFFICE: 1976—211-173/482